Modeling, Simulation, and Concept Studies of a Fuel Cell Hybrid Electric Vehicle Powertrain

Von der Fakultät für Ingenieurwissenschaften,

Abteilung Maschinenbau und Verfahrenstechnik

der

Universität Duisburg-Essen

zur Erlangung des akademischen Grades

eines

Doktors der Ingenieurwissenschaften

Dr.-Ing.

genehmigte Dissertation

von

Markus Özbek

aus

Södertälje, Schweden

Dedicated to my grandfather

Musa Özbek
1907 - 2010

who lived a long and prosperous life

Acknowledgement

The work presented in this thesis was initiated by the German federation of industrial research associations (AiF) together with the German association of powertrain technology (FVA) and conducted during my doctoral studies at the Chair of Dynamics and Control at the University of Duisburg-Essen.

First of all, I would like to thank my supervisor Univ.-Prof. Dr.-Ing. Dirk Söffker for his great support, encouragement, and help. Without him, this work would never initiate nor finish.

I would also like to thank Prof. Dr.-Ing. Dieter Schramm for his effort being the co-reviewer for my thesis.

This work was conducted in collaboration with the Chair of Energy Technology at the University of Duisburg-Essen and a great appreciation is given to rer.-nat. Prof. Angelika Heinzel, Dr.-Ing. Jürgen Roes, their technical support Jochen Bindemann, and especially my working partner Lars Wülbeck.

I would like to thank all my long time working partners at the Chair of Dynamics and Control; Hammoud Al-Joummaa, Kai-Uwe Dettmann, Dennis Gamrad, Frank Heidtmann, Yan Liu, Matthias Marx, and Mahmud-Sami Saadawia for their help and support and our secretaries Yvonne Vengels and Doris Schleithoff for their help with the administration. I wish them all the best in their future work. I would also like to thank all students who I supervised in their project works, bachelor-, and master theses. This includes Nguyen Binh, André Heßling, Xinfeng Huang, Sebastian Krins, Bertrand Teck Ping Ng, Yew Kok Poong, Adalbert Rudnicki, Theresia Rusch, Tharsis Ghim Han Teoh, and Shen Wang. I wish them all good luck in their studies.

Special thanks are given to my prior supervisor and mentor, Prof. Svante Gunnarsson at the Chair of Automatic Control at Linköping University in Sweden, for giving me the interest for control technique.

Finally but mostly I would like to thank my brothers and sisters and especially my parents whom without their love and support I would never be able to conduct this work.

Duisburg, May 2010   Markus Özbek

Contents

Nomenclature

Constants

Symbol	Parameter	Unit	Value
b_{cm}	Blower motor constant	[Nms/rad]	2.3e-4
d_c	Blower diameter	[m]	0.0508
$k_{st}A_{st}$	Product between thermal conductivity and conducting surface area of stack	[J/K]	6.0
k_{cm}	Blower motor constant	[Nm/A]	0.089
k_v	Blower motor constant	[Vs/rad]	0.0752
$m_{st}C_{p,st}$	Product between mass and specific heat capacity of stack	[J/K]	2e4
m_{veh}	Vehicle total mass	[kg]	201.3
n_{fc}	Number of fuel cells	[-]	45
p_{amb}	Ambient pressure	[Pa]	101325
p_{cp}	Blower pressure	[Pa]	101325
t_m	Membrane thickness	[cm]	3e-3
A_{fc}	Fuel cell active area	[cm^2]	50
A_{veh}	Vehicle front area	[m^2]	0.83
C_d	Vehicle drag coefficient	[-]	0.37
$C_{p,a}$	Specific air heat capacity	[J/kgK]	1004
$C_{p,cool}$	Specific coolant heat capacity	[J/kgK]	4183
$C_{p,v}$	Specific vapor heat capacity	[J/kgK]	1860
F	Faraday constant	[C]	96485
ΔG_f	Difference of Gibbs free energy for fuel cell reactants	[J/mol]	237.2e3
J_{cm}	Inertia of blower motor	[kgm^2]	7.245946e-4
J_{cp}	Inertia of blower and motor	[kgm^2]	7.25e-4
L_{cm}	Inductance of blower motor	[H]	4.98e-3
M_v	Vapor molar mass	[kg/mol]	18.02e-3
M_{H_2}	Hydrogen molar mass	[kg/mol]	2e-3
M_{N_2}	Nitrogen molar mass	[kg/mol]	28e-3
M_{O_2}	Oxygen molar mass	[kg/mol]	32e-3
N	Avogadro's number	[-]	6.022×10^{23}
R	Universal gas constant	[J/molK]	8.3145
R_a	Air gas constant	[J/kgK]	286.9
R_{bat}	Battery internal resistance	[Ω]	0.08
R_{cm}	Blower motor internal resistance	[Ω]	0.32
R_{gear}	Vehicle gear ratio	[m]	5

Symbol	Parameter	Unit	Value
$R_{i,sc}$	SuperCap internal resistance	[Ω]	0.012
R_v	Vapor gas constant	[J/kgK]	461.5
R_{H_2}	Hydrogen gas constant	[J/kgK]	4124.3
R_{N_2}	Nitrogen gas constant	[J/kgK]	296.8
R_{O_2}	Nitrogen gas constant	[J/kgK]	259.8
R_w	Vehicle wheel radius	[m]	0.223
T_{amb}	Ambient temperature	[K]	298
T_{cool}	Coolant water temperature	[K]	353
$T_{cp,in}$	Blower inlet temperature	[K]	298
V_{an}	Anode volume	[m^3]	1.08e-4
γ_a	Air heat capacity ratio	[-]	1.4
δ	Corrected pressure	[-]	1
η_{cm}	Blower motor efficiency	[%]	100
θ	Corrected temperature	[-]	298/288
ρ_a	Air density	[kg/m^3]	1.23
$\Delta H_{u,H_2}$	Hydrogen higher heating value	[J/kg]	141.9e9
$\Delta_v H$	condensation enthalpy of the water	[J/kg]	2260e3
ΔS	Reaction entropy	[J/molK]	-326.36

Variables

Symbol	Parameter	Unit
$E_{o,fc}$	Fuel cell open circuit voltage	[V]
i_{cm}	Blower motor current	[A]
i_{sc}	SuperCap current	[A]
i_{st}	Fuel cell stack current	[A]
I_{bat}	Battery current	[A]
J_w	Vehicle wheel inertia	[kgm^2]
m_{H_2}	Hydrogen mass in anode	[kg]
m_{N_2}	Nitrogen mass in cathode	[kg]
m_{O_2}	Oxygen mass in cathode	[kg]
$m_{w,an}$	Water mass in anode	[kg]
$m_{w,ca}$	Water mass in cathode	[kg]
Ma	Inlet mach number	[-]
M_{air}	Vehicle wheel torque from air resistance	[Nm]
M_{mot}	Motor torque	[Nm]
M_w	Vehicle wheel torque	[Nm]
N_{cp}	Blower speed	[rpm]
p_{cp}	Blower pressure	[Pa]
P_{cm}	Blower motor power	[W]
p_{H_2}	Hydrogen partial pressure	[Pa]
p_{O_2}	Oxygen partial pressure	[Pa]
p_{rm}	Return manifold pressure	[Pa]
p_{sat}	Air saturation pressure	[Pa]
p_{sm}	Supply manifold pressure	[Pa]
p_v	Vapor partial pressure	[Pa]
$P_{conv,in}$	Input converter power	[W]
$P_{conv,out}$	Output converter power	[W]
P_{cp}	Blower power	[W]
$P_{fc,net}$	Fuel cell net power	[W]
P_{st}	Fuel cell stack power	[W]
T_a	Air flow temperature	[K]
T_{cp}	Blower temperature	[K]
T_{fc}	Fuel cell temperature	[K]
U_{cp}	Blower blade tip speed	[m/s]
U_c	SuperCap voltage	[V]
u_{C_2}	Converter output voltage	[V]
v_{act}	Activation voltage losses	[V]
v_{conc}	Concentration voltage losses	[V]
v_{cm}	Blower input voltage	[V]
v_{fc}	Cell voltage	[V]

Symbol	Parameter	Unit
v_{loss}	Voltage losses	[V]
v_{ohm}	Ohmic voltage losses	[V]
v_{st}	Stack voltage	[V]
V_{H_2}	Consumed hydrogen fuel	[L]
W_{cp}	Blower mass flow rate	[kg/s]
W_{H2}	Hydrogen mass flow rate	[kg/s]
W_{cr}	Corrected blower mass flow rate	[kg/s]
Φ	Normalized blower flow rate	
Ψ	Blower map head parameter	
η_{conv}	Converter efficiency	[%]
η_{cp}	Blower efficiency	[%]
$\eta_{fc,nor}$	Normalized fuel cell efficiency	[-]
$\eta_{sys,nor}$	Normalized hybrid system efficiency	[-]
λ_m	Membrane water content ratio	[-]
λ_{O_2}	Excess oxygen ratio	[-]
θ_w	Vehicle wheel rotational angle	[rad]
τ_{cp}	Blower resistance torque	[Nm]
τ_f	Blower friction torque	[Nm]
τ_{cm}	Blower motor torque	[Nm]
ω_{cp}	Blower speed	[rad/s]

Abbreviations

AC	Alternating current
CFC	Corrected fuel consumption
DC	Direct current
DLC	Double layer capacitor
DoE	American department of energy
DoH	Degree of hybridization
ECE	Economic commission for Europe
EIA	Energy information agency
EPA	Environmental protection agency
ETC	European transient cycle
EUDC	Extra urban driving cycle
EV	Electric vehicle
FC	Fuel cell
FCHEV	Fuel cell hybrid electric vehicle
FTP	Federal test procedure
HEV	Hybrid electric vehicle
HiL	Hardware-in-the-Loop
ICE	Internal combustion engine
LPM	Liters per minute
MEA	Membrane electrode assembly
MIMO	Multiple-input multiple-output
PEM	Polymer electrolyte membrane
PEMFC	Polymer electrolyte membrane fuel cell
SC	SuperCap
SLPM	Standard liters per minute
SoC	State of charge
SSA	State-space averaging
UDDS	Urban dynamometer driving schedule

1   Introduction

Due to alarming environmental consequences from carbon dioxide emissions from fossil fuels, drastic measures must be taken to prevent further global warming. In June 1992, 154 nations signed an international encouragement to reduce greenhouse gases within the United Nations Framework Convention on Climate Change (UNFCCC) [Uni92]. Article 2 in the treaty states: *"The ultimate objective of this Convention and any related legal instruments that the Conference of the Parties may adopt is to achieve, in accordance with the relevant provisions of the Convention, stabilization of greenhouse gas concentrations in the atmosphere at a level that would prevent dangerous anthropogenic interference with the climate system. Such a level should be achieved within a time frame sufficient to allow ecosystems to adapt naturally to climate change, to ensure that food production is not threatened and to enable economic development to proceed in a sustainable manner."* This treaty is however an encouragement and does not legally bind the nations to fulfill the goals. In December 1997, an amendment called the Kyoto protocol [Uni98] which has more legally binding measures was presented in Kyoto (Japan). The main commitment of the Kyoto protocol is to reduce the average emissions of the greenhouse gases; carbon dioxide (CO_2), methane (CH_4), nitrous oxide (N_2O), hydrofluorocarbons (HFCs), perfluorocarbons (PFCs), and sulphur hexaflouride (SF_6) with 5.2% compared to the levels in 1990 by year 2012. A common commitment to decrease greenhouse gas emissions with 8% compared to 1990 has been undertaken by the EU-15[1] countries. By January 2009 a number of 183 nations had signed the Kyoto protocol.

According to the annual European community greenhouse gas inventory [KFG+09] (which is an obligation in the Kyoto protocol), the most important greenhouse gas by far is CO_2 which accounted in 2007 for 84% of the total (181 million tonnes CO_2 equivalents) greenhouse gas emissions in the EU-15 member states. About 20% of the CO_2 emissions in EU-15 come from road transportation industry[2]. In this sector, Germany accounts for the highest amount of CO_2 emissions in EU-15 with about 18%. Even though the total greenhouse gas emissions in EU-15 decreased with 4.3% between 1990-2007 (the goals of the Kyoto protocol are expected to be achieved), the CO_2 contribution from the road transportation industry increased with alarming 25%. Germany was the only country in the EU-15 to decrease (-4%) the CO_2 emissions in the road transportation sector [KFG+09].

The need to decrease the usage of fossil fuels would also have economical benefits and decrease the dependency from oil producing countries. The price of crude oil, which is presented by the U.S. Energy Information Agency (EIA) and depicted in Figure

---

[1]EU-15 includes Austria, Belgium, Denmark, Finland, France, Germany, Greece, Ireland, Italy, Luxembourg, Netherlands, Portugal, Spain, Sweden, and United Kingdom

[2]Road transportation includes all types of light-duty vehicles such as automobiles and light trucks, heavy-duty vehicles such as tractor trailers and buses, and on-road motorcycles (including mopeds, scooters, and three-wheelers)

1.1 shows a large increase in the last decade as countries with large populations like China and India with boosting economies contribute to the increased consumption of oil. There are hence, environmental, political, and economical reasons for decreasing usage of fossil fuels. Eliminating fossil fuels from the road transportation sector would remove the automobile industry from the environmental debate.
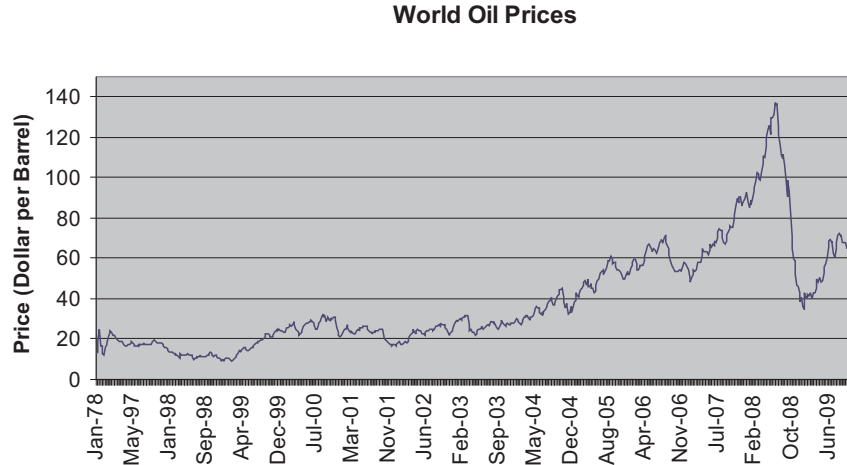
World Oil Prices

Figure 1.1: World oil prices development from U.S. Energy Information Administration [EIA09]

Zero-emission vehicles are expected to be achieved by electrifying their powertrain supplied with batteries [AN08, SSR08]. Most electric vehicles today are widely used in environments with noise and pollution restrictions, e.g. indoor and underwater. For smaller industrial electrical systems, such as scooter vehicles, fork lifts, and robots the main drawbacks are their low battery capacity, high costs, long charging time, short lifetime, and small temperature range [HU07].

As an intermediate step, hydrogen is expected to be the solution to the greenhouse gas emissions from the road transportation industry. Hydrogen vehicles can be driven by either combustion engines or with fuel cells. In contrast to combusted hydrogen, fuel cells use oxidation of the reactants which frees electrical energy instead of thermal energy (although some heat is produced in the fuel cells due to resistance). The efficiency in combustion engines is limited by the Carnot cycle whereas there are no limitations in oxidation of hydrogen [TZ00]. Fuel cells are more preferred due to their higher efficiency, lower noise, better reliability, and fewer moving parts [LD00].

1.1   Fuel cells

Fuel cells are electrochemical devices that convert chemical energy to electrical energy. Fuel cells consist of an anode and a cathode side that are separated by an electrolyte. The electrolyte can be a membrane electrode assembly as depicted in Figure 1.2. The principle of fuel cells can shortly be explained that fuel is provided to the anode side and an oxidant to the cathode side and through ionization of the reactants, protons are diffused through the electrolyte from anode to cathode as electrons are collected in electrodes. The electrons travel then from the anode to the cathode side through an external circuit to react with the ions there and the product is emitted from the fuel cell. The difference between batteries and fuel cells is that batteries are closed systems that generate electric energy when a reaction between stored reactants on the anode and cathode sides occur and deplete when the reactants are consumed. The process can be reversed by charging of the batteries. Fuel cells are however, supplied with reactants externally and the product is emitted. Fuel cells can operate as long as reactants are provided. The type of fuel, oxidant, electrolyte, and membrane can vary and gives many types of fuel cells. They are not presented here but can for further interest be found in [LD00].
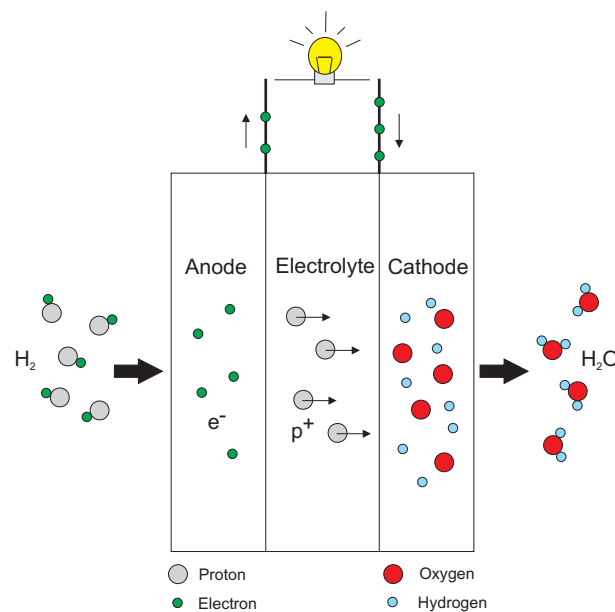

Figure 1.2: Membrane electrode assembly (MEA) of a single fuel cell with hydrogen and oxygen as reactants and pure water as only emission

History of fuel cells   The theory of fuel cells was discovered by the German scientist Christian Friedrich Schönbein in 1839 as he discovered ozone (O_3), which

was a bi-product from electrolyzing water to produce hydrogen and oxygen. This gave the idea to the Welch scientist William Robert Grove and he could demonstrate the very first fuel cell the same year [Gro39]. Schönbein described his theories with Grove through letter correspondence and Grove could later also demonstrate the hydrogen-oxygen fuel cell [Gro42].

It took however 120 years to the very first commercial application of fuel cells which was in the NASA space project Gemini. The fuel cells were used to generate electricity on-board the space ship and at the same time produced water for the crew. Up till today, fuel cells are used in space applications, e.g. in the international space station program (ISS).

The German navy is using fuel cells for the pioneering Type 212 A non-nuclear submarine, which is driven by a diesel generator and fuel cells in a hybrid concept to produce power for an electro-motor that propels the submarine. This gives a less noisy and vibrating operation of the submarine without emitting heat and it can remain under surface for three weeks without snorkeling.

Today, there exist many applications of fuel cells in a large variety of environments and applications, from bicycles to spacecrafts [CGJ04] and in a large range of power sizes, from micro- to megawatts, e.g. as remote stationary power stations [SDA09] or laptops [MJJ$^+$06], and as backup emergency power supply [ZGZW08]. One reason for the large variety of applications is that fuel cells are easily scalable and can be stacked together to give a larger system.

In a large survey in 2009 conducted by the organization Fuel Cell Today, it was estimated that 4000 units of small ($<$10 kW) fuel cell systems were delivered in 2008 for stationary applications and since 1996 approximately 50 large ($>$10 kW) stationary systems are delivered per year (although the delivered power has doubled between 1996 and 2008 to about 50 MW per year) [Ada09a, Ada09b].

If the hydrogen for fueling the fuel cells is produced from renewable energy sources, then the fuel cells can be considered as totally emission free, as the only emission during operation is pure water. Although hydrogen would be produced from carbon dioxide emitting sources and be transported to densely populated places, this could solve local emissions problems.

1.2   New powertrain technologies

As a first step to electrify the transportation sector, manufacturers are developing hybrid vehicles with different concepts that are already in the market. This gives the opportunity to successively develop the necessary components for fully electric vehicles, especially the batteries which are the main hurdle for commercializing electric vehicles due to cost, poor capacity, and lifetime. Further on, the infrastructure for

charging stations is today still not sufficient for supplying the whole vehicle market. Almost all vehicle manufacturers offer hybrid solutions for the costumers today and there are many configurations and concepts. Next, the most common of the new powertrain technologies are presented.

1.2.1 Hybrid vehicles

Hybrid vehicles are defined as having two or more power driving sources, e.g. an internal combustion engine (ICE) and an electro-motor. The very first hybrid vehicle can be designated to Ferdinand Porsche and Jacob Lohner, who built the Lohner-Porsche vehicle running with four wheel-attached electro motors and at the same time, the battery bank was charged from an ICE. This means, the vehicle had a so called series hybrid concept, or sometimes also referred to as range extender. The vehicle was presented in 1900 at the world exhibition in Paris and is illustrated in Figure 1.3.
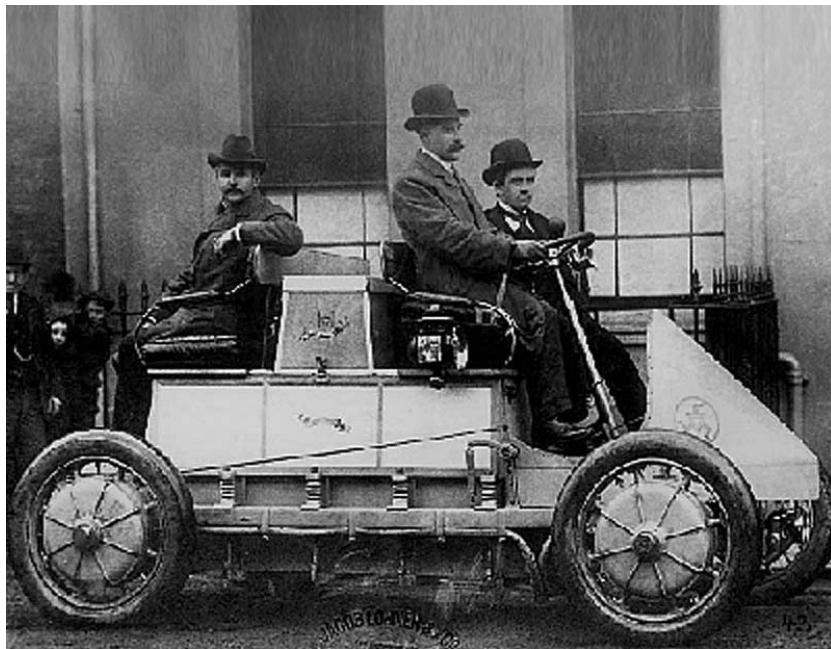
Figure 1.3: The Lohner-Porsche vehicle as the first hybrid vehicle with an ICE/battery series hybrid configuration with four wheel-motors [Hyb09]

Series hybrid

A series hybrid vehicle consists of an accumulator and an internal combustion engine. The combustion engine has no mechanical connection to the wheels and is used to

drive a generator to charge the onboard accumulator when needed.

Range extender In a range extender concept, the combustion engine extends the vehicles driving range. The main advantage of the series hybrid concept is that the combustion engine can be mainly run on its maximum efficiency point during charging of the accumulator. The disadvantage is that this concept requires a high-power and large accumulator pack (usually batteries) and that there are losses in the extra step of driving the generator to charge the accumulator.

Plug-in Plug-in vehicles are like series hybrid vehicles with the difference that the accumulator is larger and the vehicle can be plugged to a charging station. Plug-in vehicles can drive longer ranges with pure electric drive. The charger generator source (usually an ICE with gasoline, diesel, or fuel cells) is smaller than in series hybrids and is used to extend the driving range of the vehicle, while it can charge the accumulator during driving. The charger generator source can be referred to as a range extender unit and can be a module that is easily taken out and installed again when needed.

Parallel hybrid

In a parallel hybrid concept, both the combustion engine and the electro-motor are mechanically connected to the wheels. With the help of a clutch or gear, the distribution of power to the wheels can vary freely. The parallel hybrid concept can be divided in three groups, depending on the ratio of propulsion power between the ICE and the electro-motor.

Parallel hybrid: Micro hybrid The micro hybrid is the most basic of the parallel hybrid concepts. The main idea is to include a start-stop function in the vehicle, where the ICE shuts down during stand-still of the vehicle. Usually, this function is integrated in the braking pedal so that when the driver lifts the foot from the pedal, the ICE starts up again. The micro hybrid concept includes usually a generator-starter combination unit which works as a starter motor when starting up the ICE and as current generator during deceleration through engine braking. The latter function is necessary to fill the batteries before restarting the ICE and to provide energy to the electrical board of the vehicle. The micro-hybrid concept has a relatively small battery capacity compared to the other parallel hybrid concepts. The main advantage of this concept is its simplicity and fuel saving from turning of the engine during stand-still. It is also cheap due to the lack of large expensive battery banks and power electronics.

Parallel hybrid: Mild hybrid The mild hybrid concept has a larger electromotor and accumulator than the micro hybrid. The difference is that the electromotor here can provide auxiliary power to the vehicle during acceleration as well. During braking, the batteries are charged from the recuperated energy and provide power during acceleration. The mild hybrid vehicles are however not able to run fully electrically.

Parallel hybrid: Full hybrid Full hybrid vehicles work like mild hybrid with the difference that they are able to run fully electrically (sometimes only up to a certain speed), with the ICE turned off. This gives the advantage to run purely electrically in inner-city environment and with the ICE on highways.

1.2.2   Zero-emission electric vehicles

Fully electric vehicles are driven solely with electrical power and have no internal combustion engine. Even though the series hybrid vehicle can be driven solely by electrical power it is not categorized here due to that it includes an ICE.

Electric vehicles (EVs)

Purely battery driven electrical vehicles are considered to be the final goal of the vehicle alternative powertrain development within the next 20 years. They are totally emissions free if the electricity comes from renewable energy sources. The efficiency of the powertrain can be up to 90% which is considered very high in comparison to ICE driven vehicles with efficiency of about 30% and fuel cell vehicles with efficiency of about 40%. Further on, electric vehicles are quiet and do not require many moving parts. The main problems needed to be solved are the power densities of the batteries, long charging times (several hours for a full charge), and the short lifetime. Another problem is the high costs of batteries.

Fuel cell hybrid electric vehicles (FCHEVs)

In a fuel cell-based concept, the combustion engine is replaced by fuel cells. However, the fuel cells do not provide a direct torque to the driving wheels, instead they deliver electrical power to an electro-motor which drives the wheels. Fuel cells can be used as a range extender for Plug-in vehicles where they deliver power to the battery pack in a series connection.

The very first fuel cell vehicle being built is the Allis-Chalmers farm tractor which was developed by Harry Karl Ihrig [Smi09]. It was presented in Milwaukee in 1959

and consisted of 1008 individual alkaline fuel cells and had an output power of 15 kW. It was fueled with propane which has a large content of hydrogen.

General Motors presented the very first attempt from automotive industry to realize a fuel cell vehicle with the 6 passenger van (although only two passengers fitted due to the equipment onboard) GM Electrovan from 1966. A 5 kW fuel cell from Union Carbide was used and had an operational time of 1000 h and a range of 200 km, which could be realized with 700 bar liquid hydrogen and oxygen tanks onboard. For safety reasons, it was only used inside the company property and never brought to the market.

Hybrid electric vehicles (HEVs)

Electric and fuel cell vehicles can like the ICE-driven vehicles also be hybridized as hybrid electric vehicles (HEVs). Batteries can be compensated with SuperCaps to boost power and fuel cells can be compensated with batteries and/or SuperCaps to boost power and to harvest regenerative energy. Depending on the configuration of the power sources in HEVs, the concept names apply as with ICE hybrid vehicles mentioned above.

1.3   State-of-the-Art

Today, several vehicle manufacturers are researching in fuel cell-based vehicles and some of the prototypes are presented here briefly:

Honda FCX Clarity   Honda began with researching in fuel cell vehicles at the end of the 80's with the first prototype announcement coming 1999. The research resulted in the introduction of the first mass produced fuel cell vehicle from Honda at the Los Angeles Auto Show in 2007 with the Honda FCX Clarity [Bra09]. The Honda FCX Clarity has a motor with a maximum output of 100 kW and a range with the EPA combined driving cycle of 484 km with a full 171 L hydrogen tank.

Mercedes-Benz F-Cell   Mercedes-Benz have developed the F-Cell (both as A-class and B-class chassis) in small scale production which is based on the Mercedes-Benz Necar series prototypes developed between 1994 and 2000. The F-Cell has a 65 kW electro-motor with a range of 160 km with the 350 bar tank and 270 km with a newly developed 700 bar tank. As power booster, Nickel-metal hydride batteries are used for the A-class and Li-ion batteries are used for the B-class.

Volkswagen HyMotion and HyPower   Volkswagens contributions to the fuel cell vehicle development are the HyPower and HyMotion models which are based on the Touran and Bora models. The HyMotion models have Nickel-metal hydride batteries as power booster and the HyPower models use SuperCaps. They are equipped with 75 kW electro-motors and have a range of about 350 km.

GM HydroGen4   As the first vehicle manufacturer of fuel cell vehicles, GM have currently developed the fourth generation of the HydroGen fleet [HU07]. The HydroGen model is equipped with an electro-motor that gives a maximum of 93 kW output power and has a range of 320 km with a 700 bar hydrogen tank.

For fuel cell vehicles to be commercially available, there are mainly two thresholds that need to be overcome; the price and the lifetime of the fuel cells. Another important issue is the infrastructure of supplying hydrogen. Other drawbacks of fuel cells are their low power density and their inability to accept recuperated energy.

Up till now there are no large scale mass-manufactured fuel cell-based vehicles.

1.4   Project goal

The goal of this research project is to develop a comprehensive platform for a road-map to realize and to design fuel cell-based vehicles in the smaller power range (approx. 2 kW) aimed for mass-production. The work includes detailed modeling of the system components and overall hybrid system, realization of a Hardware-in-the-Loop (HiL) environment to be able to realize any fuel cell-based hybrid system, and to develop and test new control algorithms for the fuel cell system. Issues like component sizing and powermanagement strategies will be discussed. The modeling of the components should be validated on the HiL test rig and powermanagement strategies should be directly implemented in the HiL test rig and evaluated. The component control methods are conducted in a Matlab/Simulink simulation environment.

The thesis is outlined as follows:
In Chapter 2 a test rig built as a HiL concept is presented with its components. In Chapter 3 a simulation environment is developed and the corresponding models of the HiL components are presented and validated to the test rig. In Chapter 4 the control concepts of the fuel cells, DC/DC-converters, and electro-motor in the simulation models are developed. In Chapter 5 the parametrization and evaluation of the hybrid concept from a given load profile is discussed. Powermanagement concepts implemented in the HiL environment are discussed and evaluated in Chapter 6 and finally, a summary and outlook is given in Chapter 7.

2 Hardware-in-the-Loop test rig

Hardware-in-the-Loop (HiL) experimenting is a strong tool for engineers that can reduce development time and costs. The main idea is to replace physical components or the surrounding environment of a technical system with numerical models and to let the remaining components interact physically with the models through a suitable interface. Those components that can be physically excluded and modeled instead are chosen due to their high costs, that they are easy to model, and they are not key components to be considered. Experimenting with HiL makes it possible to conduct the experiments in a safe environment and abolishes the need of field tests [BPV98]. This is especially important for perilous experiments that deal with high explosive fuels (such as hydrogen) and electric storage components (such as SuperCaps). Every test is also easier to reproduce than in field tests. The principle of the HiL concept is depicted in Figure 2.1.
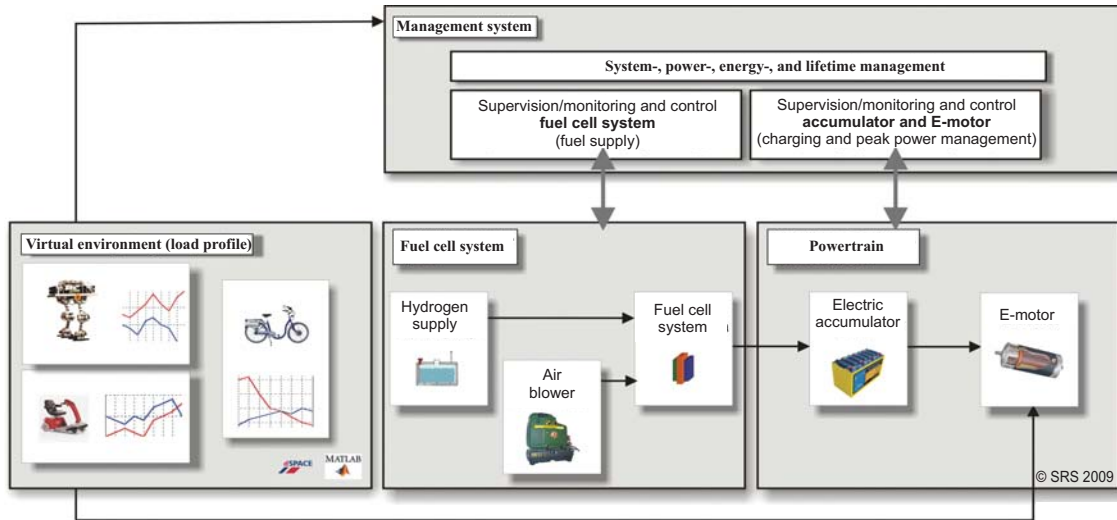

Figure 2.1: The Hardware-in-the-Loop concept with corresponding signal flows between virtual environment and physical components

The management system denotes a real-time acquisition system that interacts with the hardware and the virtual environment. Here, the control of the electro-motor, fuel cells, power flow between the components, and the simulation of the models are realized in real-time. The acquisition of the hardware components is realized through sensing at the test rig and control signals are sent to the test rig actuators. The virtual environment consists of the models that replace the hardware as well as environmental impacts on the system. The output is an arbitrarily measured or calculated load profile from a simulated system, e.g. scooter, fork-lift, robot, etc.

The realization of the load profile is done through an electro-motor that is physically attached to the drive-motor and realizes the load on the drive-motor through an applied torque.

For this application, a HiL test rig of the fuel cell-based hybrid powertrain, which is depicted in Figure 2.2, is developed and built up at the Chair of Dynamics and Control and the Chair of Energy Technology at the University of Duisburg-Essen. The powertrain is physically included in the test rig and the modeled components are the environment and the vehicle body. This means, if the powertrain is meant to be implemented in a scooter, then the scooter with its most important dynamics is realized as simulated model physically interacting with the hardware by suitable actuators. Next, an overview of the physical HiL test rig components is presented.

Figure 2.2: The Hardware-in-the-Loop test rig at the Chair of Dynamics and Control at the University of Duisburg-Essen. 1. Fuel cell system, 2. SuperCaps, 3. DC/DC-converters, 4. Power sink, 5. I/O-acquisition board, 6. Drive-motor, 7. Load-motor, 8. Drive-motor controller, 9. Load-motor controller

2.1 Fuel cell system

There exist many types of fuel cells which are differently optimized for different applications [LD00]. For mobile and vehicle applications the polymer electrolyte membrane fuel cells (PEMFCs) are mostly preferred [HU07]. This is due to their

low operation temperature (usually between 60-80 °C) which gives a faster start-up, their compactness, and their solid electrolyte.

In a fuel cell, the membrane electrode assembly (MEA) is a sandwich construction composed of catalyst on a carbon carrier material with the membrane in between. The MEA is in turn assembled between two bipolar plates that consist of channels for the gas reactants hydrogen on the anode side and air in the cathode side as depicted in Figure 2.3.
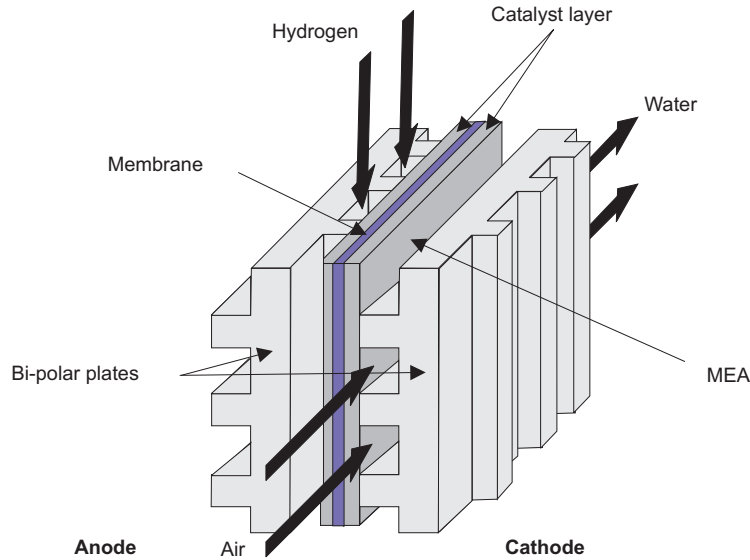

Figure 2.3: Sketch of a single fuel cell unit with the MEA sandwiched between the bipolar plates

Hydrogen is catalyzed on the platinum coated membrane on the anode side and electrons are then set free. The reaction is

$$2H_2 \rightarrow 4H^+ + 4e^- \tag{2.1}$$

whereas the free electrons are led to collectors and transported externally to the cathode side. Hence, they can be used in an external power converter to conduct electromechanical work. The protons are diffused through the membrane to the cathode side. A requirement for allowing diffusion of the protons is that the membrane contains water. The water is produced during operation of the fuel cells or can be externally supplied. On the cathode side, air is fed with help of a blower. The air is catalyzed with the same type of anode catalyst and together with the hydrogen electrons and protons from the anode the reaction is

$$O_2 + 4e^- + 4H^+ \rightarrow 2H_2O. \tag{2.2}$$

This shows that the only emission is pure water. The larger the surface of the membrane and catalysts, the larger the amount of electrons emitted. Hence, the maximum current output from a fuel cell is directly proportional to its surface. However, there are limits on how large a membrane surface can be made [LD00]. The bipolar plates must be good insulators towards electricity. The total assembly of the MEA together with the bipolar plates is defined as one single fuel cell. The maximum voltage over the anode and cathode is calculated according to Gibbs free energy. Gibbs free energy defines the difference of the energy content between the products and the reactants according to

$$\Delta G_f = G_{f,products} - G_{f,reactants}. \tag{2.3}$$

For the reaction

$$H_2 + \frac{1}{2}O_2 \rightarrow H_2O, \tag{2.4}$$

the Gibbs free energy at standard ambient conditions is $237.2\,\text{kJ/mol}$ and the maximum voltage a fuel cell can achieve is calculated according to

$$E = \frac{\Delta G_f}{NF} = 1.229\,\text{V}, \tag{2.5}$$

where N is Avogadro's number and F is the Faraday constant. However, there are losses due to heat generation and this voltage is in practice not realizable. Usually, in real applications the measured open circuit voltage is around $1\,\text{V}$ depending on temperature and pressure.

Two different fuel cell systems were used here, a Nexa® power module from Ballard [Bal09] and an alternative fuel cell system which is designed and built for this project. The alternative fuel cell system is used for modeling and validation and for developing new control algorithms for fuel cell systems. The Nexa® power module is used in the HiL test rig experiments due to its robustness and easiness to implement as an autonomous unit.

2.1.1 Ballard Nexa® power module

For HiL simulations, the utilized fuel cell system is the Ballard Nexa® power module which is depicted in Figure 2.4. It has a rated power output of $1.2\,\text{kW}$ at $26\,\text{V}$ and $46\,\text{A}$ at where it consumes $18.5\,\text{SLPM}$ (standard liters per minute) of hydrogen. The output voltage varies between 22 and $50\,\text{V}$.

Figure 2.4: The Nexa® power module fuel cell system from Ballard is used as power source in the HiL application [Bal09]

2.1.2   Alternative fuel cell system

The second fuel cell system is assembled together, from purchased components, between the Chair of Energy Technology and the Chair of Dynamics and Control at the University of Duisburg-Essen. This system is used mainly for modeling and validation of the fuel cell system and for testing new control algorithms on. The experimental results from this fuel cell system are used for validation of the fuel cell model in Chapter 3.

The fuel cell system regards the fuel cell stack with its peripheral components as depicted in Figure 2.5. This includes an air blower for the cathode air feeding, valve for hydrogen feeding, pump and valve for the recirculation of hydrogen, and a water cooling system which includes a pump and a radiator.

Fuel cell stack

The fuel cell stack, depicted in Figure 2.6 is manufactured and assembled at the Center for Fuel Cell Technology (ZBT GmbH) in Duisburg [ZBT09]. The MEA of the fuel cells consists of two platinum coated electrodes and assembled with bipolar plates. The stack has 45 cells and shows a rated voltage of 22 V at an output maximum power of 1.2 kW. Its working temperature is approximately 70 °C. The newly developed membrane requires less water content than conventional membranes.

Humidifier

The humidifier is a self made device depicted in Figure 2.5. It actually condenses recycled vapor and hydrogen from the anode exhaust and returns the hydrogen fully humidified to the anode input. This keeps the anode side humid which increases the conductibility of the membrane to protons. Recycling the hydrogen through the humidifier abolishes the need of an external vapor source.
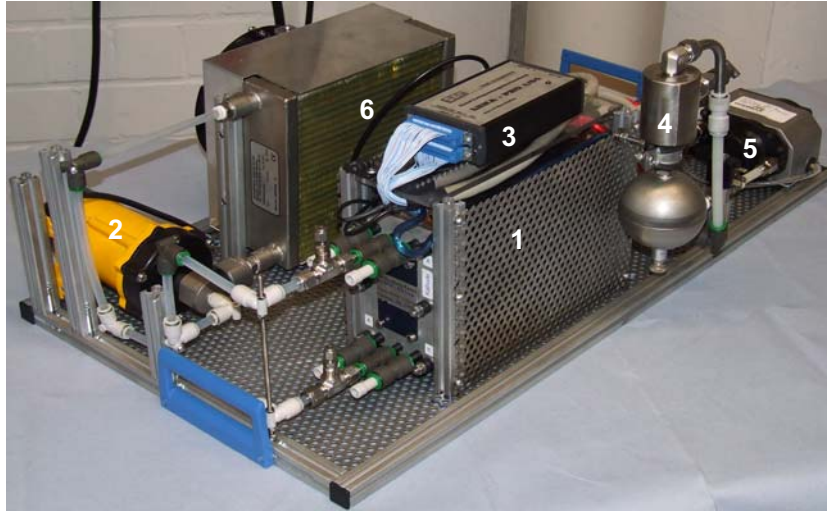
Figure 2.5: Fuel cell system including peripheral components. 1. Fuel cell stack, 2. Cooling water pump, 3. Single cell voltage measurement, 4. Humidifier, 5. Hydrogen recycling pump, 6. Cooler
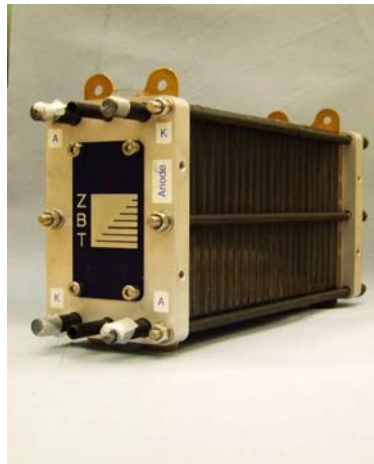

Figure 2.6: The fuel cell stack with water cooling used as an alternative fuel cell system from ZBT [ZBT09]

Blower

Several types of blowers are available on the market. Some of the most common are; snail- , piston radial-, axial-, and roots blowers. For this system a Roots blower is used. Roots blowers (named after their discoverer Francis Marion Roots) are one of the oldest types of blowers and are widely used for their silent operation, high reliability, and high efficiency. They consist of two lobed rotors which rotate merged against each other and trap air at the inlet side to transport and compress it at the outlet. They are able to produce large compression rates at low rotational speed. Their main disadvantage is their thermal inefficiency, meaning the outlet air has an unwanted increase in temperature. In fuel cells however, the inlet air temperature should maintain a temperature close to the operating temperature of the fuel cells in order not to damage the membrane and hence the increase of the inlet air temperature is beneficial.

This alternative fuel cell system is, as stated above in Chapter 2.1, used for modeling, validation, and control algorithm development.

Fuel cell system efficiency

The calculation of the efficiency of a fuel cell is sophisticated [LD00]. There is a voltage efficiency that regards only the stack without peripheral components and there is a total system efficiency that regards parasitic losses due to the blower, electronics, and valves. The interesting point regarding the aims within this research project of designing a fuel cell-based hybrid powertrain, is to find the maximum efficiency point of the fuel cell system. A more detailed regard of the efficiency of the fuel cell system is given in Chapter 4.2.1. Important is how the net output power that can be used for conducting work, changes as a function of the actual fuel consumption. With that, the maximum efficiency working point is detected and can be used for powermanagement strategies in Chapter 6. The electric consumption of the peripheral components of the Nexa® system cannot be measured. Only the power output (calculated from voltage multiplied with current) and volumetric fuel consumption in liters per minute[2] (LPM) are measured. A ramp function of current withdrawal is applied on the fuel cell system with the power sink and the normalized efficiency defined as the power output over fuel consumption as a function of the net power output

$$\eta_{fc,nor} = \frac{P_{fc,net}}{\dot{m}_{H_2}}, \tag{2.6}$$

is depicted in Figure 2.7. It is shown that the maximum efficiency is achieved at approximately 160 W. What appears as disturbances along the curve in the figure are

---

[2]It is assumed that the ambient conditions are not changed in the test lab with temperature control

moments of hydrogen purging, which is necessary to remove excess water from the fuel cells. Excess water in the membrane can block protons from diffusing through the membrane and hence decrease the efficiency of the fuel cells. Therefore, a valve is opened for a couple of seconds to purge hydrogen to remove the excess water, which can block the electrode from the gases [LD00].
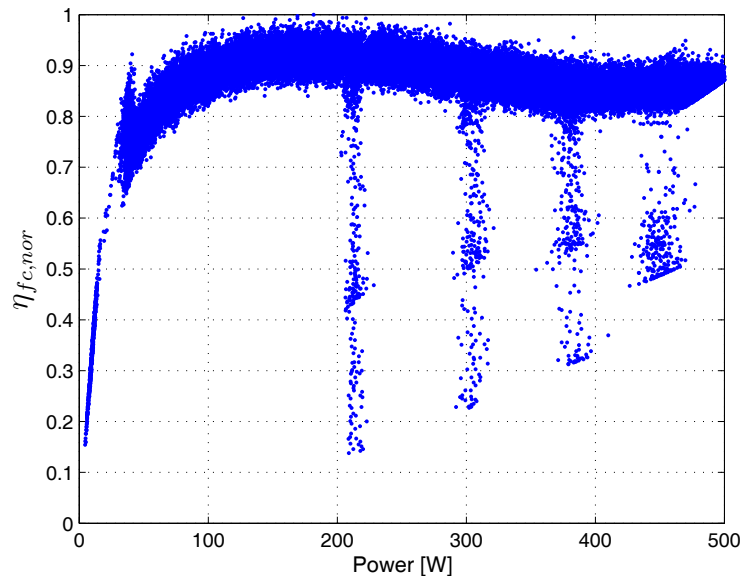

Figure 2.7: The normalized fuel cell system efficiency calculated as power output over fuel consumption as a function of the fuel cell power, is given and its maximum is at about 160 W

2.1.3   Lifetime of fuel cells

One of the main disadvantages of fuel cells is their short lifetime. In order to be able to commercialize fuel cells, it is important to deal with and improve the issues of their short lifetime. It is stated from the American Department of Energy (DoE) that the minimum lifetime requirements for fuel cells for the year 2010 should be about 5000 h of continuous operation in vehicle applications in order to make fuel cells commercially available [Ame09]. In this section, the most important aging mechanisms of PEMFCs will shortly be reviewed and explained.

Mainly, the lifetime of PEMFCs is limited by the membrane [CWY+06]. The degradation of the membrane can be categorized into mechanical, thermal, and catalyst degradation [Hua08]. These degradations mainly result in a voltage performance decrease. There are three degradation classes; baseline degradation which is inevitable

long-term material degradation that occurs as long as the fuel cells operate, transient degradation which occurs due to cyclic operation or varying operation conditions of the fuel cells and accelerates the membrane degradation, and finally sudden degradation which is linked to faulty operation of the fuel cells, such as fuel starvation or poor thermal control. Here, only the transient degradation is regarded due to that it shall be mitigated by hybridizing the powertrain in order to decrease or eliminate the transient operating conditions of the fuel cell system.

Mechanical degradation

Mechanical degradation of PEMFCs occurs in form of cracks, tears, punctures, and pinholes in the membrane which cause an early failure. The induced mechanical forces come partly from impulsion pressure generated from hydrogen, water, and air injections and are a minor contribution to the mechanical degradation [TPJ$^+$07]. Larger contributions to mechanical degradation are temperature and humidity cycles. Through these cycles, especially if they occur simultaneously, large stress changes are applied on the membrane [HSZ$^+$06]. Punctures, cracks, and pinholes on the membrane increase the hydrogen crossover which decreases the efficiency of the fuel cells and should be avoided.

Catalyst degradation

Additionally to the membrane degradation, the degradation of the catalyst is of importance for the fuel cell stack lifetime. Mainly three mechanisms contribute to the catalyst degradation; platinum (Pt) dissolution, carbon-support corrosion, and Pt sintering [YY07]. A detailed review on these degradation mechanisms is given in [YSMH09]. Platinum dissolution and carbon-support corrosion are strongly linked to each other. Platinum catalyzes the carbon-support oxidation and consequently, this accelerates the release of Pt-particles and hence, accelerates the degradation of the active surface. Carbon-support corrosion occurs during high temperature, high water content, and low pH-value operation. Oxygen atoms at the surface of the cathode side of the Pt-catalyst react with the carbon and emit CO_2 and with them the supported Pt. This decreases the contact surface area. Particle growth of the nano-sized Pt-crystals is another reason for a decreased contact area [BDG$^+$06]. During operation, migration of Pt-ions that evolve as a mid-step in the reaction phase occurs and sinter with neighboring particles which increases the size of the Pt-crystals. This phenomena is known as the Oswald ripening [SYG07]. These three effects contribute to loss of electrochemical surface area on the active layer of the MEA.

Thermal degradation

Thermal degradation refers to occurrence of hot-spots in the membrane caused by poorly thermal and water management. The hot-spots evaporate the water content locally and cause pinholes in the membrane which consequently increase the hydrogen cross-over through the membrane. Hydrogen cross-over is diffusion of whole hydrogen atoms through the membrane and may react (burn) in the cathode with oxygen and further increase the pinholes or be emitted through the exhaust [CZT+07]. Their energy content is thus wasted and this decreases the overall fuel cell efficiency. Too high operating temperatures leads to dryness of the membrane (which accelerates the mechanical degradation) and to an increase of the Pt-crystal sintering rate (which accelerate the catalyst degradation).

There are many studies that show that cyclic and transient operation of the fuel cells accelerates the degradation types mentioned above compared to steady-state operation [HSZ+06, MFF+08, SYG07, WCF+06]. To summarize this, it is preferable to operate the fuel cells in a steady-state fashion continuously rather than with alternating power output. This can be achieved by hybridizing the powertrain.

2.2   Energy storage accumulators

The considered powertrain includes secondary energy storage accumulators to increase the systems energy and power density. This is depicted in Figure 2.8 where the fuel cells have a high energy density but lacks in power density and e.g. SuperCaps that have a high power density but low energy density. By including both in a hybrid concept gives a system with both high energy as well as power density.

2.2.1   SuperCaps

SuperCaps (sometimes also referred as ultracapacitors or double layer capacitors) combine the advantages of conventional capacitors with the advantages of batteries, i.e. a high power density with a higher energy density. The porous inner structure gives the ability to store a large amount of charge in comparison to conventional capacitors. Up till today, the energy density of SuperCaps is about one tenth of the energy density of batteries but their power density is higher and hence can also be used in hybrid concepts to realize fast transient power demands. Physically, they differ from conventional batteries such that no chemical reactions occur and they have a very low inner resistance which explains the dense power output. The lifetime of SuperCaps is superior to the lifetime of batteries, being unaffected for many charge-discharge cycles. Further on, SuperCaps are not affected by memory effects, which is a common problem with batteries. The benefits of SuperCaps
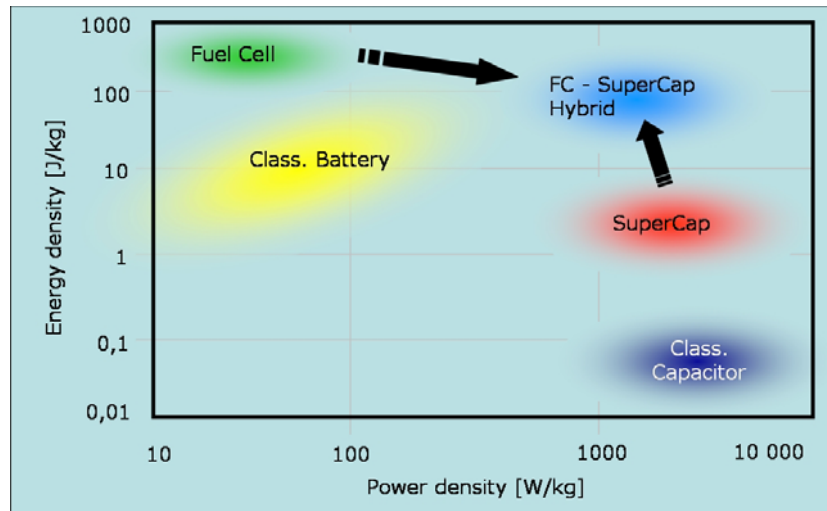
Figure 2.8: A Ragone-plot of the energy storage systems available today. A hybrid between fuel cells and SuperCaps gives a high energy- and high-power density system.

give the possibility to accept strong dynamic charging loads in contrast to batteries, where charging must be done in a more controllable fashion to avoid a short lifetime. For the validation and for use in the test rig, SuperCaps with a size of 3000 F and a maximum voltage of 2.7 V per cell are chosen here.

2.2.2   Batteries

Batteries are electrochemical energy storing devices which have to be distinguished from capacitors in the sense that the energy in batteries is chemically bounded which is converted to electric energy. Like fuel cells, batteries have an anode and cathode part that are separated with an electrolyte that can lead protons while the electrons travel through an external circuit. Batteries are distinguished from fuel cells by being closed systems, i.e. no external fuel is supplied. In rechargeable batteries, it is possible to invert the process and turn electric energy to chemically bounded energy. Another important factor between SuperCaps and batteries is the output voltage behavior as a function of charge which is depicted in Figure 2.9. SuperCaps have a larger range of output voltage and batteries have a narrow range, which can affect the bus-voltage of the hybrid system. The different battery types are distinguished by the materials used in the anode and cathode. Depending on material, different voltages, energy densities, and power densities are achieved. Lead-batteries are one of the most common and used batteries due to their low price, while Li-Ion batteries are high-density and high-power batteries that have gained more and more ground in recent years. In this research study Li-Ion batteries are not regarded due to

their complexity and high costs. Only lead-batteries are examined due to their low costs and for comparing fuel cells with commonly used industry batteries, which are typically lead-batteries. Three 12 V Sonnenschein lead-batteries (from manufacturer Exide Technologies [EXI09]) with 14 Ah each were used to be tested as an alternative to SuperCaps. The results will be given in Chapter 5.
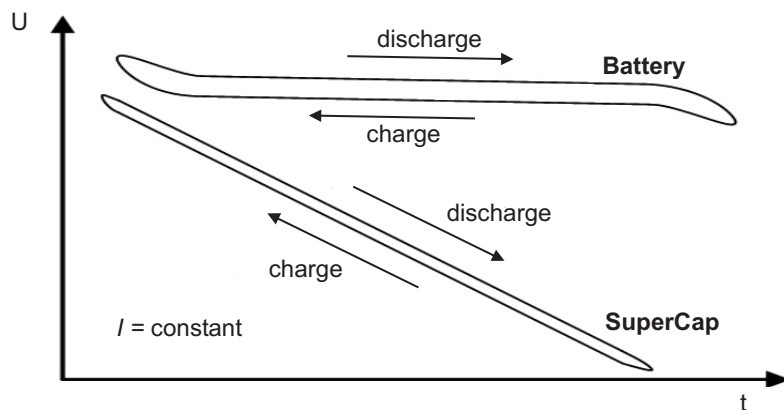

Figure 2.9: Typical voltage output curves for constant current for batteries and SuperCaps including hysteresis behavior

2.3   DC/DC-converters

DC/DC-converters are electric power devices that output a constant DC-voltage despite a varying DC-voltage on the input. Mainly, DC/DC-converters consist of an inductance and a capacitance part with a switch device that connects them in different topologies. The topology of the components inside the decides the type and character of the converter [Eri99]. The three common types of DC/DC-converters are buck-, boost-, and buck-boost converters. The input-output voltage ratio is controlled by the switching duty cycle D (which has a value between 0 and 1) as depicted in Figure 2.10. The buck converter has a linear relationship between duty cycle and input-output voltage ratio. It can only decrease the output voltage in relation to the input voltage. The relation is according to

$$U_{out} = U_{in}D. \tag{2.7}$$

The boost converter can only have an equal or larger output voltage than the input and the relationship is nonlinear. The output relates to the input with

$$U_{out} = U_{in}\frac{1}{1-D}. \tag{2.8}$$

The buck-boost converter has also a nonlinear relationship but the output voltage is inverted to the input voltage. The relationship is

$$U_{out} = -U_{in} \frac{D}{1-D}.$$

(2.9)

The reason for the nonlinearities of the boost- and buck-boost converters behavior will be given in Chapter 3.4. How to control the output voltage to follow a reference input will be given in Chapter 4.4. Furthermore, DC/DC-converters are also categorized as mono- and bi-directional. Mono-directional converters can only transfer power from the supply source (input) to the output. Mono-directional converters are protected with a diode at the input that blocks regenerative power. Bi-directional converters can transfer power to and from the source, which makes it possible to harvest energy that is recuperated at the output to the input source (if an accumulator is used). At the HiL test rig, three DC/DC-converters are used, as depicted in Figure 2.2. Due to the high costs of bi-directional converters, an alternative is to use two mono-directional converters in order to realize recuperation power saving. The converters, which are supplied from an accumulator and connected to the bus, are connected opposed from each other and during recuperation one is switched off while during powering the other one is switched off. The third converter is also a mono-directional and is supplied from the fuel cells. Since fuel cells cannot accept recuperated energy, there is no need to install a second converter. The converters used are identical and of type buck-boost, whereas the output voltage is the control variable. The converters make it possible to realize several different topologies at the HiL test rig.
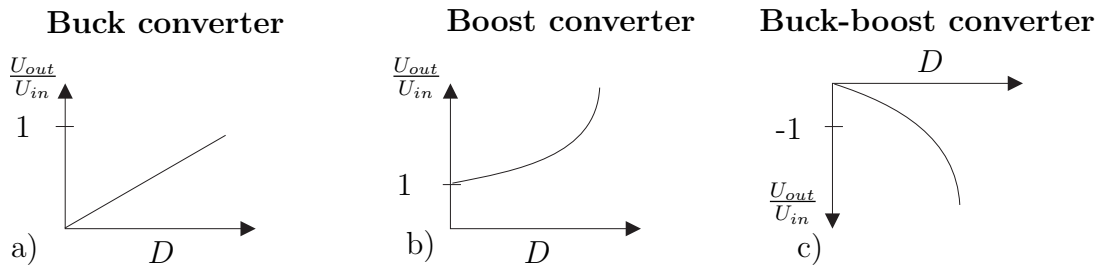

Figure 2.10: Three most common types of DC/DC-converters: a) Buck-, b) Boost-, and c) Buck-Boost converter with the typical input-output relation

DC/DC-converter efficiency   The efficiency of the DC/DC-converter is measured with a power output ramp as the converter is connected to the fuel cell system.

The result is plotted in Figure 2.11, where the efficiency is calculated with

$$\eta_{conv} = \frac{P_{conv,out}}{P_{conv,in}}. \tag{2.10}$$

As it can be seen, the efficiency is relatively low at lower power outputs and has its maximum starting at approximately 400 W.
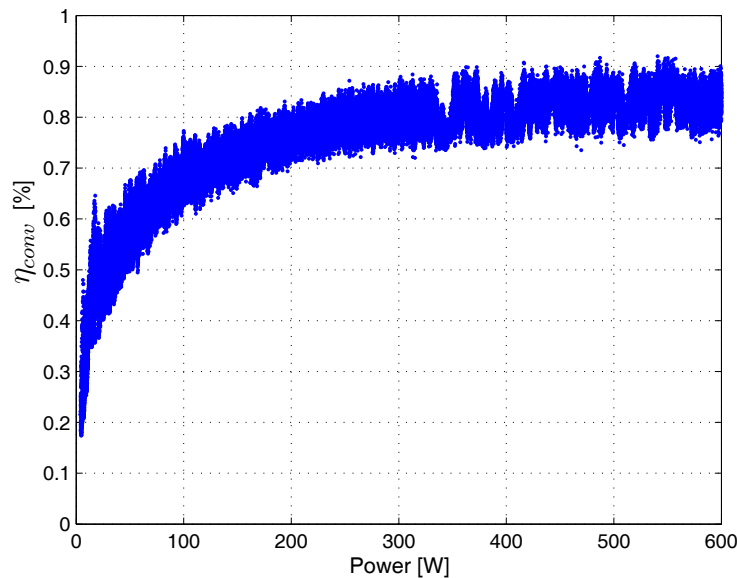

Figure 2.11: Efficiency of the DC/DC-converter as a function of the output voltage

2.4 Electric motors

All electric motors have the same main task, which is to convert electrical energy to mechanical energy. An electric motor consists of wiring cores that generate a magnetic field when energized with current. The magnetic field creates a force in a counterpart that makes an axle (rotor) to rotate. Some motors have the wiring in the rotor itself and some have it inside the housing (stator) of the motor. If this process is reversed, i.e. to mechanically rotate a shaft to produce electric power, it is then referred to as a generator. The motors used today in hybrid vehicle applications can do both and are referred to as four-quadrant motors. This makes it possible to harvest recuperated energy from declaration of the vehicle.

Mainly, electric motors are categorized in two groups; AC- and DC-motors, being supplied by AC- and DC-current respectively. This is however not totally true since

there exist motors built as AC-motors but still supplied from a DC-current source
and vice versa. This is possible with electronics in controllers and converters that
drive the motors. Typical DC-motors are those who are equipped with a brush
that leads current between stator and rotor. Brush-motors are easy to manufacture
and are cheap but are subjected to wear of the brush and produce sparks that
can be hazardous when used in systems that are supplied with flammable fuels,
e.g. hydrogen. Two types of AC-motors are asynchronous and synchronous motors.
Asynchronous motors produce the rotating force through a slip between induced
current frequency and rotating frequency. Usually, the slip angle decides the torque
that is produced. Synchronous motors can have permanent magnets that do not
require frequency slip to produce torque. For vehicle applications, synchronous
motors are usually preferred due to their better dynamical performance although
they are usually more expensive [Kie07]. To increase the torque density in the
motors, three phases of current (with a constant phase shift between) can be used
instead of one phase, which is usually the case from standard house jacks. These
motors are then referred to as three-phase motors.

Two electro-motors are used in the HiL test rig as depicted in Figure 2.2. One is
referred according to its use inside the concept as the drive-motor (because it is the
vehicle motor) and the other is referred to as the load-motor (because it applies the
simulated load from the environment onto the drive-motor). Both motors are three-
phase synchronous AC-motors which makes them highly dynamic and compact but
yet powerful.

2.4.1   Drive-motor

The drive motor is a so called brushless DC-motor. This implies to its charac-
teristic behavior which is similar to brushed DC-motors, although this motor is
brushless. This increases its dynamical performance and lifetime and does not emit
sparks which is necessary in terms of safety in environments with explosive gases.
It is supplied from a DC-current source and needs a controller to induce a mag-
netic field to drive the motor. The drive-motor has a permanent magnet of type
Samarium in the rotor which enhances the magnetic field density inside the housing.
For speed-control, it is equipped with an incremental encoder sensor for rotational
speed measuring. The rated rotational speed is 2500 RPM at where it has a rated
torque of 12.1 Nm and a rated current consumption of 8.7 A. The maximum torque is
15.1 Nm and maximum current is 10.3 A. These and other specifications are however
parameterizable with the motor controller and its software.

Drive-motor controller

The drive-motor controller is a four quadrant type, which makes it possible to recu-
perate braking energy back to the supply source. The supply voltage ranges between

24 and 50 V DC. It converts the supplied DC-current to three-phase high-voltage current to drive the motor. It is possible to realize position, speed, and torque control and the communication is realized with a CAN-bus protocol from the dSPACE system. With its software, it is possible to change several parameters, such as maximum torque, speed, control parameters, etc. For this application, it is important for the load-motor to be more dynamic than the drive-motor. The load, especially from calculated inertia, must be applied simultaneously as the drive-motor accelerates. Hence, the drive-motor is parameterized to make it possible.

2.4.2   Load-motor

The load-motor is a synchronous three-phase motor with better dynamics than the drive motor. The load-motor is supplied from the grid and returns the recuperated energy back to the grid. This does not influence the electrical power grid of the vehicle. The only energy transfer between load- and drive-motor is through mechanical stiff coupling that connects both motors as seen in Figure 2.2.

2.5   Implementation and experimental studies

A main idea of the used HiL-concept is that it shall be possible to implement any kind of environment simulated on-line from Matlab/Simulink. The powertrain consists of the presented hardware and is limited to 2 kW through parametrization of the drive-motor. The different maximum efficiency

$$\eta_{sys,nor} = \frac{P_{conv,out}}{\dot{m}_{H_2}} \tag{2.11}$$

working points of the fuel cells and the DC/DC-converter gives a total maximum efficiency point of the systems when connected together. This is depicted in Figure 2.12 and corresponds to the working point of 450 W output power from the DC/DC-converter.

2.5.1   Load profile implementation

The system is designed to be able to implement any load profile (as long as it is normalized within the max. 2 kW of the drive motor). A measured load profile from a real industrial application (fork-lift) is used to be implemented on the powertrain and to analyze. The load profile is shown in Figure 2.13.
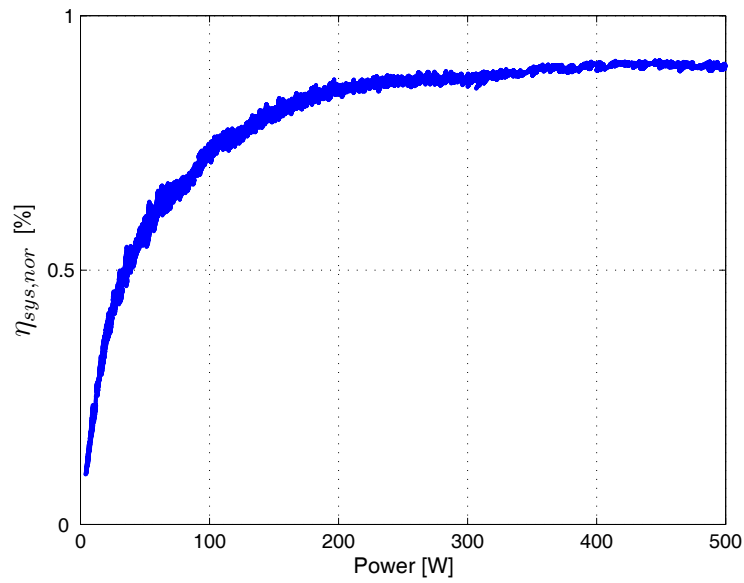
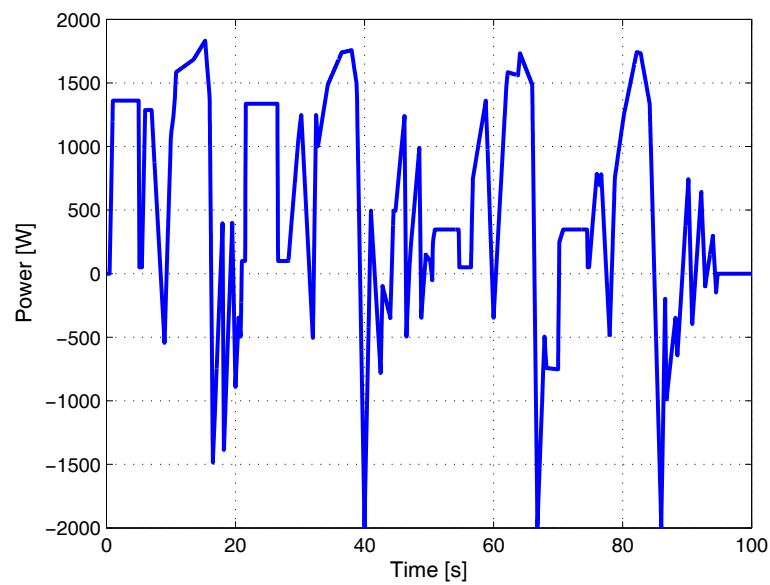Figure 2.12: Normalized efficiency of the hybrid system as a function of the power consumption with a maximum point from $450\,\mathrm{W}$

Figure 2.13: Normalized load profile which is implemented on the HiL test rig and is measured from an industrial fork-lift

2.5.2 Vehicle implementation

A scooter vehicle is modeled from data taken from an existing scooter [Gue05]. The drive motor can realize any standard driving cycle and the load motor applies the calculated virtual load on the drive motor. This includes wind-drag, friction forces, and inertia according to the equation

$$M_{mot} = (\ddot{\theta}_w(M_w R_{Tyre}^2 + J_w) + M_{air})\frac{R_{gear}}{R_w}. \tag{2.12}$$

where $\ddot{\theta}_w$ denotes the rotational acceleration of the scooter wheel, R_w, J_w, and M_w denote the radius, inertia, and mass of the scooter drive wheel, R_{gear} denotes the gear ratio between wheel and electro-motor, and the total air resistance is calculated as a torque applied on the electro-motor with M_{air}. The drive-motor is used to realize a speed reference with an built-in controller that is parameterized for realizing standard driving cycles with the modeled vehicle scooter. From Equation (2.12), the vehicle wheel acceleration $\ddot{\theta}_w$ is derived from derivation of the drive-motor speed (incremental encoder sensor) and the applied torque M_{mot} is then calculated. This torque is the reference to the load-motor. The calculations are subjected to delays but since the dynamics of the load-motor are higher than those of the drive-motor, the results are satisfying and it is possible to simulate any driving cycle with the HiL test rig.

3   Modeling the hybrid powertrain

A model of a technical system can be defined as being a tool for examining a system without conducting experiments [LG91]. If the model description of the system is mathematically, it is called an analytical one. Since many technical systems have well known physical properties, it is suitable to describe these with mathematical equations (often with differential equations). Describing a system with differential equations requires that simplifications of the system are acceptable, e.g. that nonlinearities are not regarded. When the equation solution depends on the actual input signal to the equation, it is called a *static model*. When the solution of the equation depends on the present and past input, it is called a *dynamic model*.

There are many analysis tools that can be used on technical systems but most require that a model of the system is available. Especially, when the model is linear the available methods are many, e.g. Bode-plots and Root-locus. In order to design a suitable controller for the system, it is helpful to have a model. If the examination of the model is made numerically, it is called *simulation* (from Latins *simulare* meaning pretend).

Modeling of hybrid components presented in Chapter 2 is conducted to give a tool for numerical experimenting for analyzing the components, different topologies, and powermanagement strategies. With the models, the simulations are made faster, safer, and cheaper as in a HiL or real environment. Further on, the models allow fast parametrization and sizing of the system.

The chapter is organized as follows: first, a model of the fuel cell system including the stack, air blower, and temperature is presented. Then, a model which describes the typical nonlinear output voltage as a function of state-of-charge of the SuperCaps is given. Further on, a common model for all kinds of batteries will be introduced, here describing lead-batteries. Shortly, a simple DC-motor model will be presented as well as a DC/DC-converter model. Finally, all models will be merged and together with a vehicle model, give the whole hybrid powertrain model. The validation of the individual models as well as of the whole powertrain finalizes this chapter.

3.1   Fuel cell system model

In this section, the component models of the stack and air supply system will be given and they will be validated to real system components. The fuel cell system with its corresponding fuel cell stack is described in Chapter 2.1 and depicted in Figure 2.5.

3.1.1 PEM fuel cell stack model

The fuel cell stack is the core component of the considered fuel cell system and a part of the corresponding model is given here. Input to the stack model is the stack current i_{st} and the output is the stack voltage v_{st}. A fuel cell stack model usually consists of four submodels: the stack voltage model, the anode mass flow model, the cathode mass flow model, and the membrane hydration model. More details are given in [PSP04]. Here, the equations of the stack voltage are briefly given. The stack voltage is given by

$$v_{st} = n_{fc} v_{fc}, \tag{3.1}$$

where n_{fc} denotes the number of cells and v_{fc} represents the single cell voltage, which is calculated as

$$v_{fc} = E_{o,fc} - v_{loss}, \tag{3.2}$$

where $E_{o,fc}$ denotes the open circuit voltage and v_{loss} the total voltage losses, i.e. activation, ohmic, and concentration losses. The voltage $E_{o,fc}$ can be calculated according to the Nernst equation by

$$E_{o,fc} = 1.229 - 8.5 \times 10^{-4}(T_{fc} - 298.15) +$$
$$+ 4.308 \times 10^{-5} T_{fc} \left(\ln \left(\frac{p_{H_2}}{101325} \right) + \frac{1}{2} \ln \left(\frac{p_{O_2}}{101325} \right) \right), \tag{3.3}$$

where T_{fc} denotes the cell temperature, p_{H_2} the hydrogen partial pressure in the anode, and p_{O_2} the oxygen partial pressure in the cathode. The voltage losses v_{loss} are described by

$$v_{loss} = v_{act} + v_{ohm} + v_{conc}, \tag{3.4}$$

where v_{act} is the voltage drop caused by activation losses, v_{ohm} denotes the ohmic losses, and v_{conc} the concentration losses. The activation losses v_{act} are calculated as

$$v_{act} = v_0 + v_a \left(1 - e^{-c_1 i} \right), \tag{3.5}$$

where the constants v_0, v_a, and c_i are taken from [PSP04]. Here i denotes the current density defined by

$$i = \frac{i_{st}}{A_{fc}}, \tag{3.6}$$

where A_{fc} represents the total cell area of the fuel cells. The ohmic losses v_{ohm} are calculated as

$$v_{ohm} = i R_{ohm}, \tag{3.7}$$

where R_{ohm} denotes the internal electrical resistance and is related to the membrane conductivity σ_m by

$$R_{ohm} = \frac{t_m}{\sigma_m}, \tag{3.8}$$

where t_m denotes the membrane thickness. The membrane conductivity σ_m can be calculated as

$$\sigma_m = b_1 \exp\left(b_2 \left(\frac{1}{303} - \frac{1}{T_{fc}}\right)\right), \tag{3.9}$$

where b_1 is related to the membrane water content λ_m and can be expressed with

$$b_1 = b_{11}\lambda_m - b_{12}. \tag{3.10}$$

The constants b_{11}, b_{12}, and b_2 for the membrane are taken from [SZG91]. The voltage drop due to the concentration losses is calculated as

$$v_{conc} = i \left(c_2 \frac{i}{i_{max}}\right)^{c_3}, \tag{3.11}$$

where c_3 is a constant and i_{max} denotes the maximum current density. In [PSP04], c_2 switches between two functions depending on the oxygen partial pressure and the water saturation pressure. However, while it is dealt here with a low-pressure fuel cell system c_2 is described as

$$c_2 = (7.16 \times 10^{-4} T_{fc} - 0.622) \left(\frac{p_{O_2}}{0.1173} + p_{sat}\right) - 1.45 \times 10^{-3} T_{fc} + 1.68. \tag{3.12}$$

3.1.2 Air supply system model

The modeling of the air supply system with the blower motor voltage v_{cm} as input and the outlet air flow $W_{cp,out}$ as output is here introduced. The model of the blower is based on a real blower from a Nexa® power module fuel cell stack system from Ballard [Bal09]. The blower model consists of two submodels as depicted in Figure 3.1, the model of the blower motor and the blower map which are developed in sequel. As a notation, the outlet pressure $p_{cp,out}$ corresponds to the fuel cell supply manifold pressure. The air supply system consists of a blower with a supply manifold that provides a mass flow of pressurized air to the fuel cell stack and of an electromotor that drives the blower. Typical blower motors used in fuel cell applications are three-phase brushless DC-motors due to their high dynamics, high efficiency, and for not emitting sparks like brushed DC-motors. However, the dynamical behavior of such motors is very similar to brushed DC-motors.
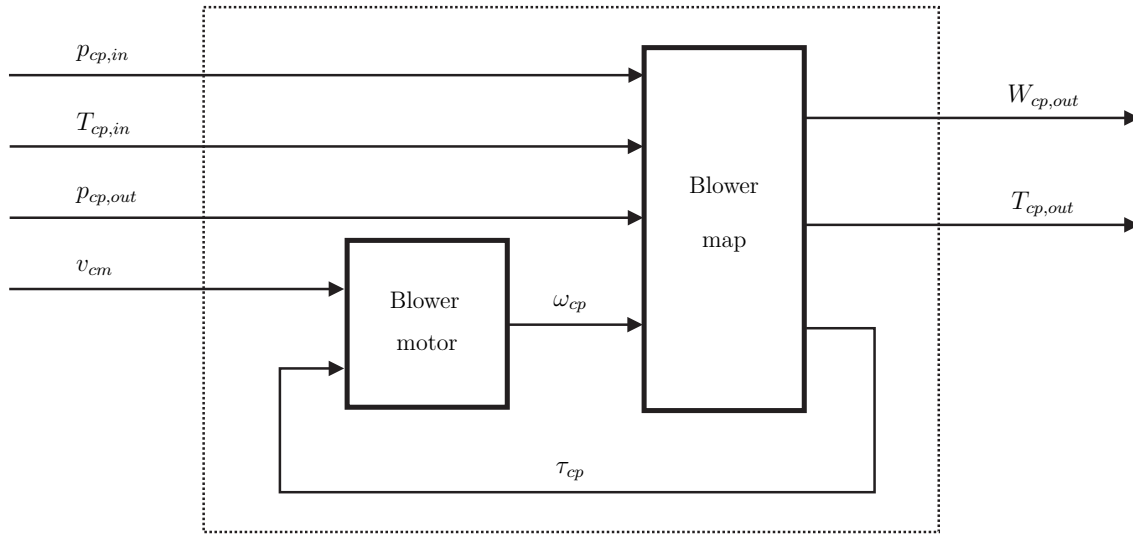
Figure 3.1: Block diagram of the blower model with corresponding inputs and outputs

DC-motor

In [PSP04] the motor driving the blower is simplified to a static behavior because the fuel cell system is a large system (over $50\,\mathrm{kW}$) and hence has large time constants. Therefore, the motor time behavior can be assumed as static. For smaller fuel cell systems (like the $1.2\,\mathrm{kW}$ system used here) the time constants are smaller and the bandwidth higher, so the need for a fast controller is larger. By calculating the dynamical behavior of the motor, the accuracy of the model increases and a better controller can be developed. The depiction of the armature and the rotor are shown in Figure 3.2. It should be noted that the drive-motor is modeled with the same dynamical behavior as the blower motor with different parameters and hence not repeated.

In this linear model, the blower speed and the armature current are defined by two ordinary differential equations. The dynamical behavior of the blower speed is modeled by

$$J_{cp}\frac{d\omega_{cp}}{dt} = \tau_{cm} - \tau_f - \tau_{cp}, \tag{3.13}$$

where J_{cp} denotes the combined rotary inertia of the blower and the motor, τ_{cm} denotes the blower motor torque, τ_{cp} the external load on the motor, and τ_f denotes the torque loss in the motor due to damping and friction. The blower motor torque τ_{cm} can be calculated using the armature current i_{cm} and a constant factor k_{cm} by
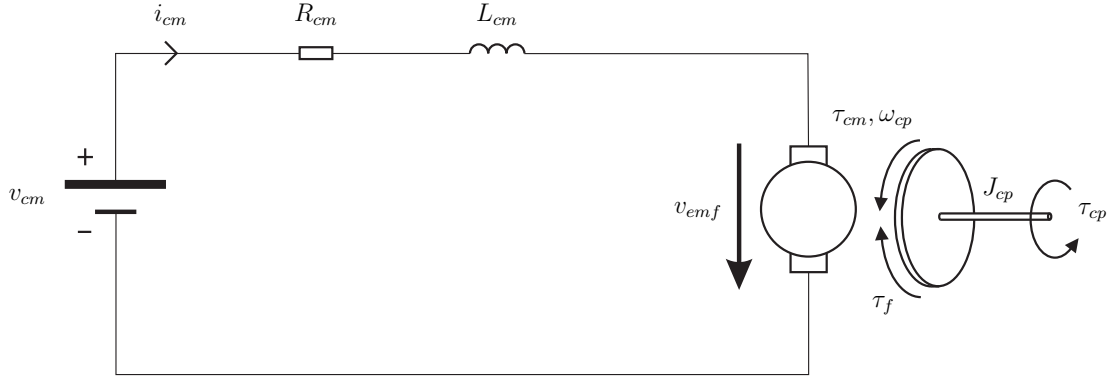
$$\tau_{cm} = k_{cm}i_{cm}. \tag{3.14}$$

Figure 3.2: Schematic representation of the blower DC-motor

The torque loss τ_f is assumed proportional to the blower speed by a constant factor b_{cm} with

$$\tau_f = b_{cm}\omega_{cp}. \tag{3.15}$$

The external load τ_{cp} is calculated in the blower map block. The dynamical behavior of the motor armature current is represented using Kirchhoff's voltage law by

$$L_{cm}\frac{di_{cm}}{dt} = v_{cm} - v_{R,cm} - v_{emf}, \tag{3.16}$$

where L_{cm} denotes the motor inductance, v_{cm} the input voltage to the blower motor, $v_{R,cm}$ the voltage drop over the internal electric resistance R_{cm}, and v_{emf} the induced voltage from the back electromotive force. The voltage drop over the resistance $v_{R,cm}$ is related to the armature current by

$$v_{R,cm} = R_{cm}i_{cm}. \tag{3.17}$$

If an electrical conductor moves across a magnetic field, an electrical voltage is induced in the conductor. In a DC-motor, the rotational movement of the rotor in the stator magnetic field induces a voltage in its winding. This induced voltage is called the back electromotive force v_{emf} and relates to the blower speed ω_{cp} with

$$v_{emf} = k_v\omega_{cp}, \tag{3.18}$$

where k_v is a constant factor, denoting the relationship between electromotive force and rotating speed. The parameters $J_{cp}, L_{cm}, R_{cm}, k_t, b_{cm}$, and k_v have to be experimentally determined.

Blower map

In the blower map, depicted in Figure 3.1, the air mass flow from the blower $W_{cp,out}$, the temperature of the air leaving the blower $T_{cp,out}$, and the blower torque τ_{cp} are

determined with static equations. The inputs to the blower map are the inlet $p_{cp,in}$ and outlet $p_{cp,out}$ air pressures, the blower speed ω_{cp}, as well as the air temperature entering the blower $T_{cp,in}$. The outlet manifold pressure $p_{cp,out}$ can either be calculated from the fuel cell model or like here, inserted from measurements. A typical approach determining the blower map is realized by including measurements in look-up tables. However, the standard linear interpolation routines used in look-up tables are neither continuous nor differentiable as sometimes discontinuities appear which can slow down simulations [CHMF99]. For this reason look-up tables are not well suited for control-oriented dynamic models. Instead, the measurement data of the blower performance are represented by continuous functions, determined using nonlinear curve fitting methods. Such approaches used for modeling and their benefits are further mentioned in [MK99]. As described in [CHMF99], the mass flow rate from the blower $W_{cp,out}$ is related to the corrected mass flow W_{cr} by

$$W_{cp,out} = W_{cr}\frac{p_{cr}}{\sqrt{T_{cr}}}, \tag{3.19}$$

where the corrected temperature is defined as $T_{cr} = T_{cp,in}/288$ and the corrected pressure as $p_{cr} = p_{cp,in}$. Corrected variables are applied in this model, because varying ambient conditions can be considered in the blower model[1]. The corrected mass flow W_{cr} is calculated as

$$W_{cr} = \Phi\rho_a\frac{\pi}{4}d_c^2 U_{cp}, \tag{3.20}$$

where Φ denotes the normalized blower flow rate, ρ_a the air density, d_c the blower diameter, and U_{cp} denotes the blower blade tip speed defined by

$$U_{cp} = \frac{\pi}{60}d_c N_{cr}. \tag{3.21}$$

The corrected blower speed N_{cr} is related to the blower speed by

$$N_{cr} = \frac{60\omega_{cp}}{2\pi\sqrt{T_{cr}}}. \tag{3.22}$$

The normalized blower flow rate Φ can be expressed as a function of the head parameter Ψ by

$$\Phi = \frac{k_3\,\Psi - k_1}{k_2 + \Psi}, \tag{3.23}$$

where k_i are factors which depend on the Mach number Ma of the inlet air and can be calculated as

$$k_i = a_i + b_i Ma, \quad i = 1, 2, 3, \tag{3.24}$$

---

[1]The corrected variables correspond to the values which would be measured at ambient conditions on a standard day at sea level, i.e. a temperature of $15°C$ and a pressure of $101\,325\,Pa$

where the Mach number Ma is defined by

$$Ma = \frac{U_{cp}}{\sqrt{\gamma_a R_a T_{cp,in}}}. \tag{3.25}$$

The dimensionless head parameter Ψ is calculated using Jensen & Kristensen method [MK99] with

$$\Psi = \frac{C_{p,a} T_{cp,in} \left(\left(\frac{p_{cp,out}}{p_{cp,in}} \right)^{\frac{\gamma_a - 1}{\gamma_a}} - 1 \right)}{\frac{1}{2} U_{cp}^2}, \tag{3.26}$$

where $C_{p,a}$ denotes the specific heat capacity and γ_a the heat capacity ratio of air [MS07]. Another important blower performance parameter is the blower efficiency η_{cp}, which depends on the normalized mass flow rate Φ and the Mach number Ma and is expressed as

$$\eta_{cp} = c_1 \Phi^2 + c_2 \Phi + c_3, \text{ with} \tag{3.27}$$

$$c_i = \frac{d_i + e_i Ma}{f_i - Ma}, \quad i = 1, 2, 3. \tag{3.28}$$

The constants a_i, b_i, d_i, e_i, and f_i for $i = 1, 2, 3$ are parameters which can be determined through curve fitting on the measurement data. The temperature of the air leaving the blower is given by

$$T_{cp,out} = T_{cp,in} + \Delta T_{cp}, \tag{3.29}$$

where ΔT_{cp} is the temperature change across the blower which is calculated as

$$\Delta T_{cp} = \frac{\Delta h_{s,cp}}{C_{p,a} \eta_{cp}}, \tag{3.30}$$

where $\Delta h_{s,cp}$ denotes the isentropic enthalpy change across the blower and is calculated as

$$\Delta h_{s,cp} = \frac{\gamma_a}{\gamma_a - 1} R_a T_{cp,in} \left(\left(\frac{p_{cp,out}}{p_{cp,in}} \right)^{\frac{\gamma_a - 1}{\gamma_a}} - 1 \right). \tag{3.31}$$

According to Equations (3.29)-(3.31), it follows that the temperature $T_{cp,out}$ results to

$$T_{cp,out} = T_{cp,in} + \frac{\gamma_a}{\gamma_a - 1} \frac{R_a}{C_{p,a}} \frac{T_{cp,in}}{\eta_{cp}} \left(\left(\frac{p_{cp,out}}{p_{cp,in}} \right)^{\frac{\gamma_a - 1}{\gamma_a}} - 1 \right). \tag{3.32}$$

The relation between the heat capacity ratio γ_a and the gas constant of air is given by

$$\frac{R_a}{C_{p,a}} = \frac{\gamma_a - 1}{\gamma_a}. \tag{3.33}$$

Using this relation in (3.32) gives finally

$$T_{cp,out} = T_{cp,in} + \frac{T_{cp,in}}{\eta_{cp}} \left(\left(\frac{p_{cp,out}}{p_{cp,in}} \right)^{\frac{\gamma_a - 1}{\gamma_a}} - 1 \right). \tag{3.34}$$

The third output of the blower map, which is an input to the blower motor, is the blower torque τ_{cp}, and is calculated as

$$\tau_{cp} = \frac{P_{cp}}{\omega_{cp}}, \tag{3.35}$$

where the blower power P_{cp} is defined by

$$P_{cp} = C_{p,a} W_{cp,out} \left(T_{cp,out} - T_{cp,in} \right). \tag{3.36}$$

Inserting Equation (3.36) in (3.34) and rearranging gives

$$P_{cp} = \frac{C_{p,a} W_{cp,out} T_{cp,in}}{\eta_{cp}} \left(\left(\frac{p_{cp,out}}{p_{cp,in}} \right)^{\frac{\gamma_a - 1}{\gamma_a}} - 1 \right). \tag{3.37}$$

Finally, it follows from Equation (3.35) and (3.37) that

$$\tau_{cp} = \frac{C_{p,a} W_{cp,out} T_{cp,in}}{\omega_{cp} \eta_{cp}} \left(\left(\frac{p_{cp,out}}{p_{cp,in}} \right)^{\frac{\gamma_a - 1}{\gamma_a}} - 1 \right). \tag{3.38}$$

3.1.3   Temperature dynamics model

In [PSP04] it is assumed, that the temperature of the fuel cell stack is constant. But in reality, without a cooling system, the temperature in a fuel cell stack strongly changes due to the chemical reactions inside the stack. As introduced in [AC08] and reviewed in [Hua08], the stack temperature has a strong influence on the fuel cell performance and lifetime. In this section the temperature of the fuel cell stack is modeled.

The temperature model is described as a first order system with the temperature gradient described as

$$\dot{T}_{st} = \frac{1}{m_{st} C_{p,st}} \left(\dot{Q}_{react} - \dot{Q}_{cool} - \dot{Q}_{a} - \dot{Q}_{amb} - \dot{Q}_{v} \right), \tag{3.39}$$

where $C_{p,st}$ and m_{st} denote the specific heat capacity and mass of the fuel cell stack respectively and the terms denote heat flows. The heat flow from the reaction between hydrogen and oxygen is calculated with

$$\dot{Q}_{react} = n_{st}i_{st}\left(-\frac{T_{st}\Delta S}{4F} + v_{loss}\right),\qquad(3.40)$$

where ΔS denotes the entropy change of the reaction between hydrogen and oxygen. The heat flow between the stack and the cooling water is given by

$$\dot{Q}_{cool} = C_{p,cool}\dot{m}_{cool}\left(T_{st} - T_{cool}\right),\qquad(3.41)$$

where $C_{p,cool}$ denotes the specific heat capacity, $\dot{m}_{cool}$ the mass flow, and T_{cool} the temperature of the coolant respectively. The coolant is water and its temperature before entering the stack is assumed constant. The heat exchange between the stack and the air entering the stack is given by

$$\dot{Q}_a = C_{p,a}\dot{m}_a\left(T_{st} - T_a\right),\qquad(3.42)$$

where $C_{p,a}$ denotes the specific heat capacity, $\dot{m}_a$ the mass flow, and T_a the temperature of the air. Note that the inlet air flow and temperature correspond to the outlet blower air flow and temperature from Chapter 3.1, i.e. $\dot{m}_a = W_{cp,out}$ and $T_a = T_{cp,out}$. The heat exchange between the stack and the ambient is given by

$$\dot{Q}_{amb} = k_{st}A_{st}\left(T_{st} - T_{amb}\right),\qquad(3.43)$$

where k_{st} is the thermal conductivity and A_{st} the total surface area of the fuel cell stack respectively. The constant k_{st} is determined experimentally and A_{st} is measured. The ambient temperature is given by T_{amb} and assumed as constant. Finally, the heat exchange between the stack and the vapor produced or injected in the fuel cell stack is given by

$$\dot{Q}_v = C_{p,v}\left(\dot{m}_{v,out}T_{st} - \dot{m}_{v,in}T_{v,in}\right) - \dot{m}_{l,out}\Delta_v H,\qquad(3.44)$$

where $C_{p,v}$ denotes the specific heat capacity of vapor, $\dot{m}_{v,out}$ and $\dot{m}_{v,in}$ denote the vapor mass flows in respectively out of the stack, $T_{v,in}$ is the temperature of the vapor entering the stack and the last term in the equation denotes the liquified water leaving the stack with $\Delta_v H$ denoting the specific enthalpy of the water leaving the stack [MS07].

3.2   SuperCap model

SuperCaps differ from conventional capacitors in the sense that a double layer instead of a single dielectric layer is built in. Between the electrode plates, a porous material with large contact area permits a large load of electrons to be stored.
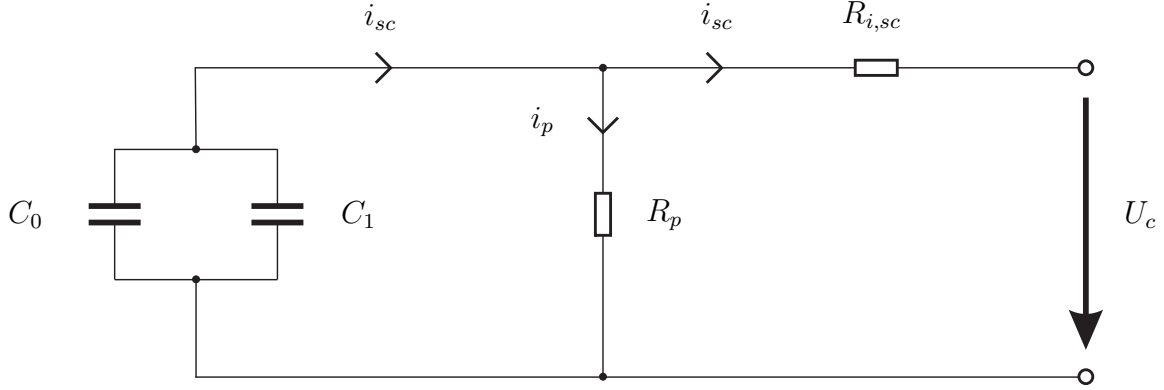
Figure 3.3: Schematic diagram of a SuperCap model with variable capacitance

The variable capacitance, which varies continuously with the capacitor voltage U_c can be described as

$$C(U_c) = C_0 + C_1 U_c. \tag{3.45}$$

To identify the parameters C_0 and C_1, experimental tests on the SuperCap are conducted. In Equation (3.45) it is assumed that the capacity is varying with the voltage according to $C(U_c) = \frac{dQ}{dU_c}|_{U'}$ for a given capacitor voltage U'. Integrating and solving for the total charge gives $Q = CU_c$, which is commonly known for conventional capacitors. Integrating the expression (3.45) with voltage gives

$$\int_0^{U_c} C(U_c) = Q = C_0 U_c + \frac{C_1 U_c^2}{2}. \tag{3.46}$$

Inserting $Q = CU_c$ in Equation (3.46) gives the final expression of the equivalent capacitance for expressing the total charge in a SuperCap

$$C_q = C_0 + \frac{C_1 U_c}{2}. \tag{3.47}$$

With this expression inserted in Equation (3.45), the term C_1 can be identified by

$$C_1 = \frac{2}{U_c}(\frac{Q}{U_c} - C_0) = \frac{2}{U_c}(\frac{I_c(t_f - t_i)}{U_c} - C_0) \tag{3.48}$$

where t_i and t_f denote the initial and final moments for the test. The parameter C_0 is identified by inducing a constant current for a small time range and measure the voltage difference according to $C_0 = I_c\frac{\Delta t}{\Delta U_c}$. The constant is determined to $C_0 = 2600$. The capacitor voltage can then be described as

$$U_c = U_c^0 - \frac{1}{(C_0 + C_1 U_c)} \int i_{sc}dt. \tag{3.49}$$

This gives the terminal voltage of the SuperCap

$$U_{sc} = U_c - R_{i,sc}i_{sc}, \tag{3.50}$$

where $R_{i,sc}$ is the internal resistance and i_{sc} is the main current to and from the SuperCap.

3.3   Battery model

An ideal accumulator would have constant voltage and a constant capacity independently from charge and current load. This is however not the case for batteries. As discussed in Chapter 2.2.2 and depicted in Figure 2.9, the voltage of a battery depends on the charge nonlinearly. Furthermore, the battery capacity also changes nonlinearly with the amount of current that is withdrawn. These effects are challenging to model. A promising approach is to model it with a kinetic battery model (KiBaM) [HSHB00]. One advantage with this modeling approach is that it is applicable to all types of batteries. Another advantage is that this approach regards self-discharging effects (that the open circuit voltage increases slightly when a load current is applied and then removed). A disadvantage is that it does not represent the sharp slopes in the beginning of a charging cycle well (as will be seen in the validation results) and that it does not regard temperature and aging effects.

The KiBaM model consists of two parts, a capacity model and a voltage model. The capacity model describes the charge of the battery and the charging- and discharging dynamics. The voltage model describes the voltage of the battery during load and idle sequences.

3.3.1   Capacity model

The principle of the capacity model is depicted in Figure 3.4. It is described as a two-tank system where tank 1 represents the instantly available charge which is not chemically bounded and tank 2 represents the chemically bounded charge stored in the battery which is realized through reversible electro-chemical reactions. From the width c and the height h_i of the tanks, the charges are calculated as

$$q_1 = h_1 c \tag{3.51}$$

and

$$q_2 = h_2(1 - c) \tag{3.52}$$

respectively. The withdrawn current is given as I_{bat} which also is the input variable to the model. The charging flow between the two tanks is described with $\dot{q}_2$ and

depends on the equivalently valve coefficient k^1 whereas the inner resistance of the battery is given by R_{bat}. Since the battery capacity depends on the actual current load, the maximum capacity h_{max}, which is achieved at low currents (here: $<1\,\text{A}$) is calculated with

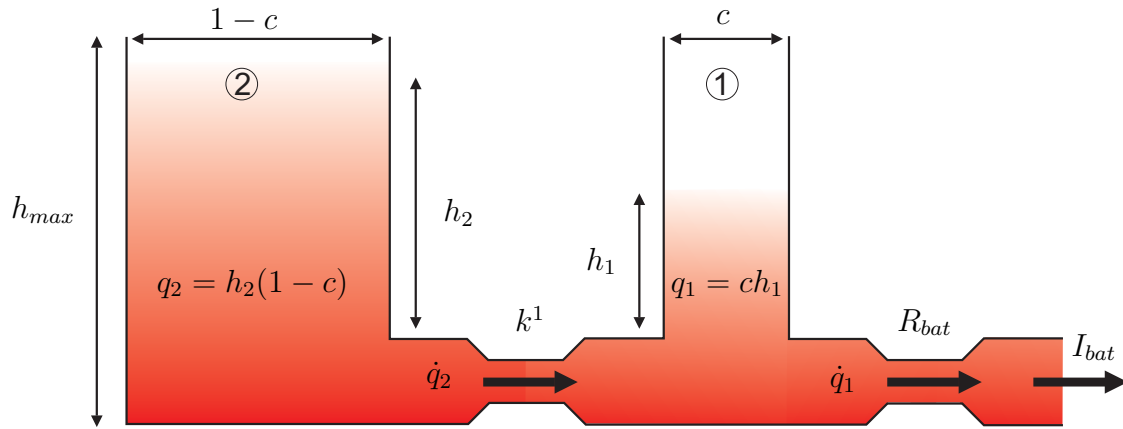$$q_{max} = q_{1,max} + q_{2,max} = ch_{max} + (1-c)h_{max} = h_{max}. \tag{3.53}$$

Figure 3.4: Sketch of the principle of the kinetic battery model (KiBaM) as a two-tank system with the chemically bounded charge represented by tank 2 and the immediately available charge by tank 1

The flow to and from the tanks is described with two differential equations of first order according to

$$\dot{q}_1 = -I_{bat} - \dot{q}_2 \tag{3.54}$$

and

$$\dot{q}_2 = k_1(h_1 - h_2). \tag{3.55}$$

Inserting Equation (3.51) and (3.52) and introducing a new constant $k = k_1/c(1-c)$ for eliminating denominators (for simplicity) gives finally the equations

$$\dot{q}_1 = -I_{bat} - k(1-c)q_1 + kcq_2 \tag{3.56}$$

and

$$\dot{q}_2 = k(1-c)q_1 - kcq_2. \tag{3.57}$$

The capacity model depends on the constants k, c, and q_{max}. These constants were determined experimentally as will be shown in Chapter 3.5.3.

3.3.2   Voltage model

The voltage model describes the typical voltage behavior of a battery during charging and discharging including the sharp nonlinear decreasing of the voltage at the end of the depletion of the charge. This is realized with the following description of the output voltage

$$E = E_0 + AX + CX/(D - X), \tag{3.58}$$

where E_0 denotes the open circuit voltage of the battery, A [V/Ah] denotes the initial voltage change during charging and discharging, C [V] and D [Ah] are parameters which describe the sharp voltage slopes at the end of a charge and discharge scenario respectively. The constant C is positive during charging and negative during discharging, D is always positive since it equivalently describes the maximum capacity of the battery. The time-dependent variable $X(t)$ describes the averaged charge at time t at which the battery is subjected for the current load I_{bat}. This can be described as

$$X(t) = \frac{q_{out}(t)}{q_{max}(I_{bat})} q_{max}, \tag{3.59}$$

where $q_{max}(I_{bat})$ denotes the maximum available capacity for a given current load and $q_{out}(t)$ denotes the net change of charge during a charge or discharge scenario. This charge is calculated from the integral of the current load

$$q_{out}(t) = \int_{t=0}^{t=T} I_{bat}(t)dt = q_{max} - q_1(T) - q_2(T). \tag{3.60}$$

The output voltage of the battery U_o is then calculated from

$$U_o = E - I_{bat}R_{bat}, \tag{3.61}$$

where R_{bat} denotes the inner resistance of the battery.

The voltage model is hence described from the constants E_0, A, C, D and R_{bat} which are experimentally determined in Chapter 3.5.3.

3.4   DC/DC-converter model

The usual main task in hybrid applications of a DC/DC-converter is to keep a constant output voltage despite of a varying input (supply) voltage for different loads, i.e. current outputs. The task is to control the output voltage to keep a constant value, especially for higher loads, low supply voltage, and fast transients. It is desirable to control the output voltage to follow a reference signal but this makes

the DC/DC-converter more complex and expensive. Another control variable could be the maximum current output that is allowed to be withdrawn. If higher currents are drawn the voltage is rapidly decreased and hence the maximum output power is kept. DC/DC converters are mainly categorized in three different types; buck, boost, and buck-boost converters [Eri99]. The buck converters reduce the output voltage in corresponding to the supply voltage and the boost converters increase the voltage output. The buck-boost converters can maintain the output voltage either in a higher or lower value to the supply voltage.

When a modeling circuit consists of one or several high-frequency power inverters (like a hybrid vehicle model), it can slow down the simulation time considerably. The fast changing modes of the circuit can force small simulation time steps in order to compute them accurately.
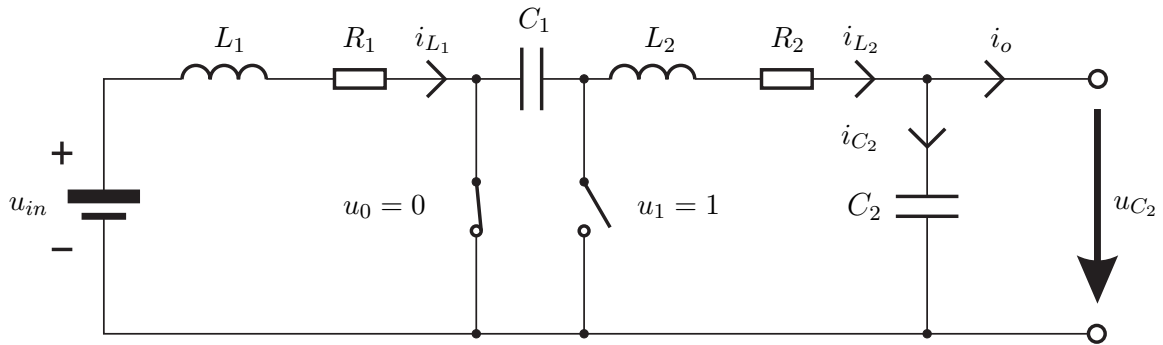
Figure 3.5: Circuit of a CUK DC/DC-converter with buck-boost behavior which includes two switches u_0 and u_1 and with output voltage u_{C_2}

A CUK-converter is shown in Figure 3.5. The equations yield in position $u_0 = 0$ and $u_1 = 1$

$$
\begin{aligned}
&u_{in} + u_{L_1} + u_{R_1} = 0 \quad \text{for } u_0 = 0 \text{ and after rearranging} \\
&\dot{i}_{L_1} = \frac{-R_1 i_{L_1}}{L_1} - \frac{u_{in}}{L_1}.
\end{aligned}
\tag{3.62}
$$

For the right hand side of the circuit yields

$$
\begin{aligned}
&u_{C_1} + u_{L_2} + u_{R_2} + u_{C_2} = \\
&u_{C_1} + \dot{i}_{L_2} L_2 + i_{L_2} R_2 + u_{C_2} = 0, \quad \text{and after rearranging} \\
&\dot{i}_{L_2} = -\frac{u_{C_1}}{L_2} - \frac{u_{C_2}}{L_2} - \frac{i_{L_2} R_2}{L_2},
\end{aligned}
\tag{3.63}
$$

where the voltages over the conductors C_1 and C_2 are given by

$$
\begin{aligned}
\dot{u}_{C_2} &= \frac{i_{C_2}}{C_2} \quad \text{and} \\
\dot{u}_{C_1} &= \frac{i_{L_2}}{C_1}.
\end{aligned}
\tag{3.64}
$$

Setting up these equations in a state-space representation gives the system matrix, when the switches are in position $u_0 = 0$ and $u_1 = 1$ as

$$
A_1 = \begin{bmatrix}
-\frac{R_1}{L_1} & 0 & 0 & 0 \\
0 & -\frac{R_2}{L_2} & -\frac{1}{L_2} & -\frac{1}{L_2} \\
0 & \frac{1}{C_1} & 0 & 0 \\
0 & \frac{1}{C_2} & 0 & 0
\end{bmatrix}.
\tag{3.65}
$$

For the case when the switches are in position $u_0 = 1$ and $u_1 = 0$, the equations are calculated equivalently and become

$$
\begin{aligned}
\dot{i}_{L_1} &= -\frac{R_1}{L_1}i_{L_1} - \frac{1}{L_1}u_{C_1} + \frac{1}{L_1}u_{bat}, \\
\dot{i}_{L_2} &= -\frac{R_2}{L_2}i_{L_2} - \frac{1}{L_2}u_{C_2}, \\
\dot{u}_{C_1} &= \frac{1}{C_1}i_{L_1}, \quad \text{and} \\
\dot{u}_{C_2} &= \frac{1}{C_2}i_{L_2}.
\end{aligned}
\tag{3.66}
$$

The second system matrix becomes

$$
A_2 = \begin{bmatrix}
-\frac{R_1}{L_1} & 0 & -\frac{1}{L_1} & 0 \\
0 & -\frac{R_2}{L_2} & 0 & -\frac{1}{L_2} \\
\frac{1}{C_1} & 0 & 0 & 0 \\
0 & \frac{1}{C_2} & 0 & 0
\end{bmatrix}.
\tag{3.67}
$$

The switching ratio D between both systems is defined as the duty time $D = \frac{t_{on}}{t_{off}}$ ranging from 0 to 1, the equations can be merged into

$$
\dot{i}_{L_1} = (-\frac{R_1}{L_1}i_{L_1})D + (-\frac{R_1}{L_1}i_{L_1} - \frac{1}{L_1}u_{C_1})(D-1) + \frac{1}{L_1}u_{bat},
\tag{3.68}
$$

respectively after rearranging

$$
\begin{aligned}
\dot{i}_{L_1} &= \frac{u_{C_1}}{L_1}D - \frac{u_{C_1}}{L_1} - \frac{R_1 i_{L_1}}{L_1} + \frac{u_{bat}}{L_1}, \\
\dot{i}_{L_2} &= -\frac{u_{C_1}}{L_2}D - \frac{R_2 i_{L_2}}{L_2} - \frac{u_{C_2}}{L_2}, \\
\dot{u}_{C_1} &= \frac{i_{L_2}}{C_1}D + \frac{i_{L_1}}{C_1} - \frac{i_{L_1}}{C_1}D, \quad \text{and} \\
\dot{u}_{C_2} &= \frac{i_{L_2}}{C_2}.
\end{aligned}
\tag{3.69}
$$

After merging both system equations, the total state-space representation of the DC/DC-converter is given by

$$
A_{tot} = A_1 D + A_2(1-D) = \begin{bmatrix} -\frac{R_1}{L_1} & 0 & \frac{D-1}{L_1} & 0 \\ 0 & -\frac{R_2}{L_2} & -\frac{D}{L_2} & -\frac{1}{L_2} \\ \frac{1-D}{C_1} & \frac{D}{C_1} & 0 & 0 \\ 0 & \frac{1}{C_2} & 0 & 0 \end{bmatrix}. \tag{3.70}
$$

This gives the state equation representation as

$$
\dot{x} = \begin{bmatrix} -\frac{R_1}{L_1} & 0 & \frac{D-1}{L_1} & 0 \\ 0 & -\frac{R_2}{L_2} & -\frac{D}{L_2} & -\frac{1}{L_2} \\ \frac{1-D}{C_1} & \frac{D}{C_1} & 0 & 0 \\ 0 & \frac{1}{C_2} & 0 & 0 \end{bmatrix} \begin{bmatrix} i_{L_1} \\ i_{L_2} \\ u_{C_1} \\ u_{C_2} \end{bmatrix} + \begin{bmatrix} \frac{1}{L_1} \\ 0 \\ 0 \\ 0 \end{bmatrix} u_{bat}. \tag{3.71}
$$

Since all states are considered being measured, the output equations become

$$
y = \begin{bmatrix} 1 & 0 & 0 & 0 \\ 0 & 1 & 0 & 0 \\ 0 & 0 & 1 & 0 \\ 0 & 0 & 0 & 1 \end{bmatrix} \begin{bmatrix} i_{L_1} \\ i_{L_2} \\ u_{C_1} \\ u_{C_2} \end{bmatrix}. \tag{3.72}
$$

Note that the battery voltage here is considered as input to the system. The duty ratio D is in real applications the actual input to DC/DC-converters since it defines the output voltage of the converter. As it can be seen from the system description above, having the duty ratio D as a variable the system appears as nonlinear. By linearizing at a point D_o, it is possible to implement a full state-feedback controller based on pole placement or linear quadratic optimization rules. This requires that the battery voltage u_{bat} works as input to the system. When regarding the nonlinear system the state equation is given as

$$
\dot{x} = \begin{bmatrix} -\frac{R_1}{L_1} & 0 & -\frac{1}{L_1} & 0 \\ 0 & -\frac{R_2}{L_2} & 0 & -\frac{1}{L_2} \\ \frac{1}{C_1} & 0 & 0 & 0 \\ 0 & \frac{1}{C_2} & 0 & 0 \end{bmatrix} x(t) + \begin{bmatrix} 0 & 0 & \frac{D}{L_1} & 0 \\ 0 & 0 & -\frac{D}{L_2} & 0 \\ \frac{-D}{C_1} & \frac{D}{C_1} & 0 & 0 \\ 0 & 0 & 0 & 0 \end{bmatrix} x(t) + \begin{bmatrix} \frac{1}{L_1} \\ 0 \\ 0 \\ 0 \end{bmatrix} u_{bat}, \tag{3.73}
$$

where D denotes the input signal and u_{bat} can be considered as constant (although it is changing in a real system). The first term regards the linear part of the system and the second part describes the nonlinearities in the system due to the duty cycle D.

3.5   Validation of the component models

In this section, the simulation and validation results of the modeled components are presented. Each validation experiment will be described, the identification procedure will be illustrated with examples and important observations will be discussed.

3.5.1   Validation of the fuel cell model

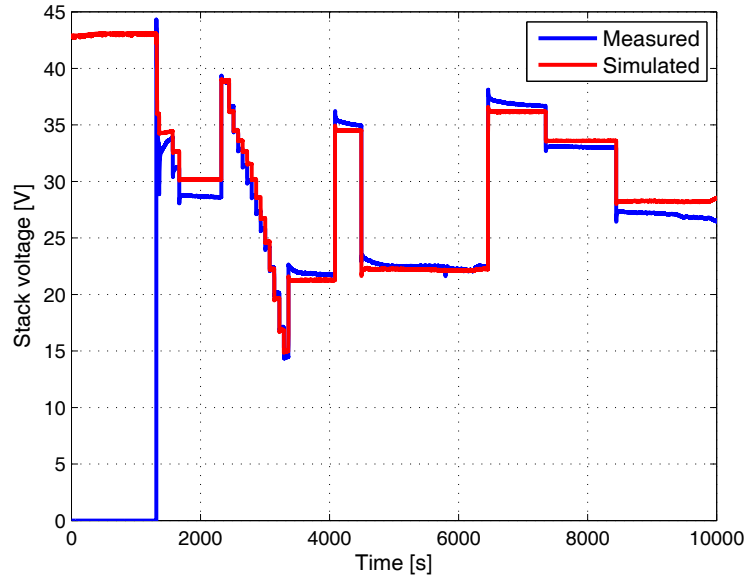The fuel cell stack considered here is shown in Figure 2.6. The components were modeled and validated separately and the results of the validation are presented next.

Figure 3.6: Validation of the electrical behavior by comparison of simulated and measured time behavior of a current input profile

Validation of the stack model

For practical validation, the fuel cell stack behavior is considered for 10 000 s. The mass flow rate of the air and hydrogen entering the stack, the corresponding pressures $p_{ca,in}$ and $p_{an,in}$, as well as the stack temperature T_{fc} are measured. The stack voltage of the real fuel cell stack v_{st} is the measured variable for the model validation to be compared to. The measured and simulated voltage for an arbitrary current load are depicted in Figure 3.6. During the warm-up of the fuel cell (0-1 300 s) the stack voltage of the real fuel cell stack is not measured.

Validation of the air supply model

For validating the air blower model, a test rig was set up as depicted in Figure 3.7. The blower is driven by a brushless DC-motor. The blower speed ω_{cp}, the blower torque τ_{cp}, the motor current i_{cm}, the blower air mass flow $W_{cp,out}$, the outlet temperature $T_{cp,out}$, and the exit air pressure $p_{cp,out}$ are measured with the corresponding sensors shown in Figure 3.7. Experiments are realized using a DSP system, where the input voltage to the blower motor v_{cm} is given and measured variables are observed and controlled. In order to vary the outlet pressure $p_{cp,out}$, a manually adjustable pressure regulating valve is used. The applied blower from Ballard [Bal09] belongs
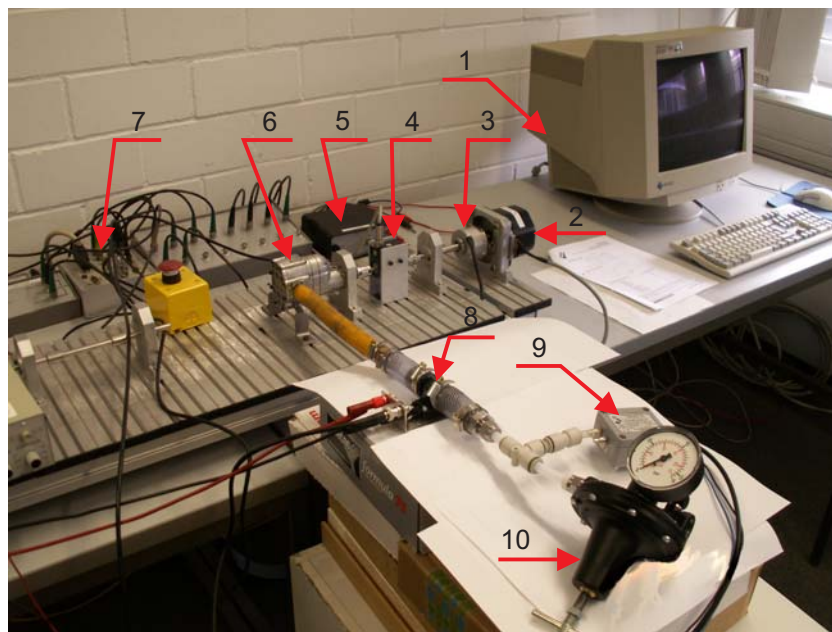
Figure 3.7: Test rig used for validation of the blower model at the University of Duisburg-Essen. 1. Interface, 2. Brushless DC-motor, 3. Rotary speed sensor, 4. Torque sensor, 5. Current sensor, 6. Blower, 7. DSP system, 8. Air mass flow and temperature sensor, 9. Pressure sensor, 10. Pressure regulating valve

to the category of the roots blowers and consists of two oval shaped lobe rotors inside the housing. One rotor is the driving rotor driven by the motor, while the other rotor is driven by a pair of gears with the same gear ratio. For this reason, both rotors rotate with the same speed but reversely [KMD02]. First, the air enters the inlet side of the housing and between both rotors. As the rotors rotate towards the outlet side, the air is pushed against the housing of the blower. On the outlet side, the air is compressed up to the system pressure and forced out. During each rotation, four volumes are displaced. During the total working process, the air is only moved from the inlet side to the outlet side of the blower and there is no

volume change of the air within the housing. One advantage of the air blowers is that large amounts of air can be displaced in the lower speed regions. However, a disadvantage of the roots blowers is that the thermal efficiency η_{cp} is low compared to e.g. centrifugal and screw blowers [KMD02].

For validation, the experiments are carried out in two steps: Firstly, the blower is physically disconnected and the motor parameters are identified and separately validated. Secondly, the blower is connected and the blower parameters are identified based on measured data. During the experiment, the input voltage v_{cm} was incrementally increased from 2.4 V to 16.8 V with 2.4 V steps. The blower speed ω_{cp} increases respectively from 300 to 2100 rpm with an increment of 300 rpm. The outlet pressure $p_{cp,out}$ is manually adjusted with an increment of 10 mbar at each speed region.

The task of this step is to determine the constants of the static blower map a_i, b_i, d_i, e_i, and f_i for $i = 1, 2, 3$. According to Equations (3.23)-(3.28), the constants a_i and b_i describe the relation between the dimensionless parameter Ψ, the normalized mass flow rate Φ, and the Mach number Ma of the air entering the blower, while the constants d_i, e_i, and f_i denote the relation between the blower efficiency η_{cp}, the normalized mass flow rate Φ, and the Mach number. First, the parameters a_i, b_i, d_i, e_i, and f_i, the dimensionless variable Ψ, the normalized mass flow rate Φ, the Mach number, and the blower efficiency η_{cp} are determined. The dimensionless head parameter Ψ can be calculated with Equation (3.26) and the Mach number Ma of the air entering the blower by Equation (3.25). The reference values of the normalized mass flow rate Φ and the blower efficiency η_{cp} can be calculated with Equation (3.20) and (3.38) to

$$\Phi_{ref} = \frac{4W_{cr}}{\rho_a \pi d_c^2 U_{cp}} \tag{3.74}$$

and

$$\eta_{cp,ref} = \frac{C_{p,a} W_{cp,out} T_{cp,in}}{\omega_{cp} \tau_{cp}} \left(\left(\frac{p_{cp,out}}{p_{cp,in}} \right)^{\frac{\gamma_a - 1}{\gamma_a}} - 1 \right), \tag{3.75}$$

where the mass flow rate across the blower $W_{cp,out}$, the bower speed ω_{cp}, the torque to drive the blower τ_{cp}, and the pressure of the air leaving the blower $p_{cp,out}$ are measured and the blower diameter d_c is known. In Equation (3.74), the blower blade-tip speed U_{cp} can be calculated with Equation (3.21) and (3.22). The other parameters in Equation (3.74) and (3.75) are assumed as constant. After determining the reference values of the normalized mass flow rate Φ_{ref} and the blower efficiency η_{cp}, the identification of the other parameters can be conducted. In order to identify the parameters $k_{i=1,2,3}$ in Equation (3.23), a least square curve fitting approach is applied. The model error e_i is defined by

$$e_i = y_{ref}(x_i) - y(x_i), \quad i = 1, 2, \ldots, n, \tag{3.76}$$

where $y_{ref}(x_i)$ is the reference value from measurements at x_i and $y(x_i)$ the simulation result. The simulation results in this case are calculated with the simulated normalized blower flow rate from Equation (3.23) with the input vector Ψ and the vector k_i of the model. The goal of the iteration algorithm is to minimize J_e, as the sum of the squared errors between reference and measurement, defined by

$$J_e = \sum_{i=1}^{n} e_i^2, \tag{3.77}$$

where n is the number of measurements. The goal of the identification process is to determine the optimal combination vector of the tuning parameters $k_{i,opt}$, so that J_e is minimized. During this process, the elements of the unknown parameter vector k_i have to be changed, until J_e reaches a minimum (or limit) as a break condition. Using the command *fminsearch* in Matlab® such optimization process can be conducted. The approximation results of the factors are shown in Figure 3.8 (a)-(c). The values of Φ as a function of Ψ and ω_{cp} calculated with the blower map model are graphically depicted in Figure 3.9 (a). The blower efficiency η_{cp} is depicted in Figure 3.9 (b).

Finally, using the blower model with its identified parameters, an experiment is conducted to validate the model. The input blower voltage v_{cm} is changed with series of voltage steps and applied as input. The comparison between measured and simulated data is shown in Figure 3.10. It is obvious that the dynamics of the blower speed (top figure), air flow (middle figure), and motor current (bottom figure) can be well represented with the air supply system model.

Validation of the temperature model

Using Equation 3.39, the model of the temperature dynamics of the fuel cell stack are determined. The identification of the unknown model parameters are done from the same experiment as the validation for the stack model. In the mentioned experiment, the stack current, the mass flow rate, and the pressure of the air and the hydrogen entering the fuel cell stack are measured by the corresponding sensors and given to the model as inputs. The stack temperature is also measured with a temperature sensor. The comparison between the simulation results and the measurements are shown in Figure 3.11. The figure shows that the temperature model represents well the temperature dynamics in the fuel cell stack to the stationary behavior after 1000 sec. During the warm-up phase (before 1000 sec), the difference between the measurements and simulation results is relative large.

3.5.2   Validation of the SuperCap model

How to model and identify the parameters is outlined and explained here. First, the inner resistance parameter $R_{i,sc}$, as depicted in Figure 3.3 is identified by discharging

(a) Estimation of k_1

(b) Estimation of k_2

(c) Estimation of k_3

(d) Estimation between Φ and Ψ
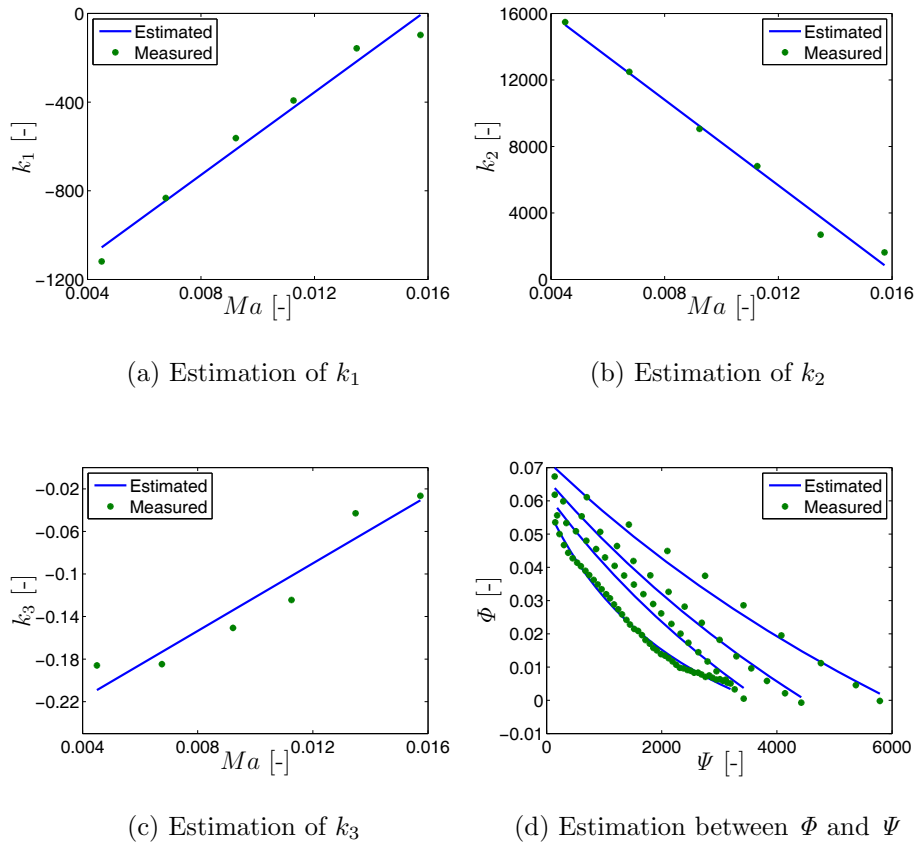
Figure 3.8: Estimation of the parameters k_1, k_2, k_3, Φ, and Ψ

(a) Parameters Φ, Ψ, and ω_{cp}

(b) Blower efficiency map
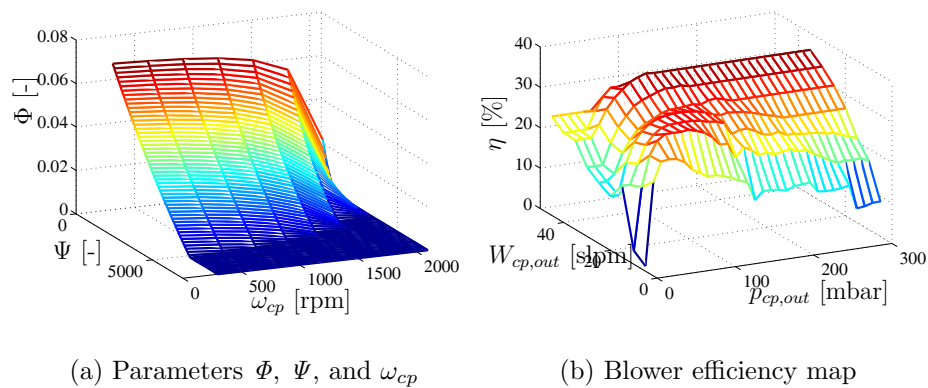
Figure 3.9: Left: Estimation of the parameters Φ and Ψ as a function of rotation speed. Right: Efficiency map of the blower
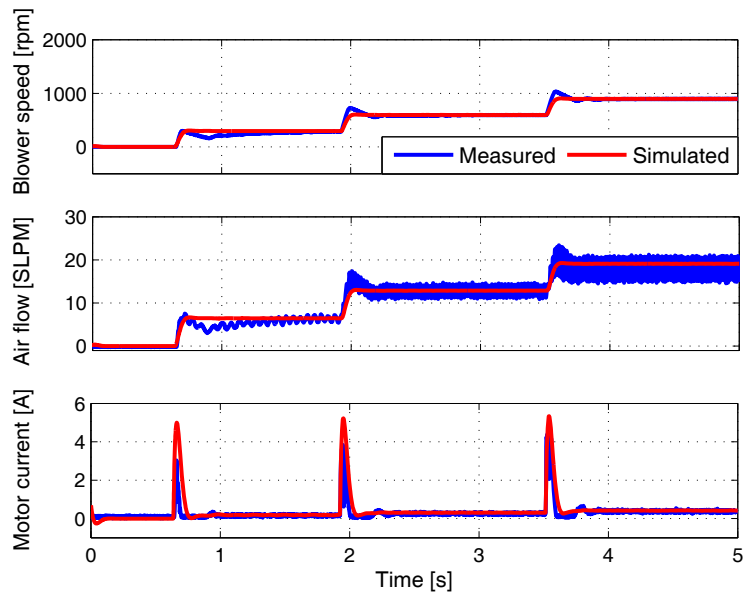
Figure 3.10: Validation of the dynamical behavior of the blower by comparison of the rotation speed, air flow, and motor current.
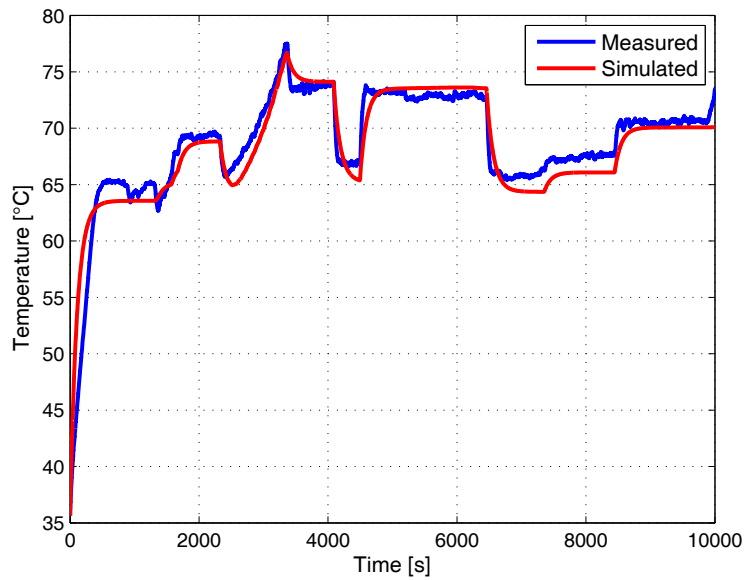
Figure 3.11: Validation of temperature dynamics model

the SuperCap with a high step current and then calculated as $R_{i,sc} = \frac{\Delta U_c}{\Delta i_{sc}}$ [ZB98]. The value was determined to $R_{i,sc} = 0.012$ Ohm. The validation of the model is depicted in Figure 3.12 where a constant current of 3 A first charging the SuperCap and then being discharged with a 30 A constant current.
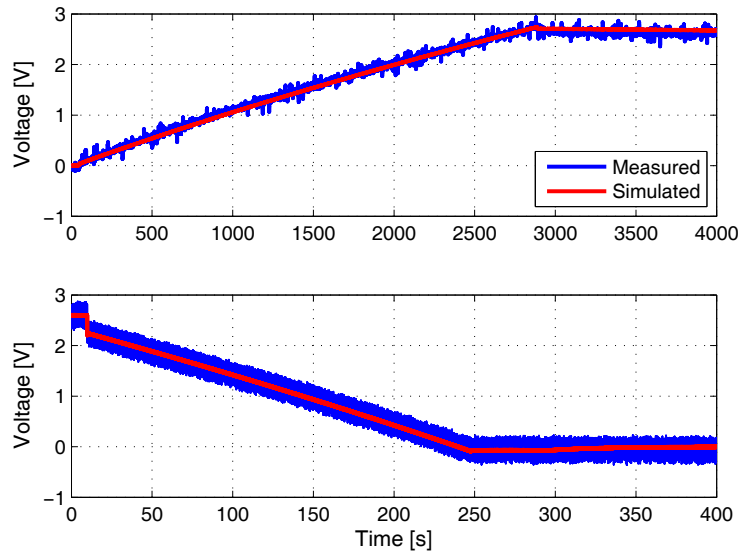
Figure 3.12: Validation of the SuperCap model. Above figure shows the charging with 3A and bottom figure shows discharging with 30A.

3.5.3   Validation of the battery model

In this section the parameters of a battery model are determined experimentally. Lead-batteries with rated voltage of 12 V and 14 Ah from company Exide Technologies GmbH [EXI09] were used to validate the model on. Several tests were conducted whereas the voltage and current were measured. The battery was tested with different constant charge and discharge currents. The output voltage was kept within the safety instructions of a lead-battery and hence was not allowed to exceed 14.1 V (2.35 V per cell) and not fall below 10.8 V (1.8 V per cell). Therefore, the charge and discharge current could vary in the beginning respectively in the end of each test. However, the measured current was used on the battery model as input and the measured voltage output is used for validation.

Since the variables of the voltage model are directly dependent on the parameters and variables of the capacity model, the parameters of the capacity model are determined first. Before that, the inner resistance is determined. A step current is

taken from the battery and within a short time interval the internal resistance is determined as

$$R_{bat} = \frac{\Delta U_{bat}}{\Delta I_{bat}}. \tag{3.78}$$

Because the resistor has no dynamics, a fall of voltage is monitored with the same time interval as the current output. It is important to choose the time interval as short as possible due to that other effects (such as the self-charging effect) can occur and mislead the results. Several tests were made and the inner resistance is determined to $R_{bat} = 0.08\,\Omega$.

Capacity parameters

Next, the parameters k, c, and q_{max} from the capacity model are determined. The constant maximum capacity q_{max} is determined by withdrawing a small constant current amount from a fully charged battery. It is necessary to apply a small current load in order not to develop large heating losses which can decrease the capacity of the battery. A current of $1\,A$ was withdrawn and the constant maximum capacity is calculated to q_{max}=110 483 As (approx. 30 Ah).

In most batteries, the current-dependent maximum capacity $q_{max,I}(I_{bat})$ is usually given in the specifications. Here, it is determined experimentally. Four tests are conducted with different current loads, with 1, 2, 4, and 5 A, and the current-dependent maximum capacity is estimated with a polynomial fit in tool in Matlab. The polynomial fit as function to the total charge/discharge time is depicted to the measured results in Figure 3.13.

These parameters are identical during charging and discharging. By using curve-fitting methods the goal is to minimize the criterion

$$Error = \left(F_{t_1,t_2} - F_{data}\right)^2. \tag{3.79}$$

Since the idea of this modeling technique is to model any given battery as easily as possible, only two charging/discharging measurements are realized. It will be shown later on that it is sufficient although even better results could be achieved by charging/discharging with even more currents. Another reason is that the lead-batteries used here should not be subjected to a large amount of current cycles since aging effects could change the results. Aging effects are, as already stated, not regarded in this model. The two measurements, one small and one high current measurement were 1 A and 5 A respectively. The parameter F_{t_1,t_2} denotes the ratio between an instant capacity of the battery for an arbitrary current load (here 5 A) to the maximum capacity at which a small current is drawn (here 1 A). The smaller current $I_{T=t_1}$ which totally depletes the battery at time t is calculated as

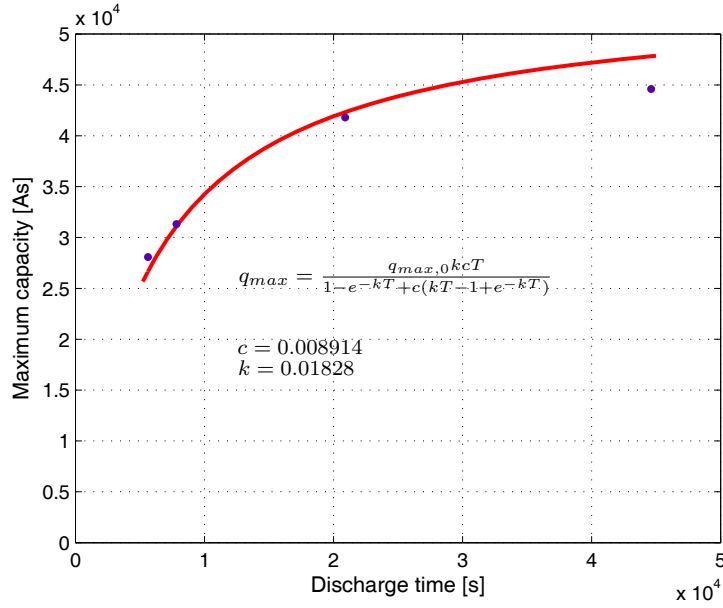$$I_{T=t_1} = \frac{kcq_{max}}{1 - e^{-kt} + c(kt - 1 + e^{-kt})}. \tag{3.80}$$

Figure 3.13: The polynomial fit of the maximum current-dependent capacity of a single lead-battery. Coefficients are estimated to $c = 0.008914$ and $k = 0.01828$.

Voltage parameters

The voltage model takes the sharp changes in the voltage outputs in the beginning and in the end of a fully charging/discharging scenario. The equation

$$E = E_0 + AX + CX/(D - X) \tag{3.81}$$

describes the output voltage of the battery without regarding the inner resistance. The constant E_0 [V] describes the open circuit voltage of the battery when fully charged. The constant A [V/Ah] corresponds to the linear slope of the voltage behavior during charging and discharging. The parameters C [V] and D [Ah] describe the sharp changes in the voltage output in the beginning and the end of a charging and discharging scenario. A smaller value of C gives a sharper slope and the parameter changes sign depending on charging or discharging. The parameter D is always positive and is closely corresponding to the maximum capacity of the battery. The variable X is the normalized charge that is withdrawn or given to the battery at an arbitrary time and is described with

$$X(t) = \frac{q_{out}(t)}{q_{max}(I_{bat})} q_{max}. \tag{3.82}$$

It is always positive and has a value between the momentarily charge flow $q_{out}(t)$ and the maximum charge q_{max}.

The variable $q_{max}(I)$ current-dependent maximum capacity for an arbitrary current and the constant q_{max} describes the maximum capacity of the battery. The variable $q_{out}(t)$ is the total charge flow at an arbitrary time with respect to that the battery is fully charged initially. It is described with

$$q_{out} = \int I(t)dt = q_{max} - q_1(t) - q_2(t). \tag{3.83}$$

For identification of the parameters, it is regarded that E_0, A, C and D are determined separately during charging and discharging respectively. For discharging the parameters were $E_{0,d} = 12.87\,\text{V}$, $A_d = $ -0.1086 V/Ah, $C_d = $ -0.04398 V, and $D_d = 14.13\,\text{Ah}$. For charging $E_{0,c} = 13{,}79\,\text{V}$, $A_c = $ -0,1066 V/Ah, $C_c = 0{,}6154\,\text{V}$ and, $D_c = 30\,\text{Ah}$.

The validation was done on three identical lead-batteries connected in series and parallel. The parameters that were identified for a single battery are scaled accordingly. The reason for validating on three connected batteries is due to the need for higher voltage and capacity on the HiL test rig and its applications. A single battery is not sufficient for the power demands required in the load-profiles implemented. The validation results for three in series connected lead-batteries are depicted in Figure 3.14. The charging and discharging results for 2 A are shown. As can be seen the model is more accurate during discharging than charging. This depends on the value of D that causes a very sharp increase in the output voltage function E when the battery approaches full charge due to division by zero as can be seen in Equation (3.81). Increasing the value of D gives better fit in the end of a charging scenario but decreases the accuracy in the beginning. Hence, a compromise must be made. But in general it is inevitable to have better results during discharging than during charging.

When three lead-batteries were connected in parallel, the parameters were scaled accordingly and the validation results are depicted in Figure 3.15. Likewise here, the validation is more accurate during discharging than during charging. Especially, in the beginning and in the end of the charging scenario. It will be shown in Chapter 5 that lead-batteries are not suitable for highly dynamical load profiles (like the one used here). Hence, the batteries and the respective models are not further detailed.
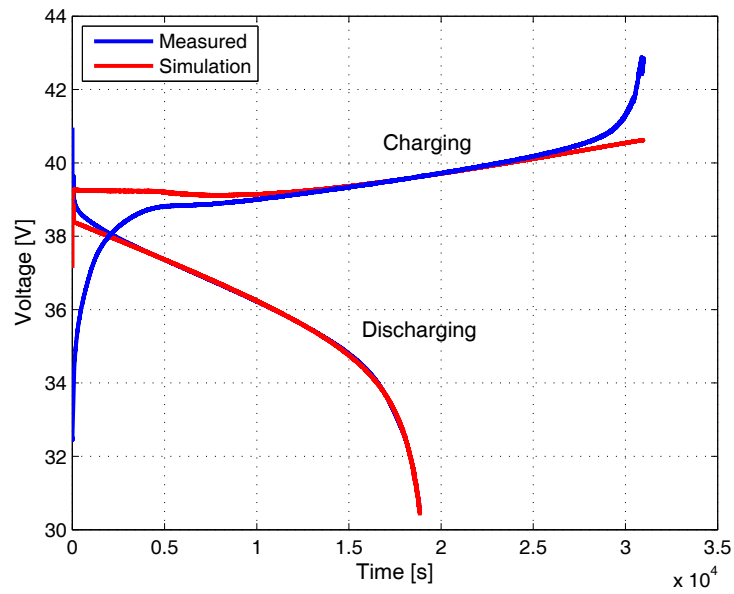
Figure 3.14: Charging and discharging behavior with 2 A for three lead-batteries connected in series
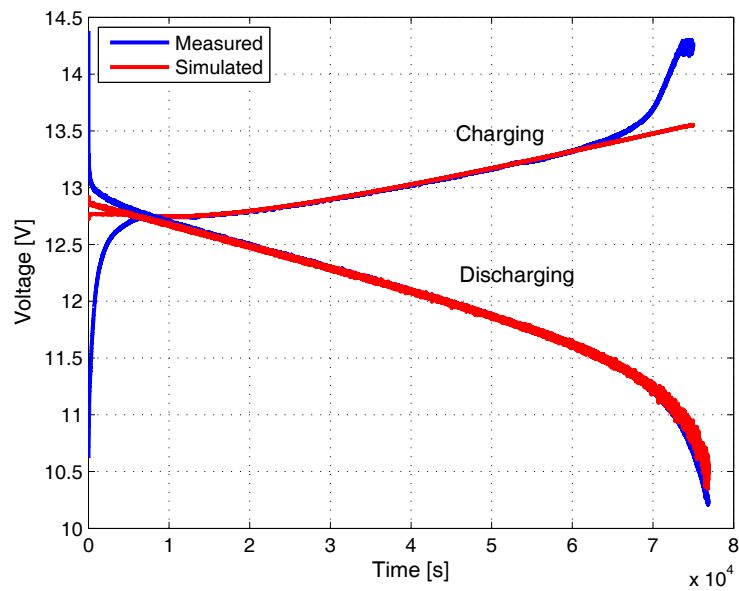

Figure 3.15: Charging and discharging behavior with 2 A for three lead-batteries connected in parallel

3.5.4 Validation of the DC/DC-converter

Although three DC/DC-converters are used in the test rig, only one is modeled and parameterized to be validated due to the similar behavior and power ranges between them. The sizes of the inductance and capacitance part of the DC/DC-converter are not identified correctly. There are two reasons: firstly, there were no possibility to conduct direct measurements inside the DC/DC-converter; secondly, the sizes for the inductance and capacitance parts are usually in micro-level for smaller DC/DC-converters [FM98]. This would increase the time constants of the system remarkably and hence require sample times in micro seconds and slow down the simulation times dramatically. For the sample time of milliseconds to be used, it is hence necessary to assume large values of the inductance and capacitance. Consequently, the simulation time is reduced without strongly affecting the modeling accuracy. Using a static model for the DC/DC-converter would simplify the models considerably and eliminate the need of a controller for the voltage output. However, this would introduce an algebraic loop to the model.

Algebraic loops in simulation models are when the solution (output) from a block is directly fed back to the input of the same block, if the block is a static block and contains no dynamics. This is also the case if the solution goes through several static blocks and then feeded back again. Algebraic loops slow down the simulation time considerably since the solution must be calculated with iterative methods which sometimes even diverge. Then, the simulation cannot be conducted. In this model the algebraic loops would be through the fuel cell model since there is a static relationship between input and output. If a static DC/DC-converter model would be inserted, the output of the converter would be feeded back to the fuel cell model and hence cause an algebraic loop when the output is given to the converter model.

Two inputs, load current, and supply voltage (depicted in Figure 3.16) are given to the model and two outputs (depicted in Figure 3.17) are compared to measured data of the DC/DC-converter. As can be seen, the results are satisfyingly.
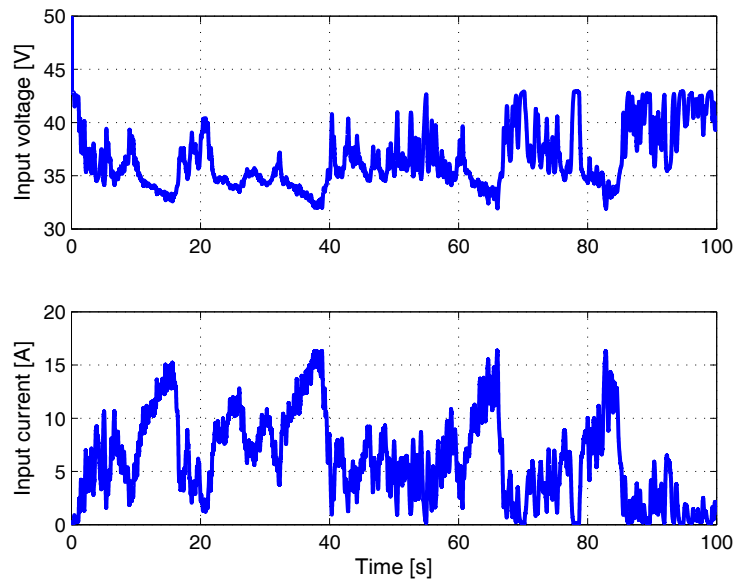
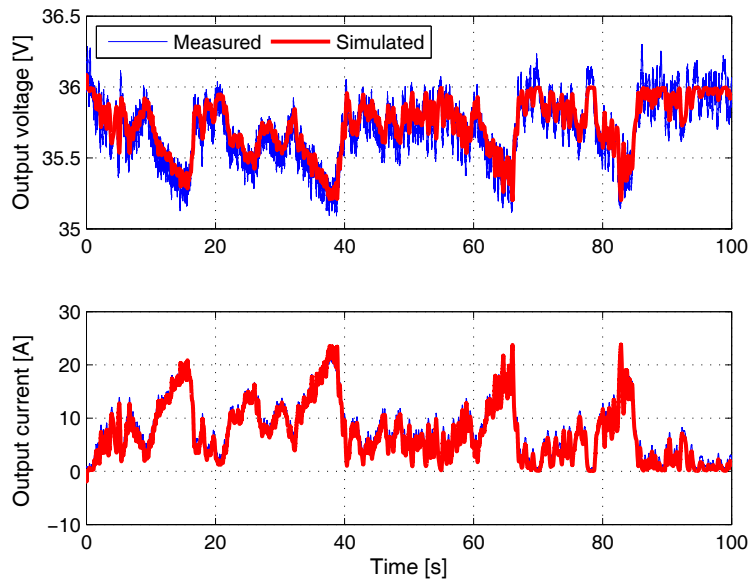Figure 3.16: Input signals for the validation of the DC/DC-converter

Figure 3.17: Validation of the voltage and current outputs of the DC/DC-converter

3.5.5   Validation of the hybrid system

After the models are individually validated for different inputs, the whole system with all components is put together with the inputs/outputs shown in Figure 3.18. The measured current flow from/to the electric motor is given as input and the simulation results are directly compared to the measured data. The controller of the DC/DC-converter is adjusted empirically to suit the behavior of the DC/DC-converter in the test rig because no information was available on what kind of controller was used on the actual DC/DC-converter. In Figure 3.19, the simulated and measured bus voltage (which is the output of the DC/DC-converter) is depicted. A small offset difference is noted but is neglected. Ripples on the measured data are due to sensor disturbances. The current flows between the components are depicted in Figure 3.20 respectively.
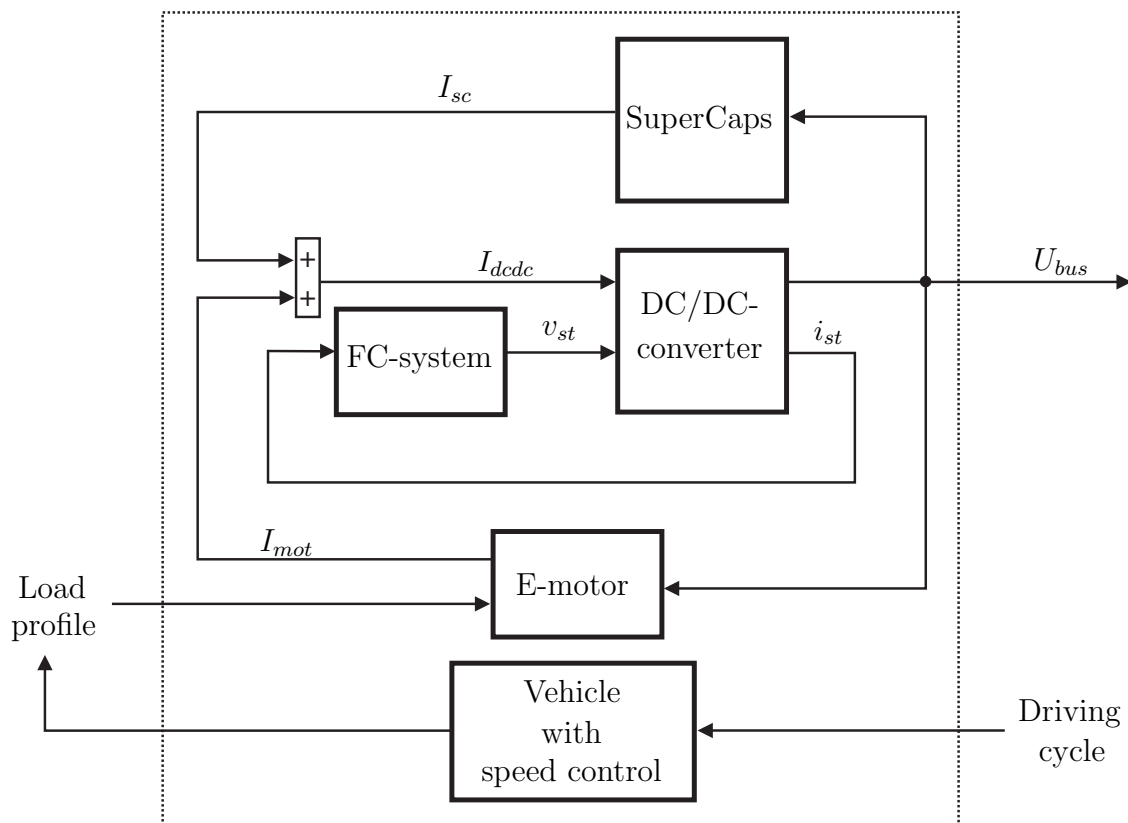
Figure 3.18: Block diagram of the modeled hybrid system with corresponding inputs and outputs of the sub-models
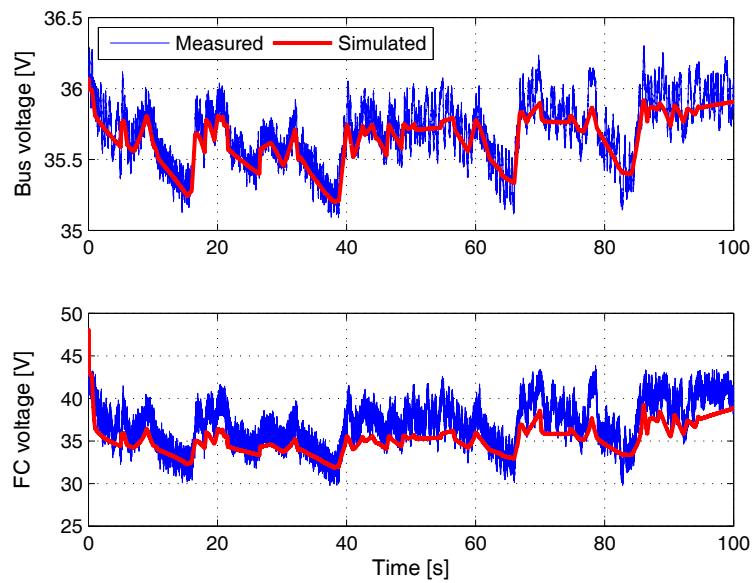
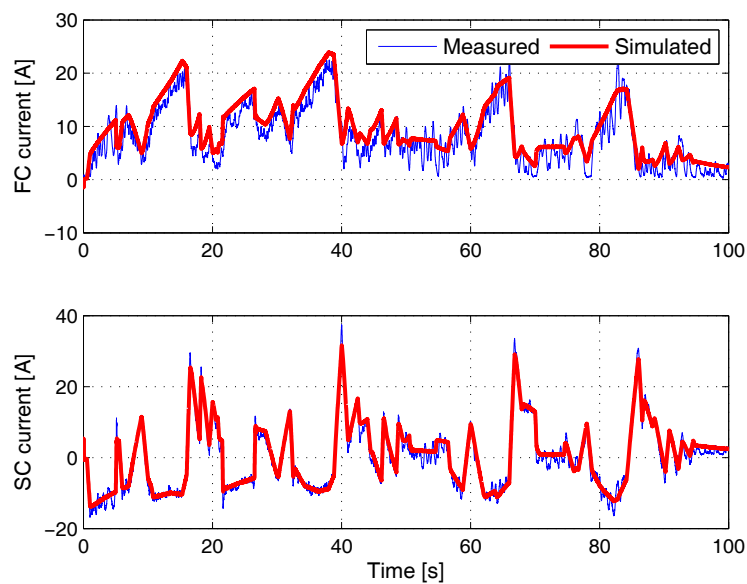Figure 3.19: Validation of the voltage outputs of the SuperCaps and fuel cell stack

Figure 3.20: Validation of the current outputs of the SuperCaps and fuel cell stack

4 Control of hybrid system components

In this chapter, control aspects of fuel cell-based hybrid systems will be presented and implemented in the developed models. The system components to be controlled are the fuel cell system, the DC/DC-converters, and the drive-motor due to their unstable behavior and with respect to the robustness and performance properties.

For the fuel cell system three different control methods are compared, a novel approach using gain scheduling control is introduced and compared with known control approaches in the field of fuel cells.

The control of DC/DC-converters depends on the type of converter that needs to be controlled. Here, due to the switching behavior it will be shown that state-feedback control can be used based on the state-space averaging models developed in Chapter 3.4.

The drive-motors torque or speed follows a reference signal. Here, a driver model is developed that follows a given speed driving-cycle. The driver model gives a voltage as input to the drive-motor realizing the driving-cycle. So the controller of the drive-motor is designed to follow speed profiles as well as possible.

It is assumed that all states are measured. Otherwise the usage of observers is possible and makes the design of the introduced kind of control approach possible.

4.1 Control of fuel cell systems

Control of fuel cells is a demanding task due to their nonlinearities. A proper control increases the fuel cell system efficiency and decreases the risk of oxygen starvation [ZLYO08]. In [PSP04] some control concepts are compared to each other. These are static and dynamic feed-forward and state feedback based on a linearized model of the fuel cell system. The conclusion is that state-feedback control shows better results than static and dynamic feed-forward in avoiding oxygen starvation. However, no nonlinear approaches were tested here. In [GCLP04], another dynamic feed-forward control approach is introduced that shows better results than static feed-forward. Also here, the controller is developed based on a linearized model at a single nominal working point. Some papers introduce nonlinear approaches such as exact feedback linearization in [NGD07] and flatness-based control in [DWAH08]. The feedback linearization method used is developed on a simplified fuel cell model and shows lack of robustness towards modeling errors. Applying feedback linearization on a detailed fuel cell model increases the complexity significantly. Flatness-based control showed better results than feed-forward but was not applied on analytically models of the fuel cell due to its complexity. Gain-scheduling control, based on state feedback should decrease the complexity of dealing with nonlinearities due to the

linearization of the model in several working points. This gives the simplicity of developing a controller based on linear systems together with the advantages of increased performance from nonlinear controllers. A review of gain-scheduling control is given in [LL00] and has not yet been implemented on fuel cells.

4.2   Control of the fuel cell system

Three different control approaches are compared to each other, i.e. static feed-forward, state-feedback, and gain-scheduling control. The latter of the methods is a novel approach and applied on a detailed nonlinear fuel cell system model here for the first time. The dynamical behavior of a fuel cell system is described by using a multiple-input-multiple-outputs (MIMO) state space representation. The inputs to the fuel cell system are

- the stack current i_{st},

- the blower input voltage v_{cm}, and

- the hydrogen input mass flow $\dot{m}_{H_2}$.

The outputs are

- the stack voltage v_{st} and

- the oxygen excess ratio λ_{O_2}.

As introduced in Chapter 3.1, the stack current appears as disturbance. The hydrogen input mass flow $\dot{m}_{H_2}$ is controlled separately to minimize the pressure difference between anode and cathode. The blower motor input voltage v_{cm} is the input variable able to affect the fuel cell dynamics behavior, due to that the blower speed determines the oxygen input flow and hence, directly influences the oxygen excess ratio λ_{O_2}. Consequently, oxygen starvation can be avoided. Oxygen starvation occurs when the partial pressure of oxygen falls below a critical level at any possible location within the meander of the air stream in the cathode. This can occur during a sudden current step output. A severe oxygen starvation can cause a short cut and a hot spot on the surface of the membrane and cause irreversible damages to the membrane, so one of the control objectives is to avoid oxygen starvation and to keep the output oxygen excess ratio at an optimal level or to realize only dynamically smooth behaviors.

4.2.1 Efficiency constraint

The net efficiency of the fuel cell system is calculated with

$$\eta_{net} = \frac{P_{net}}{W_{H_2,reacted}\Delta H_{h,H_2}}100\%, \tag{4.1}$$

where P_{net} denotes the net power of the fuel cell system, $W_{H_2,reacted}$ the mass flow rate of the reacted hydrogen, and $\Delta H_{h,H_2}$ denotes the higher heating value for hydrogen [LD00, BK06]. The net power of the fuel cell system P_{net} is defined as

$$P_{net} = P_{st} - P_{cm}, \tag{4.2}$$

where P_{st} denotes the gross power of the fuel cell stack and P_{cm} the blower motor power that is provided from the fuel cell and accounts for some of the parasitic losses. The variables are calculated as

$$P_{st} = v_{st}i_{st} \quad \text{and} \tag{4.3}$$
$$P_{cm} = v_{cm}i_{cm}, \tag{4.4}$$

where the fuel cell stack voltage v_{st} is calculated with Equation (3.1), i_{st} and v_{cm} denote the current stack and the blower input voltage, which represent the system inputs of the fuel cell system model. The variable i_{cm} denotes the blower motor current. The indicator of the net efficiency and the oxygen starvation is the excess oxygen ratio λ_{O_2}, which is defined by

$$\lambda_{O_2} = \frac{W_{O_2,in}}{W_{O_2,reacted}}, \tag{4.5}$$

with $W_{O_2,in}$ denoting the mass flow rate of oxygen gas entering the cathode and $W_{O_2,reacted}$ representing the rate of reacted oxygen. For different fuel cell current loads, the relationship between the excess oxygen ratio λ_{O_2} and the fuel cell net efficiency η_{net} is depicted in Figure 4.1. As value for all currents, the optimal value is chosen as $\lambda_{O_2,opt} = 2$, as marked in Figure 4.1, which is assumed as an averaged maximum.

The mass flow rate of reacted oxygen $W_{O_2,reacted}$ is defined by

$$W_{O_2,reacted} = \frac{M_{O_2}n_{fc}i_{st}}{4F}, \tag{4.6}$$

with M_{O_2} as the molar mass of the oxygen, n_{fc} as the number of cells, and F as Faraday number. From Equation (4.6), it becomes obvious that for a certain fuel cell system the mass flow rate of reacted oxygen only depends on the fuel cell current. Therefore the variable $W_{O_2,reacted}$ can not be influenced by controlling the
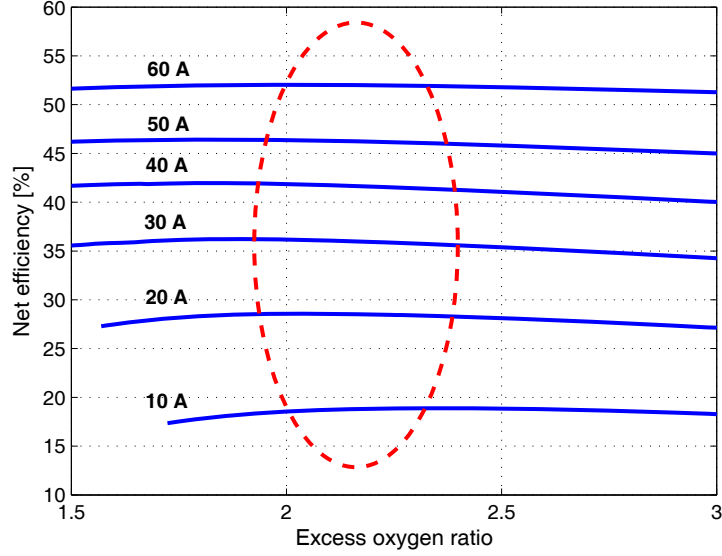
Figure 4.1: An optimal efficiency is achieved through different lambda values which can be controlled with the air-blower. Here, it is depicted for different current steps.

fuel cell system. If the mass flow rate of oxygen gas entering the cathode $W_{O_2,in}$ during the increasing current draw is constant, the excess oxygen ratio λ_{O_2} decreases accordingly. As a consequence, the net efficiency of fuel cell η_{Net} decreases and oxygen starvation is imminent. In order to keep the excess oxygen ratio λ_{O_2} at an optimal value, the mass air flow rate must be controlled. Inserting Equation (4.2), (4.5), and (4.6) in (4.1) the efficiency η_{net} is given as

$$\eta_{net} = \frac{v_{st}4FW_{O_2,in} - \lambda_{O_2}v_{cm}i_{cm}M_{O_2}n_{fc}}{W_{H_2,reacted}\Delta H_{h,H_2}\lambda_{O_2}M_{O_2}n_{fc}}, \tag{4.7}$$

which is plotted in Figure 4.1 as a function of λ_{O_2} for different stack load currents i_{st}.

4.2.2 Static Feed-Forward control

A classical way to control a fuel cell system is using an open-loop feed-forward control approach [PSP04]. This method only requires measurement of the current load of the fuel cell system, the knowledge of the system behavior (if the control input is previously calculated or optimized), and is easy to implement. The input signal to the system, i.e. the input voltage to the blower motor v_{cm}, can be represented with a look-up table, based on the data as given in Figure 4.1. As result, the input voltage of the electro-motor drives the blower at its optimal working point for each

current load i_{st} of the fuel cell system. The implementation of the look-up table in the feed-forward concept is depicted in Figure 4.2.
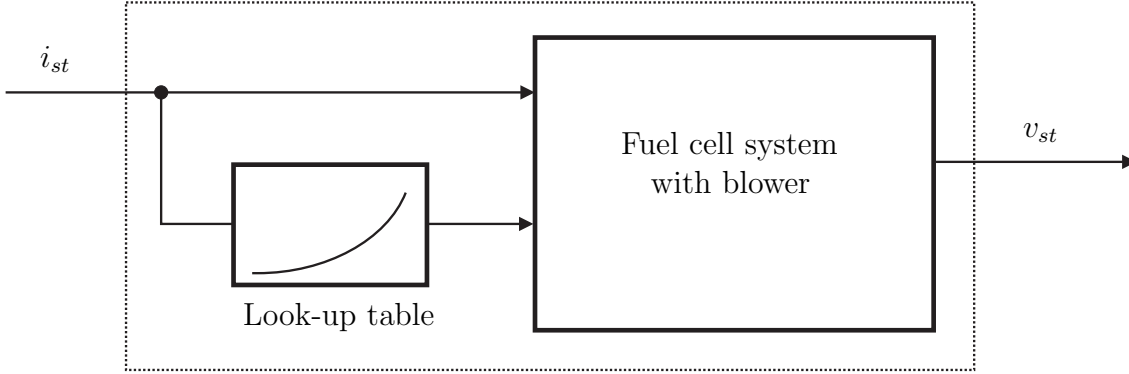

Figure 4.2: Control schedule of the static feed-forward controller implemented as a look-up table with the fuel cell current load i_{st} as input and the stack voltage v_{st} as output

4.2.3 Linearization of the fuel cell model

For analytical examination, analysis of a fuel cell system, and for design of a suitable controller, it is helpful to linearize the nonlinear model. In general, linearization of a nonlinear system makes it possible to apply conventional and powerful analyzing techniques such as stability, observability, and controllability examinations. A general explicit nonlinear system model can be presented in the following form

$$\dot{x}(t) = f(x(t), u(t)), \quad x(0) = x_0 \tag{4.8}$$
$$y(t) = g(x(t), u(t)). \tag{4.9}$$

If the system model with Equation (4.8) and (4.9) is linearized at the operating point (x_{op}, u_{op}, y_{op}), the system state model can be written as

$$\delta\dot{x}(t) = \frac{\partial f(x(t), u(t))}{\partial x}\Big|_{op}\delta x(t) + \frac{\partial f(x(t), u(t))}{\partial u}\Big|_{op}\delta u(t), \tag{4.10}$$

$$\delta y(t) = \frac{\partial g(x(t), u(t))}{\partial x}\Big|_{op}\delta x(t) + \frac{\partial g(x(t), u(t))}{\partial u}\Big|_{op}\delta u(t), \tag{4.11}$$

where the new linear state vectors δx, the input vector δu, and the output vector δy are defined as

$$\delta x(t) = x(t) - x_{op}, \tag{4.12}$$
$$\delta u(t) = u(t) - u_{op}, \text{ and} \tag{4.13}$$
$$\delta y(t) = y(t) - y_{op}. \tag{4.14}$$

The linearized system model is written in the state-space form as

$$\delta\dot{x}(t) = A\delta x(t) + B\delta u(t), \quad \delta x_0 = \delta x(0) \tag{4.15}$$
$$\delta y(t) = C\delta x(t) + D\delta u(t), \tag{4.16}$$

where A denotes the system matrix, B the input matrix, C the output matrix, and D the direct feed-through matrix. The current input i_{st} of the fuel cell system, which ranges between 0 and 60 A. The linearization point is chosen at 30 A. The voltage input to the blower motor is set accordingly and the stationary values of the states that follow are defined as initial condition values. The system variables are

$$x = \begin{bmatrix} m_{O_2} & m_{H_2} & m_{N_2} & m_{w,ca} & m_{w,an} & \omega_{cp} & p_{sm} & m_{sm} & p_{rm} & i_{cm} \end{bmatrix}^T,$$
$$u = v_{cm}$$
$$w = i_{st}$$
$$y = \begin{bmatrix} v_{st} & W_{cp,out} & p_{sm} \end{bmatrix}^T, \tag{4.17}$$
$$z = \begin{bmatrix} \eta_{net} & \lambda_{O_2} \end{bmatrix}^T, \tag{4.18}$$

with x as the state vector, u the input vector, w the disturbance vector, y the output vector, and z is introduced as a complementary output vector. The system is described by 10 state variables, 1 input variable, 1 disturbance variable, and 5 output variables including the performance variables η_{net} and λ_{O_2}.

4.2.4 Optimal control

A Linear Quadratic Regulator (LQR) optimal control is applied to design a state-feedback controller. As introduced in the previous sections, the target of the control is to minimize the response of the excess oxygen ratio λ_{O_2} from its reference. In the linearized model, this variable is denoted by δz_2. The LQR-related cost function J is defined by

$$J = \int_0^\infty \left(\delta z_2^T Q_z \delta z_2 + \delta u^T R \delta u \right) dt, \tag{4.19}$$

using the weighting matrices Q_z and R of the performance variable δz_2 and the input δu respectively. In order to follow the desired value of the excess oxygen ratio λ_{O_2}, an additional state q is defined. A direct relation between the desired performance variable $\lambda_{O_2,d}$ and the desired mass flow rate across the blower $W_{cp,d}$ is defined by [PSP04]

$$W_{cp,d} = \left(1 + \frac{M_v}{M_a} \frac{p_{sat}(T_{cp,in})}{p_{cp,in} - p_{sat}(T_{cp,in})} \right) \frac{M_{O_2} n}{x_{O_2} 4F} i_{st} \lambda_{O_2,d}, \tag{4.20}$$

with M_v, M_a, and M_{O_2} as the molar masses of vapor, dry air, and oxygen respectively, $p_{sat}(T_{cp,in})$ denotes the vapor saturation pressure at temperature $T_{cp,in}$, and x_{O_2} denotes the oxygen mass fraction in dry air. Using this desired value, an additional state q is defined by

$$\dot{q} = W_{cp,d} - W_{cp,out} = W_{cp,d} - C_{y2}\delta x, \tag{4.21}$$

where the mass flow rate across the blower $W_{cp,out}$ in case of a real application can be measured easily. Using the LQR approach design, in order to minimize the additional state q, the cost function J has to be transformed to

$$J = \int_0^\infty \left(\delta z_2^T Q_z \delta z_2 + q^T Q_q q + \delta u^T R \delta u \right) dt \tag{4.22}$$

with the weighting function Q_q for the state q. Because

$$\delta z_2 = C_{z_2}\delta x, \tag{4.23}$$

the cost function becomes

$$J = \int_0^\infty \left(\delta \hat{x}^T \hat{Q} \delta \hat{x} + \delta u^T R \delta u \right) dt, \tag{4.24}$$

where the weighting matrix $\hat{Q}$ is defined as

$$\hat{Q} = \begin{bmatrix} C_{z_2}^T Q_z C_{z_2} & 0 \\ 0 & Q_q \end{bmatrix} \tag{4.25}$$

and the new state vector $\hat{x}$ is defined as

$$\hat{x} = \begin{bmatrix} \delta x \\ q \end{bmatrix}. \tag{4.26}$$

According to the principle of the LQR optimal controller, the control input is

$$\delta u = -K_{opt}\delta \hat{x}, \tag{4.27}$$

with K_{opt} as the controller gain matrix calculated from

$$K_{opt} = R^{-1}\hat{B}_u P, \tag{4.28}$$

where $\hat{B}_u$ denotes the input matrix of the system describing the additional state q and P denotes the solution matrix to the algebraic Riccati equation. The state-space model of the system with the additional state q is then given as

$$\delta \dot{\hat{x}} = \hat{A}\delta \hat{x} + \hat{B}_u \delta u + \hat{B}_w \delta w \tag{4.29}$$

with the matrices

$$\hat{A} = \begin{bmatrix} A & 0 \\ A_q & 0 \end{bmatrix}, \quad \hat{B}_u = \begin{bmatrix} B_u \\ 0 \end{bmatrix}, \quad \hat{B}_w = \begin{bmatrix} B_w \\ B_q \end{bmatrix}. \tag{4.30}$$

Here, the matrix A_q can be calculated according to Equation (4.21) by

$$A_q = -C_{y_2}. \tag{4.31}$$

The matrix B_q can be calculated according to Equation (4.20) by

$$B_q = \left(1 + \frac{M_v}{M_a} \frac{p_{sat}(T_{cp,in})}{p_{cp,in} - p_{sat}(T_{cp,in})}\right) \frac{M_{O_2}n}{x_{O_2}4F} \lambda_{O_2,d}. \tag{4.32}$$

Due to the structure of A_q (singular eigenvalues) controllability has to be assumed for successful realization.

4.2.5 Gain-scheduling control

Since fuel cells are strongly nonlinear over their entire area of working field, it can be desired to examine the possibility of implementing nonlinear control approaches. For the state-feedback method, the system is linearized in a single working point and the linear controller is then applied at the whole working range. For strongly nonlinear systems, like fuel cells, this can be insufficient from a performance point of view as will be seen in the results presented here, but also with respect to stability. With gain-scheduling control, it is possible to linearize the system in several nominal points and introduce a controller for each point. Thereafter, the different controllers are interpolated between each other and implemented on the fuel cell system on the whole working range. The linearization points for the gain-scheduling controller are for this fuel cell system chosen to $i_{st} = 10, 20, 30, 40, 50$, and $60\,\text{A}$. This multi-model approach does not guarantee stability. If stability of the approach has been proven experimentally, this is easy to realize and can be used to tune the controlled system behavior. A strategy to check stability of such systems is given by [ASS07]. This covers the whole working range of the fuel cells and the distance between the linearization points is close enough to give satisfying results. The gain-scheduled linearized system model is represented in the following state-space form

$$\delta\dot{x}(t) = A_i\delta x(t) + B_i\delta u(t), \quad \delta x_0 = \delta x(0) \tag{4.33}$$
$$\delta y(t) = C_i\delta x(t) + D_i\delta u(t). \tag{4.34}$$

Optimal controller gains are calculated for each working point $K_{opt,i}$ according to Equation (4.28). In Figure 4.3, the interpolation between the matrix-elements of the gain-scheduled optimal controller matrix $K_{opt,i}$ is depicted. As it can be seen, the elements are smoothly changing their values between the linearization points. This makes the gain-scheduling controller possible to implement and at the same time allowing a fast and smooth switching between the linearization points.
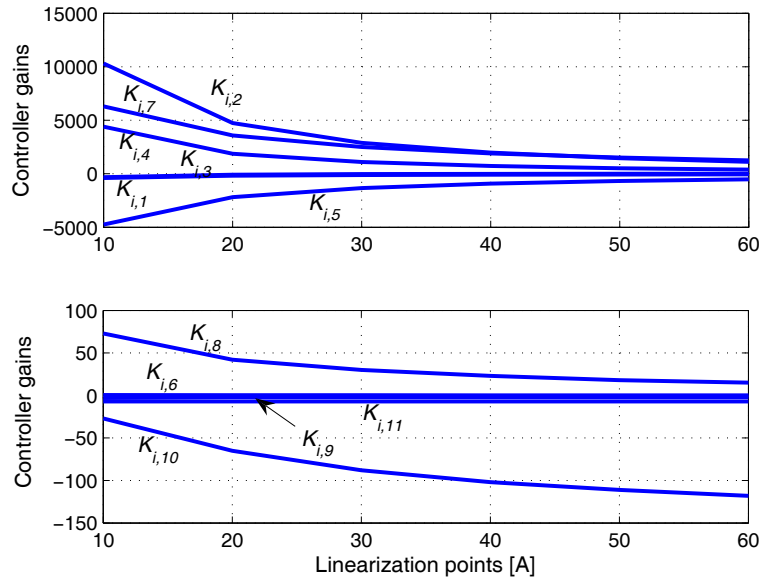
Figure 4.3: The gain-scheduling controller is interpolated between the linearization working points. Top: Large value gains. Bottom: Small value gains

4.2.6 Hydrogen valve control

The hydrogen of the considered system supplied from a high-pressure tank comes with a flow rate controlled by a valve. This gives a relatively rapid adjustment of the flow rate and anode pressure. The control variable is the anode pressure and as reference value the cathode pressure is used. This means, the control goal is to minimize the pressure difference between anode and cathode, therefore a PI-controller is used. Since the output control value is the anode pressure, p_{an} and the input variable is the anode inlet flow $W_{an,in}$ the equation (without interfering from any disturbances) is given by

$$p_{H_2} = \frac{R_{H_2} T_{fc}}{V_{an}} m_{H_2}, \tag{4.35}$$

here the hydrogen mass m_{H2} is calculated as the integral of the difference between injected and consumed hydrogen flows by

$$m_{H_2} = \int_0^t (W_{H_2,in} - W_{H_2,reacted}) dt. \tag{4.36}$$

The variable $W_{H2,reacted}$ is directly considered as a disturbance through the output current according to

$$W_{H_2,reacted} = M_{H_2} \frac{n i_{st}}{2F}. \tag{4.37}$$

The variable $W_{H2,an,in}$ is calculated from

$$W_{H_2,in} = \frac{W_{an,in}}{p_{v,an}M_{H_2} - p_{an}M_{H_2} + p_{v,an}M_v},\tag{4.38}$$

where $p_{v,an}$ denotes the partial pressure of vapor inside the anode. The variable is referred as the input signal to the hydrogen control system as shown in Figure 4.4.
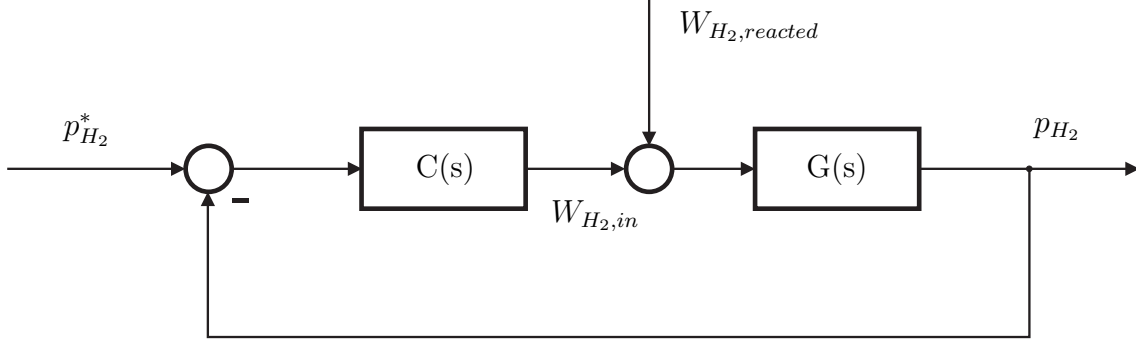

Figure 4.4: Control diagram of the hydrogen valve control

Calculating the transfer function from the consumed hydrogen $W_{H_2,reacted}$ due to a drawn current load gives

$$G_{p_{H_2},W_{H_2,reacted}} = -\frac{R_{H_2}T_{fc}}{s(V_{an} + V_{an}K)},\tag{4.39}$$

whereby the transfer function using a PI-controller with K as proportional gain and T_I as design parameter yields

$$P_{H_2}(s) = \frac{KR_{H_2}T_{fc}(s + T_I)}{Vs^2 + KRTs + KRTT_I}R(s) - \frac{sRT}{Vs^2 + KRTs + KRTT_I}W_{H_2,reacted}(s).\tag{4.40}$$

Examining the final values for $t \to \infty$ using the final-value-theorem, the final value of a given reference step gives

$$\lim_{s \to 0} -s\frac{1}{s}\frac{KR_{H_2}T_{fc}(s + T_I)}{Vs^2 + KRTs + KRTT_I} = 1.\tag{4.41}$$

For a disturbance step function the final value results to

$$\lim_{s \to 0} -s\frac{1}{s}\frac{sR_{H_2}T_{fc}}{Vs^2 + KRTs + KRTT_I} = 0\tag{4.42}$$

meaning any disturbances are rejected. Using only a P-controller as suggested in [PSP04] would give the transfer function

$$P_{H_2}(s) = \frac{K R_{H_2} T_{fc}}{V s + K R T} R(s) - \frac{R T}{V s + K R T} W_{H_2,reacted}(s).$$ (4.43)

Applying the final-value-theorem to examine the stationary values for an input step function for the reference signal gives

$$\lim_{s \to 0} s \frac{1}{s} \frac{K R_{H_2} T_{fc}}{V_{an} s + K R_{H_2} T_{fc}} = 1,$$ (4.44)

and for the disturbance

$$\lim_{s \to 0} -s \frac{1}{s} \frac{R_{H_2} T_{fc}}{V_{an} s + K R_{H_2} T_{fc}} = -\frac{1}{K},$$ (4.45)

So the disturbance can not be accommodated by P-Control. Due to the integral behavior of the system it is not recommended to use a P-controller, as in [PSP04] due to this stationary error from the disturbance. Instead, a PI-controller should be used in order to completely eliminate the stationary error as depicted in Figure 4.5. The transfer function from the reference value to the output is

$$G_{r,p_{H_2}}(s) = R_{H_2} T_{fc} K \frac{s + T_I}{V_{an} s^2 + R_{H_2} T_{fc} K s + R_{H_2} T_{fc} K T_I}.$$ (4.46)

Depending on the parameters this can lead to oscillations of the PDT$_2$-system. Using root-locus analysis, the integral coefficient T_I determines the bandwidth of the closed system. When that is made, the proportional coefficient K is chosen to avoid any kind of disturbances.

4.3   Results

The three control approaches are compared by simulations. All three include the presented hydrogen valve controller as introduced in Chapter 4.2.6. As input signal a series of current step functions ranging through the whole working field of the fuel cells as depicted in Figure 4.6 is chosen.

The results of the three control approaches are shown in Figure 4.7. As desired value of the excess oxygen ratio the value $\lambda_{O_2} = 2$ is chosen. The state-feedback controller gives a stationary error in working points different from the linearization point of $30\,\mathrm{A}$ (here realized at approx. $20\,\mathrm{s}$).

Zooming at a current step outside the linearization point, e.g. at $10\,\mathrm{s}$, the results are depicted in Figure 4.8. It is shown that the state-feedback and the gain-scheduling control methods are advantageous in relation to the static feed-forward method in
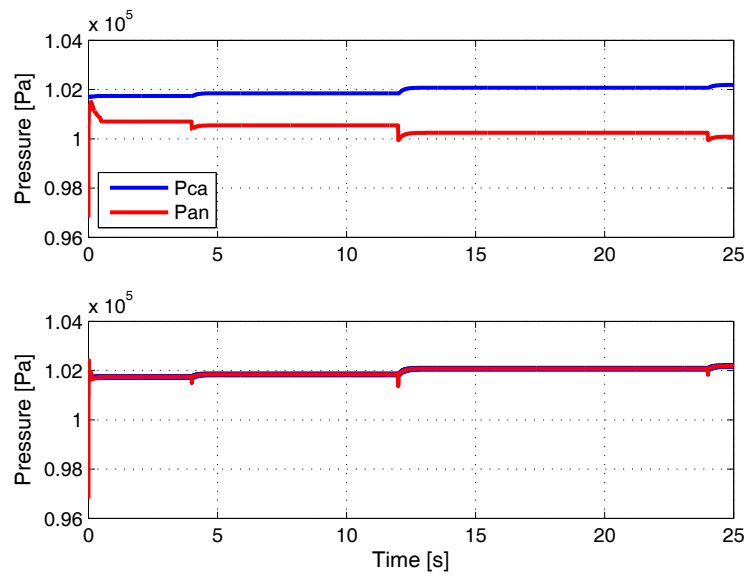
Figure 4.5: Cathode and anode pressures for a P- (top) respectively PI-controller (bottom) for the hydrogen valve
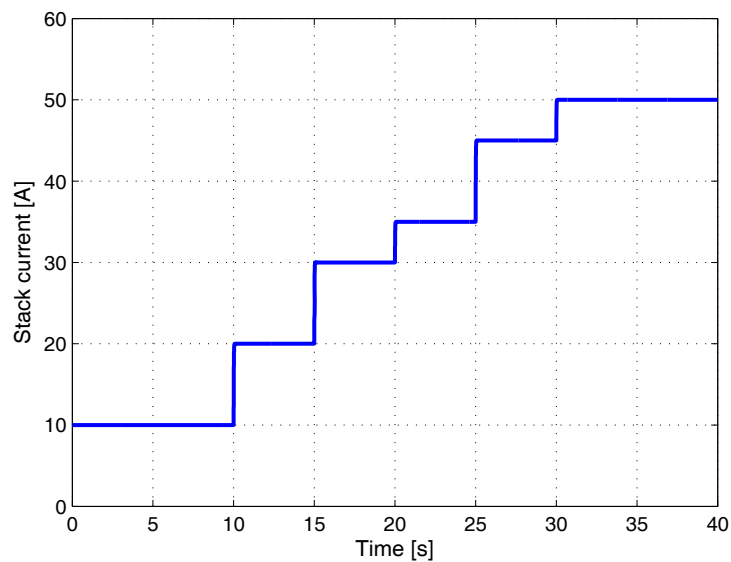

Figure 4.6: Input current variable used as input for comparing the control approaches
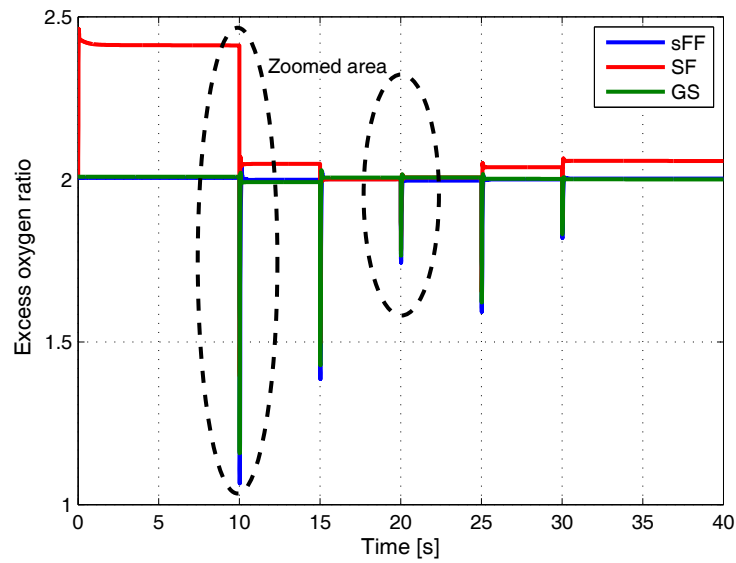
Figure 4.7: Comparison of the static feed-forward, state feedback, and gain-scheduling control applied for a nonlinear fuel cell model
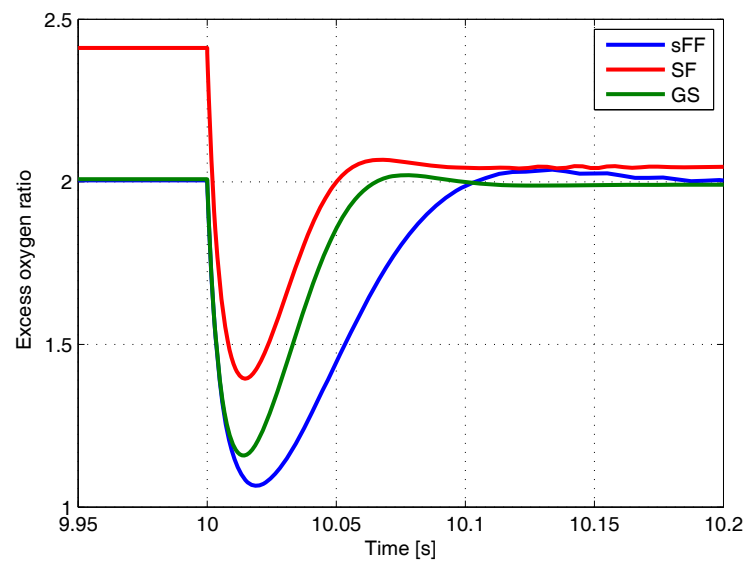

Figure 4.8: Zoomed area for a step current output at a working point outside the linearization nominal point

keeping the excess oxygen ratio at an optimal point and preventing oxygen starvation.

Zooming Figure 4.7 at the linearization point shows the depicted results in Figure 4.9. The state-feedback and gain-scheduling controllers show almost similar results while the static feed-forward controller shows slower response to recover the optimal value of the oxygen excess ratio.
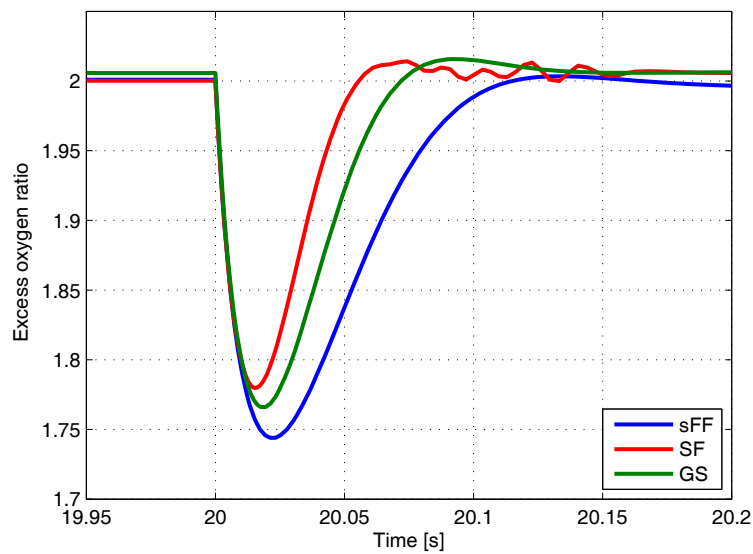
Figure 4.9: Zoomed area around the working linearization point for a step current output

4.4 Control of DC/DC-converter

Here, the control of a CUK DC/DC-converter model described in Chapter 3.4 and validated in Chapter 3.5.4 is developed. The CUK-converter is identical to a Buck-Boost converter with the difference that the output voltage is not inverted as in a Buck-Boost converter. Boost, Buck-Boost, or CUK-converters are usually more difficult to control than buck-converters. This is due to that the converters with boosting behavior are so called non-minimum phase systems [Ven86]. Therefore, a method called state-space averaging is applied.

State-space averaging (SSA) A method which deals with discrete switching inputs is state-space averaging [Eri99]. With this method, a state-space model is derived for every switching position and the models are averaged giving a low-frequency model that is possible to simulate continuously neglecting the switching states. This technique is favorable over sliding mode control in simulation environments due to faster simulations and is the method used here [OS08].

The state-space averaging method is used to linearize the system by describing all variables in DC and AC parts, e.g. $i_{L1} = I_{L1} + \tilde{i}_{L1}$, where capitol letter denotes the DC and tilde denotes the AC part. After substituting all variables the next step is to eliminate all DC and cross-products between DC and AC variables. For this method to be valid it is required that the variables in the two switching states behave linear and that the ripple due to switching is small in comparison with the average value [FM98]. Doing so gives a linear system and a linear controller can be applied on the DC/DC-converter.

For the inductance current

$$\frac{d\tilde{i}_{L_2}}{dt} + \frac{d\tilde{I}_{L_2}}{dt} = -\frac{U_{C_2} + \tilde{u}_{C_2}}{L_2} - \frac{(U_{C_1} + \tilde{u}_{C_1})(D + \tilde{d})}{L_2} - \frac{R_2(I_{L_2} + \tilde{i}_{L_2})}{L_2}. \tag{4.47}$$

Removing the pure DC and cross-products between the AC components gives

$$\frac{d\tilde{i}_{L_2}}{dt} = -\frac{1}{L_2}\tilde{u}_{C_2} - \frac{R_2}{L_2}\tilde{i}_{L_2} - \frac{D}{L_2}\tilde{u}_{C_1} - \frac{U_{C_1}}{L_2}\tilde{d}. \tag{4.48}$$

Equivalently, for the other states gives

$$\frac{d\tilde{u}_{C_2}}{dt} = \frac{\tilde{i}_o}{C_2} + \frac{\tilde{i}_{L_2}}{C_2} \tag{4.49}$$

$$\frac{d\tilde{i}_{L_1}}{dt} = -\frac{D}{L_1}\tilde{u}_{C_1} - \frac{R_1}{L_1}\tilde{i}_{L_1} + \frac{U_{C_1}}{L_1}\tilde{d} + \frac{1}{L_1}\tilde{u}_{in} \tag{4.50}$$

$$\frac{d\tilde{u}_{C_1}}{dt} = \frac{D - 1}{C_1}\tilde{i}_{L_1} + \frac{D}{C_1}\tilde{i}_{L_2} + \frac{I_{L_2} - I_{L_1}}{C_1}\tilde{d}. \tag{4.51}$$

The converter model

$$
\dot{x} =
\begin{bmatrix}
0 & 0 & \frac{1}{C_2} & 0 \\
0 & -\frac{R_1}{L_1} & 0 & -\frac{0.5}{L_1} \\
-\frac{1}{L_2} & 0 & -\frac{R_2}{L_2} & -\frac{D}{L_2} \\
0 & \frac{0.5}{C_1} & \frac{0.5}{C_1} & 0
\end{bmatrix}
\begin{bmatrix}
\tilde{u}_{C_2} \\
\tilde{i}_{L_1} \\
\tilde{i}_{L_2} \\
\tilde{u}_{C_1}
\end{bmatrix}
+
\begin{bmatrix}
0 \\
\frac{100}{L_1} \\
\frac{100}{L_2} \\
0
\end{bmatrix}
\tilde{d}
\tag{4.52}
$$

$$
y =
\begin{bmatrix} 1 & 0 & 0 & 0 \end{bmatrix}
\begin{bmatrix}
\tilde{u}_{C_2} \\
\tilde{i}_{L_1} \\
\tilde{i}_{L_2} \\
\tilde{u}_{C_1}
\end{bmatrix}
\tag{4.53}
$$

is linearized at a working point of an output voltage at $50\,\mathrm{V}$ and at no load current $i_o = 0$ and no supply voltage $u_{in} = 0$. The duty ratio is chosen as the middle value of $D = 0.5$.

The system is now linearized with the duty ratio $\tilde{d}$ as input. Note that only one output $\tilde{u}_{C_2}$ is regarded and the system is yet fully observable, which allows the feedback of all states and hence a state-feedback controller is used here. The controller is developed with the LQR-approach as introduced in Chapter 4.2. The weighting matrices are designed in order to fulfill a satisfying trajectory of the reference signal and to give a satisfying validation as shown in Chapter 3.5.4.

The control of the DC-motor which is modeled in Chapter 3.1.2 is realized with the same CUK-converter described here. The output voltage from the DC/DC-converter rotates the motor and the required current is fed back to the converter model as an external disturbance.

The results of the controllers are given together with the validation results of the corresponding components in Chapter 3.

5 Parametrization and evaluation

In this chapter, the sizing of the components from a given load profile will be presented and different hybrid concepts and therefore topologies will be simulated and additionally realized in the HiL-powertrain for evaluation. The goal is to downsize the fuel cells as much as possible and at the same time make sure that the dynamics requirement of the load profile can be realized. In case of an unknown load profile, the system can also be designed from empirical data or assumptions [LD00]. However, this is not regarded here, because the load profile is assumed to be known.

In [SDA09], a stand alone fuel cell hybrid system for supplying remotely located telecommunication stations without connection to the electrical grid was designed and built up. Here, the load profile was supposedly known. The load profile had few power peaks (about 6 times larger than the continuous power output) and contained no recuperation phases. Even though the fuel cell system had smaller rated power than the maximum power peaks of the load profile, i.e. the fuel cell was down-sized, there were possibilities to further down-size the fuel cell system. The reason why it was not done is that the authors restricted the choice of system components to commercially available products.

In [KSLK08], a fuzzy logic controller was used on the system as controller for the powermanagement and the sizing was made iteratively with simulation models afterwards. Also here, the load profile was supposed to be known. The criteria to be optimized was the overall system efficiency. Even though this is a good approach while the size of the fuel cells is decreased, it is optimal only for the given powermanagement. The reason is that the powermanagement is determined before the sizing of the components. Developing the powermanagement after the sizing is calculated should be advantageous due to the parameter knowledge of the system components and hence gives the ability to optimize the powermanagement controller. Other publications on sizing of a hybrid system can be found in [KML+05, Hen08, KP07, CBF08, ERWL05].

5.1 System design from given load profiles

The design scheme for sizing a hybrid powertrain is as follows:

- Calculation of the power flow to/from the electro-motor (in case of a driving cycle for vehicle application),

- Definition of a load profile (or calculation from driving cycle),

- Calculation of the size of the fuel cells,

- Definition of the bus voltage interval,

- Calculation of the size of the accumulator (batteries or SuperCaps),

- Definition of the most suitable topology for the load profile, and

- Specification of a powermanagement algorithm with fuel consumption, dynamics requirement, or component lifetime in consideration.

The main benefits form hybridizing a system is to save costs through down-sizing, fuel saving, and lifetime extension of the components. Especially, when it comes to fuel cells, the largest costs are not fuel but the purchasing costs. The advantages of hybridizing a fuel cell system are:

- Downscaling of the fuel cells,

- Increasing of the system dynamics,

- Increasing the system efficiency,

- Harvesting of braking energy, and

- Increasing the lifetime of system components.

For unpredictable load profiles, the only way to guarantee that the required power will always be delivered is to abandon the hybrid concept and equalize the fuel cell output power with the systems maximum power. Of course, this would considerably increase the purchasing costs, deteriorate the fuel cell lifetime, and increase the fuel consumption. Since fuel cells have relatively slow dynamics, it would not be possible to realize highly dynamical load profiles solely with fuel cells. The given load profile, as repeatedly depicted in Figure 5.1, is measured from an industrial fork lift and normalized to suit the 2 kW hybrid system demands developed here.

5.1.1   Degree-of-Hybridization (DoH)

The Degree-of-Hybridization (DoH) is defined as the ratio between the maximum power the fuel cells can deliver with the maximum power of the system (load profile). Since the accumulator is mainly used for delivering the peak power, it is necessary to define a continuous power that the hybrid system can run infinitely (as long as fuel is provided). This parameter is probably the most important to the system behavior. As simulations will show, a large DoH would mean shorter deliverance time of peak power and hence could mean the power load profile not being realized.

The fuel cells shall be sized to the average of the load profile power as depicted in Figure 5.1. Subtracting the average value from the load profile gives the power flow
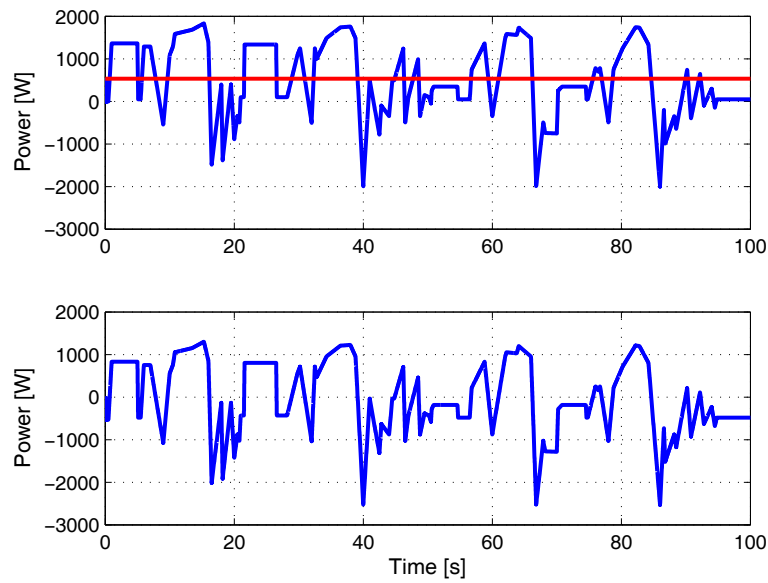
Figure 5.1: Given load profile with the mean value of 531.5 W for the fuel cells and the power flow for SuperCaps. Above plot - Load profile with calculated fuel cell power, bottom plot - calculated SuperCap power flow.
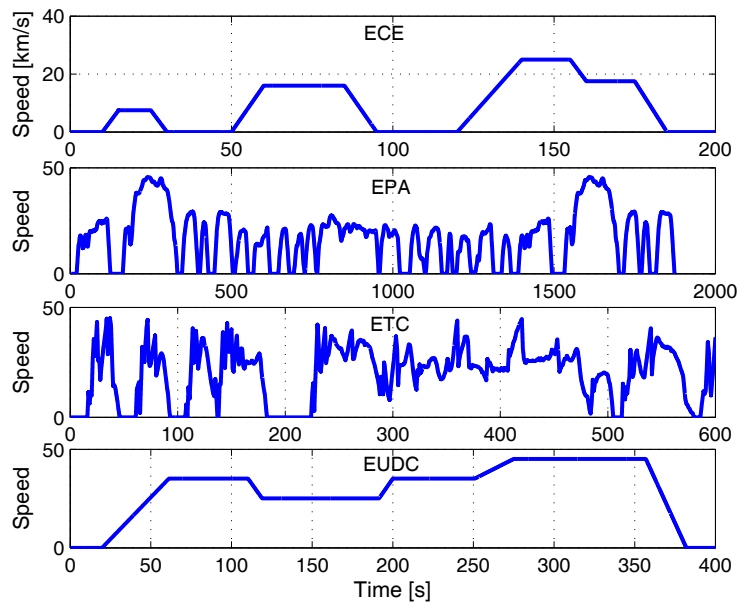

Figure 5.2: Simulated driving cycles normalized for a smaller vehicle

to and from the accumulator as shown in the lower plot of Figure 5.1. The charge of
the accumulator should cover all the peak demands of the load profile. This means,
for each charging moment coming either from the fuel cells or from regenerative
braking, the accumulator should be charged to guarantee enough energy for the
next power peak demand. The results indicate a recommended value of 531.5 W for
the fuel cells, which gives a DoH of 0.265, i.e. 26.5% of the maximum power comes
from the fuel cells and the remaining (peak) from the accumulator.

This is repeated for a vehicle scooter as simulated system whereas the speed profile
is given and the corresponding power is calculated from simulations. Thereafter the
DoH is calculated and the results are shown in the tabular below.

Cycle	Mean [W]	Max [W]	DoH (for 2 kW system)
EUDC	279.5	1 303	0.215 (0.140)
ECE	100.5	918.7	0.109 (0.050)
EPA	217.5	1 470.3	0.148 (0.109)
ETC	290.9	2 258.8	0.128 (0.145)

As it can be seen from the values above, the industrial application requires larger
fuel cells than the vehicle application which ought to have fuel cells in sizes between
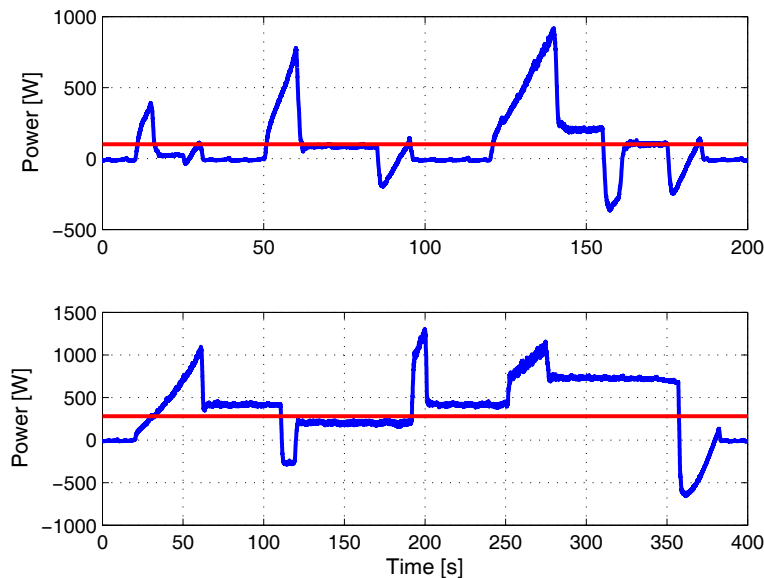100 and 290 W.

Figure 5.3: Simulated power flow for the suburban driving cycles ECE and EUDC
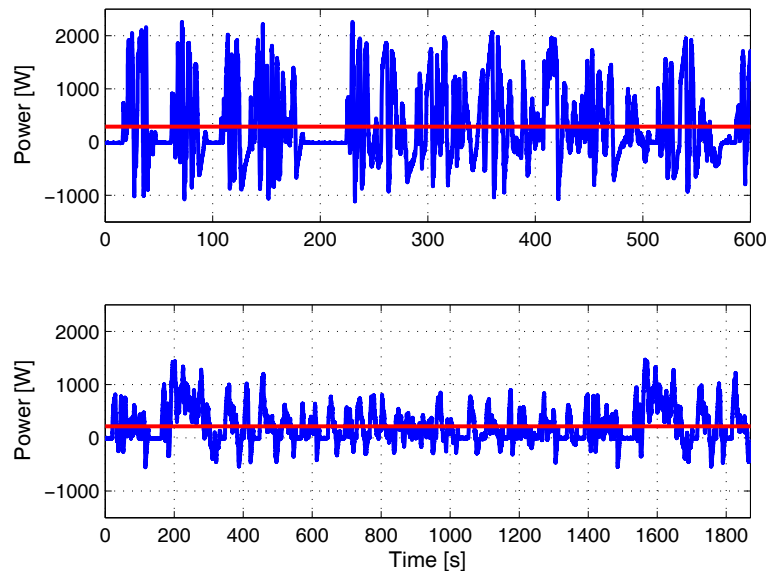and their corresponding averaged power [red]

Figure 5.4: Simulated power flow for the urban driving cycles ETC and EPA and their corresponding averaged power [red]

5.1.2   Batteries or SuperCaps

As mentioned in Chapter 2 the SuperCaps have a superior power density over batteries whereas batteries have higher energy density. Fuel cells have even higher energy density than batteries but lower power density than SuperCaps and batteries. Since the accumulator in a hybrid system is used for delivering fast power peaks, it shall be chosen depending on the power density of the load profile. To demonstrate this, lead-batteries are implemented in the HiL-powertrain instead of SuperCaps and tested for the given load profile. The batteries are connected in series to have a rated bus voltage of 36 V (meaning 3 in series coupled batteries). Lead-batteries are often used in industrial systems due to their low costs and hence are being compared to in this application. The results are shown in Figure 5.5. It is noted that the bus voltage varies more than with SuperCaps and the reason is the limited load current capability of the lead-batteries. The red lines show the maximum and minimum allowed voltage for three in series coupled lead-batteries and the bus voltage exceeds even the maximum allowed voltage. The conclusion is that lead-batteries are not suitable for this load profile since it is to dynamic.
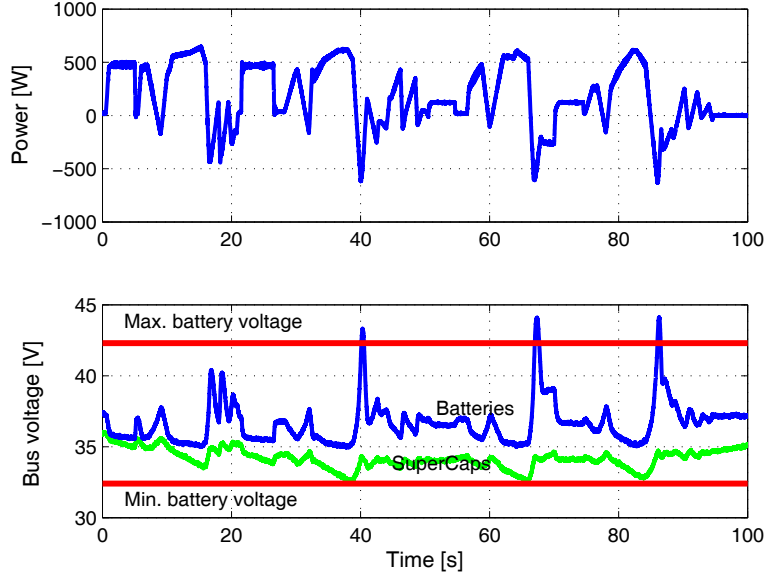
Figure 5.5: Comparison between SuperCaps and lead-batteries realizing the highly dynamical load profile. As can be seen in the bottom plot, even a down-scaling of the load profile is too dynamical for the batteries.

5.1.3 Sizing the SuperCaps of the hybrid system

To simplify the illustration of the load profile, the time stamps of the power profile hitting the zero level are noted and the energy content of each positive and negative peak is calculated and plotted as quantized values, as can be seen in Figure 5.6. The energy change is plotted in Figure 5.7 and has a difference of 14754 J which corresponds to (for the case of 18 SuperCaps in row)

$$C_{sc} = \frac{2E_{sc}}{U_{sc}^2} = \frac{2 * 14754}{48.6^2} \approx 12.5\,\text{F}, \tag{5.1}$$

which gives for 18 SuperCaps in row 225 F per SuperCap. After defining the maximum and minimum voltages the capacitance of the conductors for the given load profile can be calculated from

$$E_{sc} = \frac{C(U_{max} - U_{min})^2}{2}. \tag{5.2}$$

Constraints to accumulator voltage

As can be seen from the load profile, it starts directly with a small recuperation phase. It is hence not possible to start with a fully charged accumulator, due to
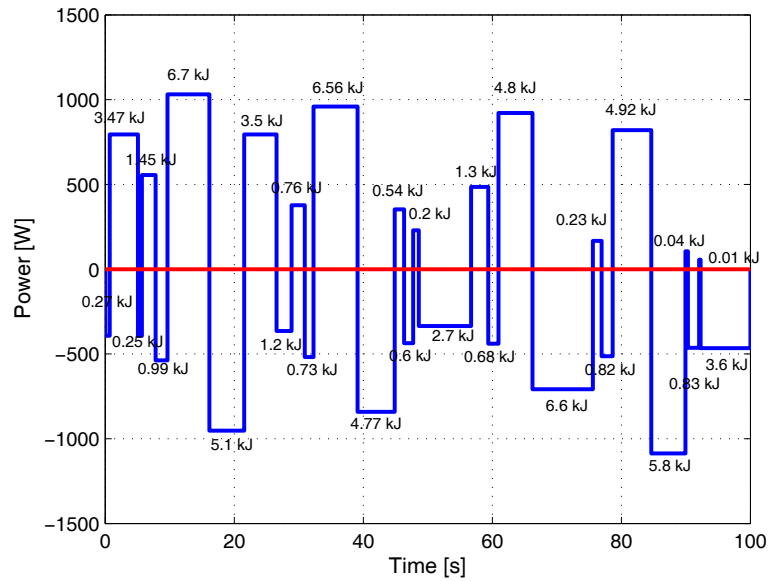
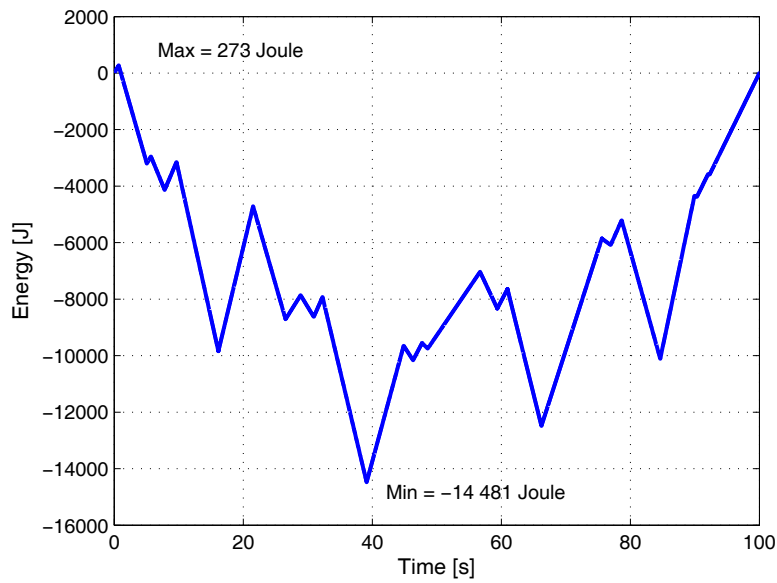Figure 5.6: Discretized accumulator power flow with the energy content of each power peak

Figure 5.7: Energy content change of the load profile for the hybrid system

risk for over charging. The initial charge is determined by integrating the load
profile with time and determine the maximum and minimum energy content values
depicted in Figure 5.7 which correspond to the maximum and minimum voltage and
it is calculated to 1-273/(273-(-14 480)) = 0.9818, i.e. initial SoC = 98.18%.

From sizing the SuperCaps it is possible to determine the lowest and highest accept-
able voltage for the given load profile. By inserting in Equation (5.2) the highest
and lowest voltage (48.6 V resp. 30 V) the capacity is calculated for the given load
profile to

$$C_{sc} = \frac{2E_{sc}}{(V_{max} - V_{min})^2} = \frac{2 * 14754^2}{48.6 - 30} = 85.3\,\text{F} \tag{5.3}$$

corresponding to 1535.3 F for each cell.

Since the load profile is assumed as a power flow, which is the product between
current and voltage (or speed and torque), it does not directly determine the current
and voltage values. However, since many components and cables develop heat with
increased currents, there are limitations how much current can flow in a hybrid
system. Therefore, the maximum current should first be determined and then the
voltage level. From market product availability and specifications, the maximum
current for a 2 kW system ought to be about 50 A and have a voltage level between
30 and 48 V. The maximum voltage here shall not, unless necessary, exceed 50 V for
safety reasons.

5.1.4 Simulation results

Based on the calculations given above, the parametrization is implemented in the
scalable models presented in Chapter 3 and simulated. The SuperCaps are connected
in series and are 18 to the amount with 1535.3 F in capacitance per cell. The fuel cell
power is scaled to 531.5 W. The DC/DC-converter parameters are not changed due
to the already fast dynamics in comparison to the other system components but yet
not modeled statically to avoid algebraic loops. The simulation results are depicted
in Figure 5.8. The above plot shows the power flows of the SuperCaps and fuel cells
and the middle plot shows the variation of the bus voltage. The reference bus voltage
value is here set to 50 V and the actual bus voltage equals the output voltage of the
SuperCaps since they are directly connected to the bus (topology range extender).
The SoC of the SuperCaps is depicted in the bottom figure. The initial charge was
calculated above and the final charge is slightly less than predicted. This is due
to resistance losses in the DC/DC-converter as well as in the SuperCaps which are
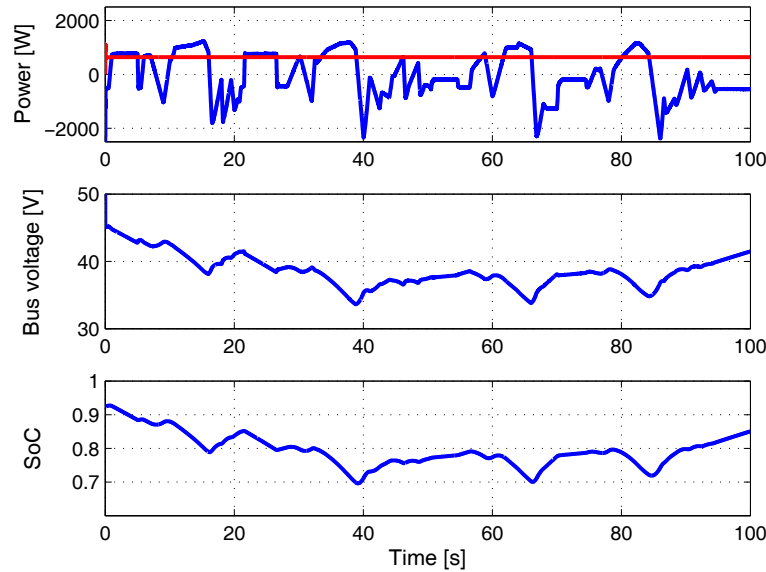neglected in the above calculations of the component sizing for a given load profile.

Figure 5.8: Simulation results of the parameterized components. Above plot shows SuperCap power in blue and fuel cell power in red, middle plot shows the bus voltage and bottom plot shows the SuperCaps SoC.

5.2 Choice of topology

Several different topologies for fuel cell hybrid systems are already outlined and tested in a simulation environment for different driving cycles in [NPA06]. A relevant task is to find an optimal topology for driving cycles. As conclusion in [NPA06] it is suggested that some topologies are better suited for high performance driving cycles while other topologies are better suited for long-range driving cycles. The reason is stated, that each topology configuration has different system efficiency and power ability. Hence, there is no optimal topology for all types of driving cycles. In this work, four topologies are presented and discussed; a basic topology without DC/DC-converters, the range extender topology, the full hybrid topology, and the extended hybrid topology with two DC/DC-converters. The choice of topology depends mainly on what the user prioritizes. It may either be fuel consumption, range, dynamics, or lifetime. Two of the topologies are realized in the HiL-powertrain and simulated for the given load profile and evaluated.

5.2.1 Topology A: Basic topology

A basic hybrid concept is when no DC/DC-converters are involved and the power sources are directly connected to the system bus as depicted in Figure 5.9. However,

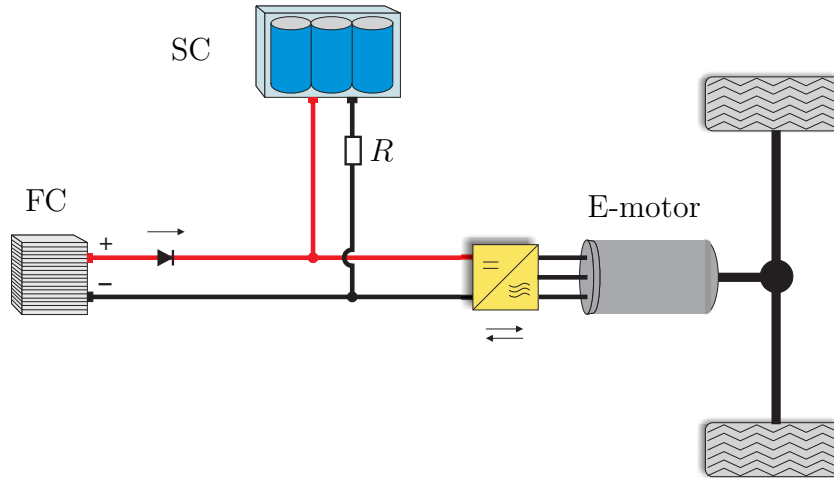a DC/AC-converter must be implemented for motor control.

Figure 5.9: Topology A: Basic topology for a hybrid system where no DC/DC-converters are used

Initially, if the SuperCaps have lower voltage than the fuel cell voltage, the fuel cells will be short cut and permanently damaged. To avoid a short cut, it is necessary to implement a resistor in series with the accumulator shown as R in Figure 5.9. Of course, this means that much power will be dissipated in heat and hence decrease the system efficiency considerably. At operating conditions, the fuel cell will fill the accumulator until the same equilibrium voltage level is reached in the system bus and between the energy sources. The resistance can be minimized and the SuperCaps would then be regarded as a high pass filter for the fuel cell power output. It should be noted that, even if equilibrium is reached for the bus voltage, it is still possible to charge the SuperCaps to a voltage higher than provided from the fuel cells. This requires of course a diode for the fuel cells to protect them from regenerative current. Due to that the fuel cell system supplies an unregulated power it is necessary to connect a DC/DC-converter when it is connected to a DC-load which works at constant supply voltage. This is the case for most electric drives. The main disadvantage of this topology is the inability of controlling the bus voltage and the large resistance losses, and hence not regarded as competitive to the other topologies.

5.2.2   Topology B: Range extender

The range extender has its name due to the idea behind that the vehicle is powered from an accumulator and in order to extend the distance of the vehicle (due to poor energy density of the accumulator) a secondary energy unit (with high energy

density) is implemented to charge the accumulator. The topology configuration is depicted in Figure 5.10.
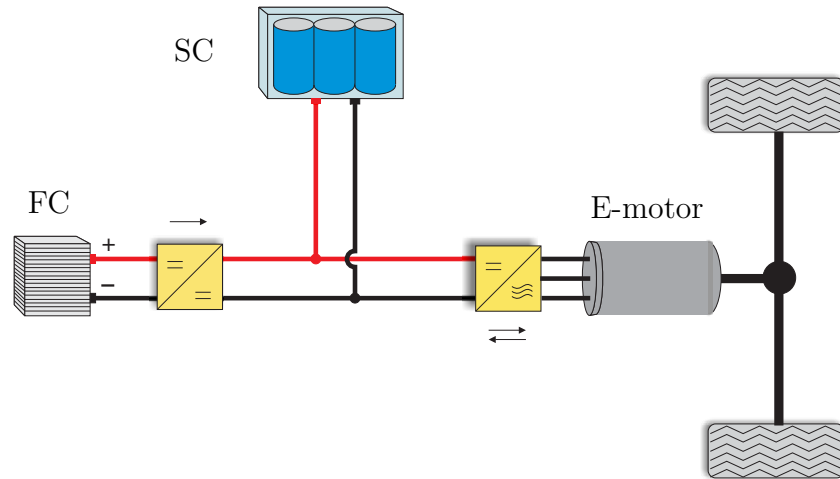

Figure 5.10: Topology B: Range extender topology with a fuel cell mono-directional DC/DC-converter

There are several ways how to charge the SuperCaps, defined in the powermanagement strategies discussed in Chapter 6. Dependent on the size of the fuel cells and on the powermanagement, constant output fuel cell power can be realized. The HiL-simulation results, after sizing the fuel cells to the averaged load profile are depicted in Figure 5.11 and show the continuous power output behavior of the fuel cells.

In this topology, the bus voltage equals the output voltage of the SuperCaps and varies correspondingly. Over-sizing the fuel cells would fill the SuperCaps faster but also saturate them during the load profile and hence the power output of the fuel cells would alternate accordingly. For lifetime considerations of the fuel cells and due to a variety of the working range (in less efficient working points), this should be avoided. Summarizing the advantages and disadvantages of this topology, the main benefits are that the fuel cells can, by the ability of continuous operation, work constantly at their maximum efficiency point and their lifetime at the same time can be enhanced. Further on, the usage of only one DC/DC-converter (instead of two) decreases the overall losses and due to the continuous working point of the fuel cells, the DC/DC-converter can be configured accordingly. The drawbacks are that the bus voltage is equivalent to the SuperCap voltage and cannot be controlled with useful dynamics. One must charge the SuperCaps up till the referenced voltage and this could take considerable time before the desired voltage is achieved. This includes, that the supply voltage to the electro-motor will vary slowly leading to the risk that the maximum dynamics cannot be achieved for unpredictable load profiles. The main disadvantage of inserting a buck-boost converter to the fuel cells is the
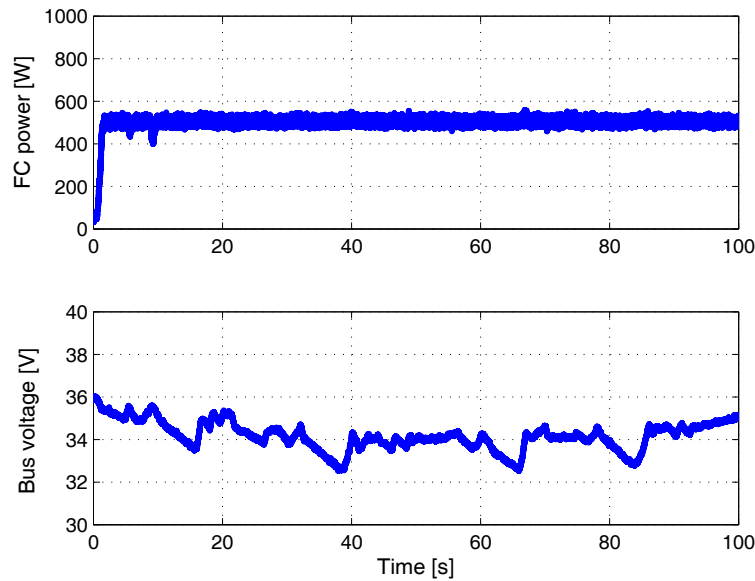
Figure 5.11: Fuel cell power flow and bus voltage for topology range extender during HiL-simulation of the load profile

placement of the switch in the converter, which is directly on the input branch where the fuel cells are connected. The switch will then cause a rippling behavior on the input current coming from the fuel cells and can deteriorate their lifetime.

5.2.3   Topology C: Full hybrid

The scheme of a full hybrid concept is depicted in Figure 5.12. In this topology, the fuel cells are directly connected to the bus. The DC/DC-converter output voltage affects from which source the power is coming. Setting a reference voltage value less than the fuel cell voltage would mean that most of the power comes from the fuel cells, whereas a higher voltage output would mean the power comes mostly from the SuperCaps.

In regenerative phases, the diode at the fuel cell output protects the fuel cells and the regenerated power goes to the SuperCaps through the bi-directional DC/DC-converter. As the bus has two conventional capacitors connected (one in the DC/DC-converter and one in the motor controller) the bus voltage is rapidly increasing with fast recuperation peaks. The increase of the bus voltage must be controlled with the bi-directional DC/DC-converter to the desired level. This is done by charging the SuperCaps with the surplus energy coming from regenerative braking. If the
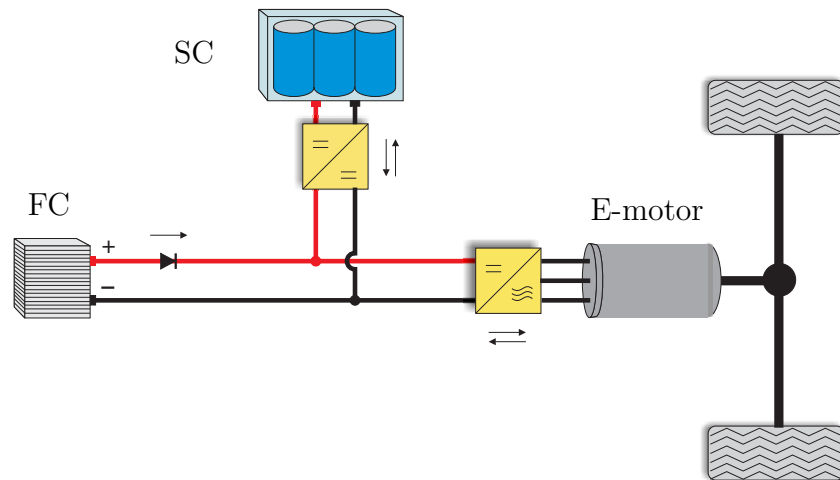
Figure 5.12: Topology C: full hybrid with a bi-directional DC/DC-converter for the SuperCaps
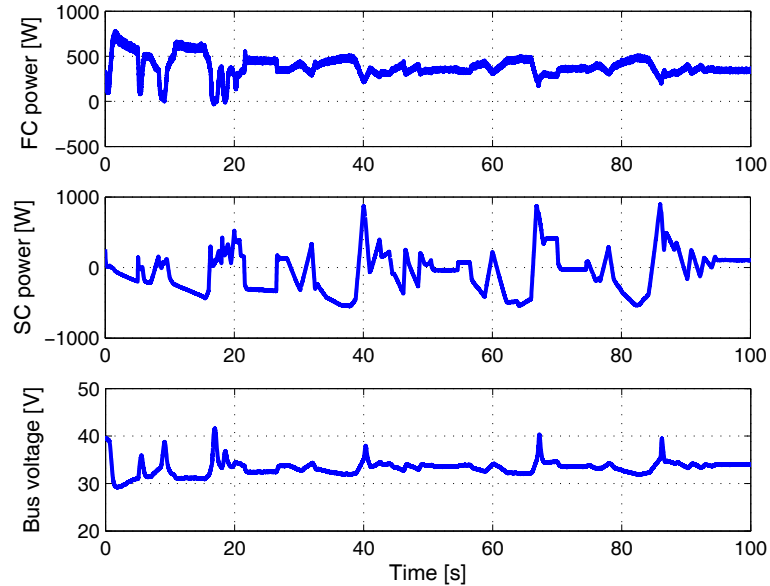

Figure 5.13: Power flows and bus voltage for topology full hybrid during the predefined load profile. The bus voltage and the fuel cell power is varying relatively much and affect the fuel cell lifetime negatively.

SuperCaps are fully charged, the energy must be dissipated in heat. The bus voltage varies more quickly due to the small capacitors as shown in Figure 5.13.

The bus voltage can rapidly be set to any value and guarantee high dynamics for the electro-motor. This gives a more variable bus voltage and hence a more varying power output from the fuel cells. Fuel cells however are not suitable for fast dynamics and additionally this leads to a faster deterioration of the fuel cells.

5.2.4   Topology D: Extended topology

The extended topology concept is depicted in Figure 5.14. According to [NPA06], this topology shows good performance but low range ability. This is logic due to the two DC/DC-converters used while for each converter there are losses. The good performance can be justified because of the continuously high supply voltage applied to the electro-motor. This guarantees the maximum dynamics that the electro-motor can achieve. Due to its complexity (especially in defining a suitable powermanagement strategy for this topology), its increased weight, and costs, this topology is not in detail examined here but would be an interesting topic of research for high performance hybrid systems.
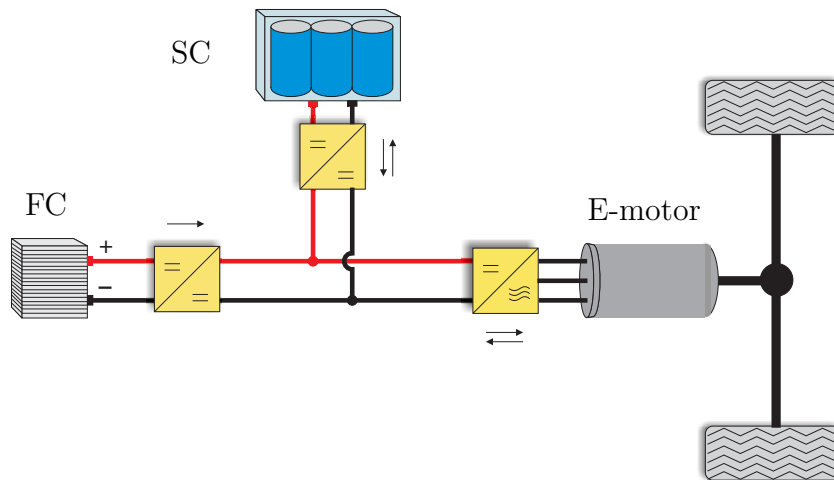

Figure 5.14: Topology D: Extended topology with DC/DC-converters for the fuel cell and accumulator

Summarizing this, Topology B (range extender) is used due to the ability of operating the fuel cells at a constant working point (which mitigates a fast fuel cell deterioration). Further on, this topology is easy to control and the efficiency losses are less than the other topologies.

5.3   Evaluation of the dynamics of the hybrid system

Here, the dynamical behavior of the individual components and the overall hybrid system behavior is evaluated. As explained in Chapter 2.1.3, in order to mitigate a fast fuel cell lifetime deterioration, it is important to avoid fast transients applied on the fuel cells. For this reason, the dynamics of the load profile, the fuel cells, and the SuperCaps is examined. In Figure 5.15 the difference of the dynamics between fuel cells and SuperCaps is depicted for a 2 kW step function of the power load. It is clearly shown how the faster dynamics and peak power are provided by the SuperCaps while the fuel cells supply a power output of 1 kW with a slower response.
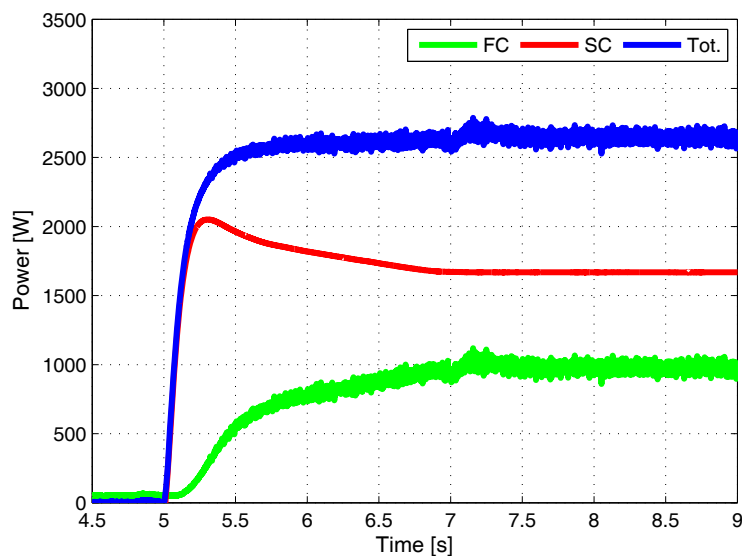

Figure 5.15: Step response on the hybrid system showing the dynamical behavior of the fuel cells and SuperCaps

Fuel cell systems are very complex and their dynamical behavior is determined by gas, thermal, humidity, and thermochemical effects. Time constants and bandwidth for these dynamics are presented in Figure 5.16 which are based on experimental examinations from [BPP+07, Win07, XTS+04, ZS07]. The lifetime strongly depends on the gradients of those dynamics.

Once the maximum peak power of the load profile is known, it makes sense to limit the components thereafter. The components that can deliver maximum power continuously should firstly be specified. Electro-motors however, have a maximum power output which is time-dependent. This is due to high currents heating up the
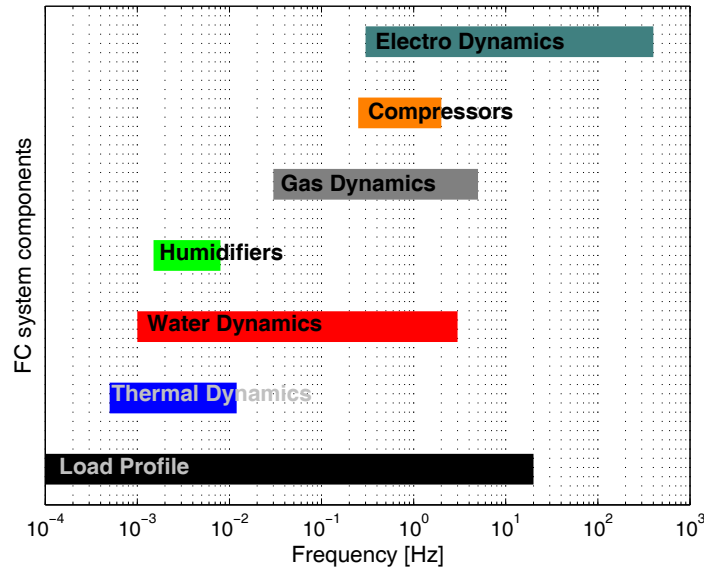
Figure 5.16: Dynamical behavior (corner frequencies) of the different components in a fuel cell system (Acc. to [BPP$^+$07, Win07, XTS$^+$04, ZS07])

wiring in the motor and without active cooling, there is a limit for how long the maximum power can be applied. By investigating the load profile with the power density function, several observations can be made to design the system components optimally. Typical electro-motors have a maximum continuous power output and a short-time peak power output. The continuous power output can be applied unlimitedly with time, while the peak power is limited for a certain time period. The ratio between maximum peak power and continuous power can vary for different motors. To avoid over-dimensioning of the electro-motor, the use of the ratio could save weight and costs on the motor due to optimal coil winding design. This generates a parameter recommendation to implement an electro-motor with continuous power output equal the fuel cell power and a maximum power equal the maximum load profile power.

Power density function

The power density function shows the frequency of occurrence of the power spectrum. By deriving the power density function from the load profile, it is possible to set the maximum efficiency points of the different components at the most occurred working point. The power density function of the motor torque and speed of the driving motor are seen in Figure 5.17 and 5.18.
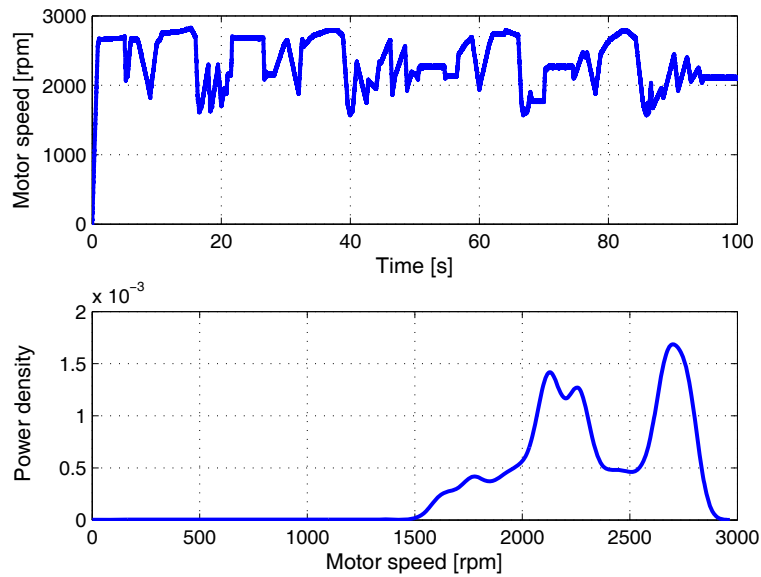
Figure 5.17: Power density function for the motor speed that can be used for motor sizing and powermanagement
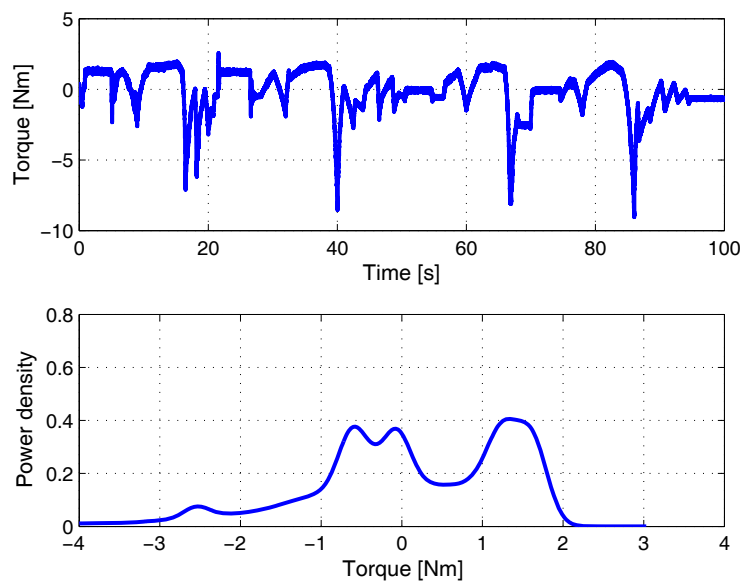

Figure 5.18: Power density function for the motor torque that equivalently can be used for motor sizing and powermanagement

Note that, it is not necessary for the hybrid system to accept regenerative braking to make sense. Costs could be reduced also with a fuel cell hybrid system without regenerative braking. This is due to that the fuel cells still can be down-sized due to that the batteries can provide peak power that exceeds the maximum fuel cell power. Of course, when regenerative braking is not present, the size of the batteries must be kept small in order to be fully charged by the fuel cells before the next power peak [LD00].

6 Powermanagement

In this chapter, different powermanagement strategies will be explained, implemented and the results will be presented. A powermanagement strategy is needed in almost all hybrid vehicle applications and depends strongly on the goals which are set by the developer. Powermanagement of hybrid vehicles can be explained as the control of the power flow between the hybrid components. In particular, this regards the control of the output voltage of the DC/DC-converter. Through the output voltage, it is possible to control the power flows arbitrarily.

6.1 Theory

Regenerative braking means that the braking energy of the system during deceleration is converted back to electrical energy which in turn is stored in the SuperCaps. In the case of brushless DC-motors, it is necessary to have a 4Q (four quadrant) motor controller in order to be able to save back regenerative braking energy. Theoretically, the maximum mechanical energy that can be saved back is calculated according to the kinetic energy of the vehicle with

$$E_{kin} = \frac{m_{veh} v_{veh}^2}{2}. \tag{6.1}$$

For the given vehicle with a mass of $m_{veh} = 201.3\,\mathrm{kg}$ and a maximum velocity of $m_{veh,max} = 50\,\mathrm{km/s}$ the maximum kinetic energy is 19 416 J. The energy stored in a single SuperCap (with constant capacitance) is calculated according

$$E_{sc} = \frac{CU^2}{2}. \tag{6.2}$$

For a SuperCap with a capacitance of 3000 F, the energy stored in a fully charged (2.7 V) SuperCaps is 10 935 J. The power to overcome the air drag is calculated according to

$$P_{drag} = \frac{\rho v_{veh}^3 A_{veh} C_d}{2}. \tag{6.3}$$

With the inserted values, the power to overcome the air drag at top velocity is 506 W. Since the DoH is set to that the fuel cells have a power output of 300 W the top speed can be achieved for a limited time. With the rated 300 W, it is possible to have a constant top speed of 42 km/h. If a capacitor is connected to the terminal input of the controller then the final voltage is calculated as

$$U_{final} = \sqrt{U_0^2 + \frac{2E_{init,kin}}{C}} \tag{6.4}$$

where U_{final} is the final voltage of the DC-bus, U_0 is the initial voltage, $E_{init,kin}$ is the initial kinetic energy, and C is the total capacitance of the connected capacitor.

In [Pro09], a fuel cell-based hybrid system is demonstrated and shows the charging of the accumulator. In this system, the developers choose to charge the accumulator from the fuel cells only in stand-still mode of the vehicle. Although it is technically achievable to charge the accumulator during acceleration and even during recuperation, it is not further explained why the accumulator is charged only during stand-still. However, this PM is not tried here because the SoC falls to a critical level for the driving cycles and the speed profile cannot be realized.

In this contribution three powermanagement strategies are tested and compared: rate limiter, charging only with maximum fuel cell power, and keeping a constant SoC of the SuperCaps, the results are also reported in [MOS09]. The powermanagement algorithms are tested for different SoC which strongly affects the evaluation results as will be seen. For evaluation, the fuel consumption, control error of the vehicle speed, and the deterioration of the fuel cells are chosen. An indicator for fuel cell deterioration is to high-pass filter the fuel cell power output and then calculate the standard deviation [MOS09]. As example of a driving cycle being simulated at the HiL test rig is depicted in Figures 6.1 and 6.2 which show clearly the difference in gradient output power of the fuel cells with and without a rate limiter. With decreased dynamics the load gradients of the fuel cells are lower, making the fuel cells work smoother and hence increase in power output slowly during discharging of the SuperCaps. Consequently, the fuel cells must charge the SuperCaps at the end of the cycle.

The driving cycles chosen to test the powermanagement on are the ECE and the EUCD cycles. These cycles correspond to a short cycle with starts and stops and to a cycle with smoother driving.

6.2 PM I: Rate limiter

Fuel cell lifetime aspects were discussed in Chapter 2. Especially, fast dynamics, alternating temperature, humidity, and current output affect the lifetime of fuel cells considerably. In order to achieve a longer lifetime, it is necessary to develop powermanagement strategies that smooth out the mentioned variables. In this section, such strategy will be described and tested. In [TRD06], the fuel cell stack current output was limited to $4\,\mathrm{As}^{-1}$ with a rate limiter in order to mitigate a fast fuel cell deterioration. The rate limiter inserted was for positive as well as negative slopes and hence decreased the fuel cell current output in a slower rate. This led to problems with overcharging of the SuperCap bank. Although fast transients of the fuel cell power output lead to a faster deterioration, there are no scientific contributions that suggest that a fast de-loading (negative transients) would lead to a faster fuel
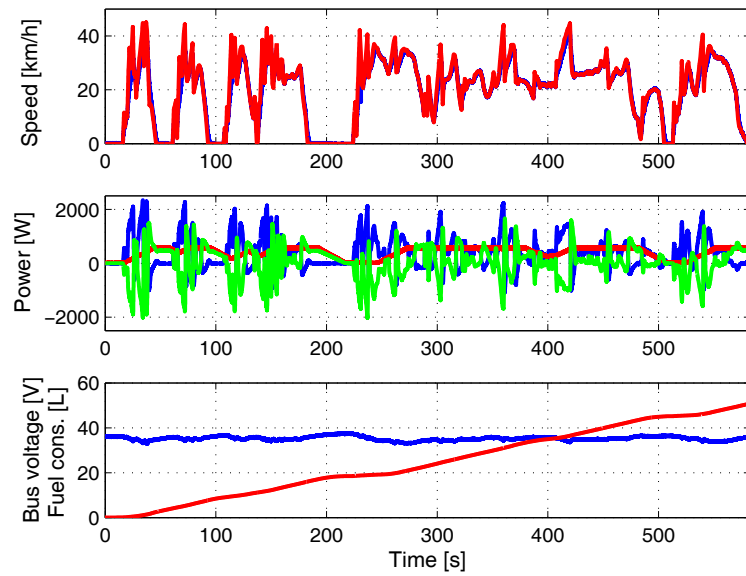
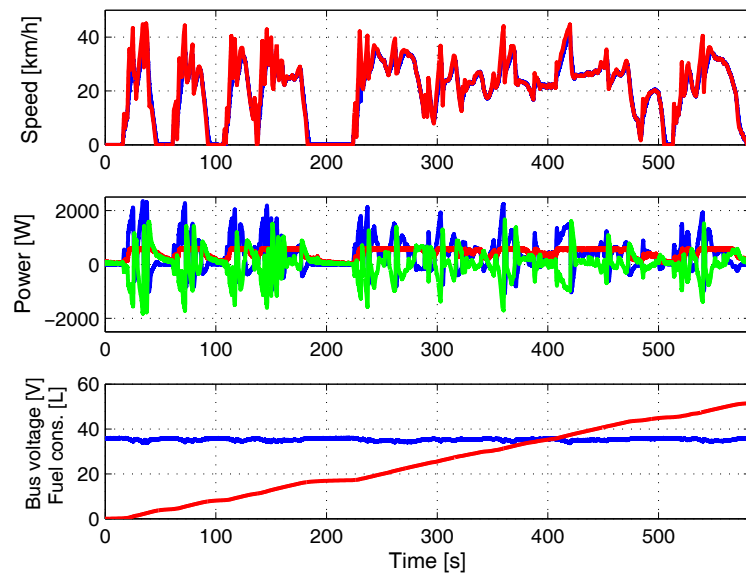Figure 6.1: ETC cycle with a rate-limiter of $1\,\mathrm{A/s}$

Figure 6.2: ETC cycle without rate limiter where more dynamical fuel cell power is observed

cell lifetime deterioration. The problem with overcharging of the SuperCap can be avoided with only regarding a current rate limiter for positive transients.

6.3 PM II: Maximum fuel cell power

The idea in PM II is to make the system react fast to low SoC which can decrease the performance and the dynamical capability of the system. During charging, the fuel cell will only run nearby optimal efficiency conditions, i.e. at 450 W. A disadvantage of this strategy is when the charging starts the fuel cell switches very fast between stand-by operation and full power. This can lead to a faster deterioration due to the high power gradients as described before in Chapter 2.1.3.

6.4 PM III: Constant SoC-level

The efficiency of the system components is discussed in Chapter 2 and shown for the fuel cells in Figure 2.7, for the DC/DC-converter in Figure 2.11, and for the combined fuel cell and DC/DC-converter in Figure 2.12. The conclusion is that the maximum efficiency with regard to fuel consumption is at 450 W. However, the efficiency deviates in different working points as well. This is investigated with PM III which keeps the SoC at a constant level by controlling the fuel cell system to charge the SuperCaps in order to keep the desired SoC.

6.5 Experimental results and evaluation

In order to correctly compare powermanagement strategies to each other for different driving cycles, it is necessary to compensate for the different SoC for the SuperCaps at the end of the cycle. This is done by measuring the fuel consumption per voltage as depicted in Figure 6.3 which corresponds to approximately 0.15 L/V (varying nonlinearly) for a constant charge current of 8 A.

Using curve fitting interpolation, as shown in Figure 6.3, the corrected fuel consumption between two voltage points is (after differentiating the interpolated function) approximated as

$$V_{H_2,corr} = \int_{V_1}^{V_2} (0.044V - 0.056)dV,\tag{6.5}$$

or equivalently

$$V_{H_2,corr} = (0.022V_2{}^2 - 0.056V_2) - (0.022V_1{}^2 - 0.056V_1).\tag{6.6}$$
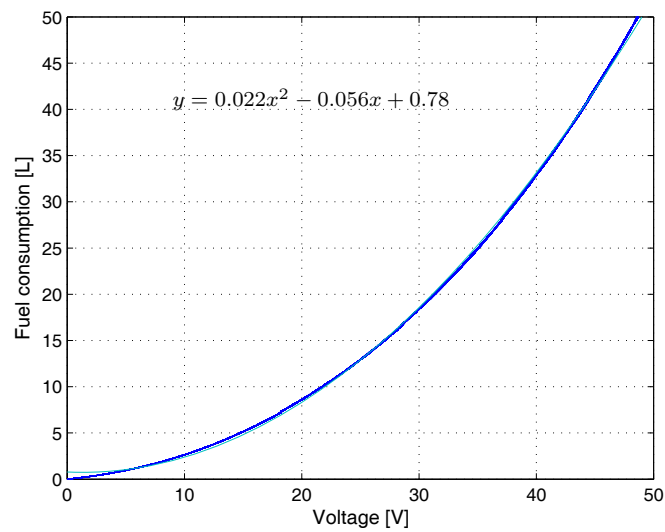
Figure 6.3: Fuel consumption as function of SuperCap voltage which varies around approximately $0.15\,\mathrm{L/V}$

After calculating the fuel required to refill the accumulator to its initial value, it is divided with the time length of the cycle and then multiplied with the measured fuel consumption function. This compensates for different SoC end value at the end of the driving cycle.
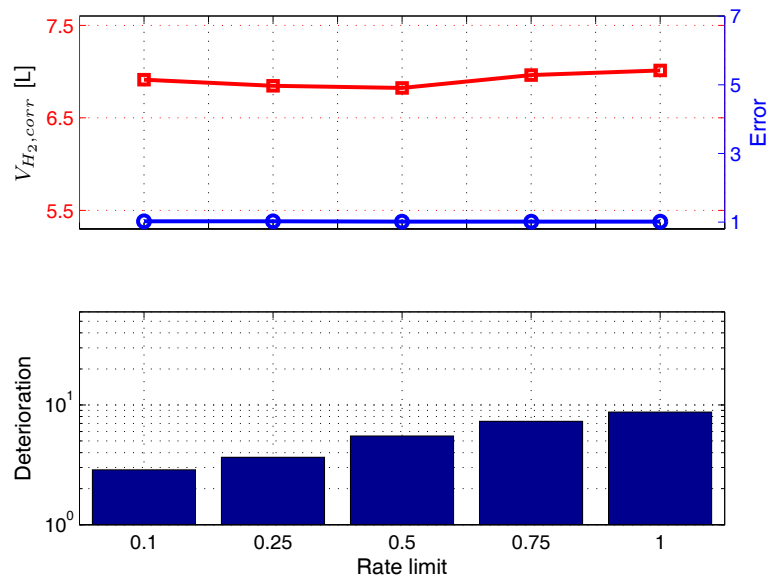
Figure 6.4: PM I - rate limiter on the ECE cycle. With higher rate limit the deterioration of the fuel cells increases, an optimum for fuel consumption is between a rate limit of 0.25 and 0.5.
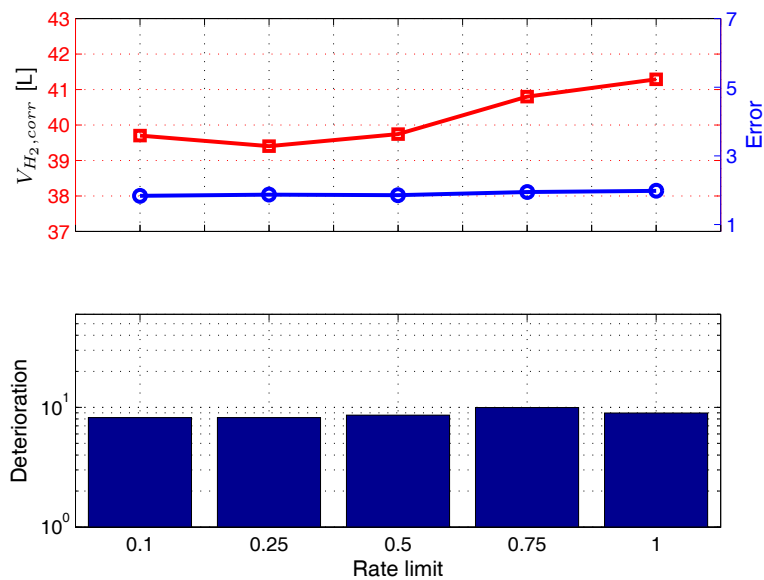
Figure 6.5: PM I - rate limiter on the EUDC cycle. With higher rate limit the deterioration of the fuel cells increases, an optimum for fuel consumption is between a rate limit of 0.25 and 0.5.
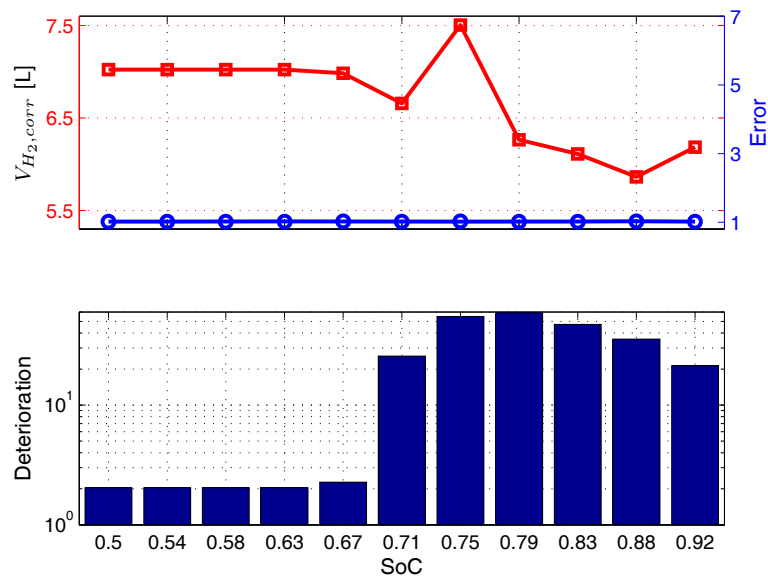
Figure 6.6: PM II - maximum FC power on the ECE cycle. Fuel consumption optimum at SoC=0.8 while for a low FC deterioration SoC below 0.7.
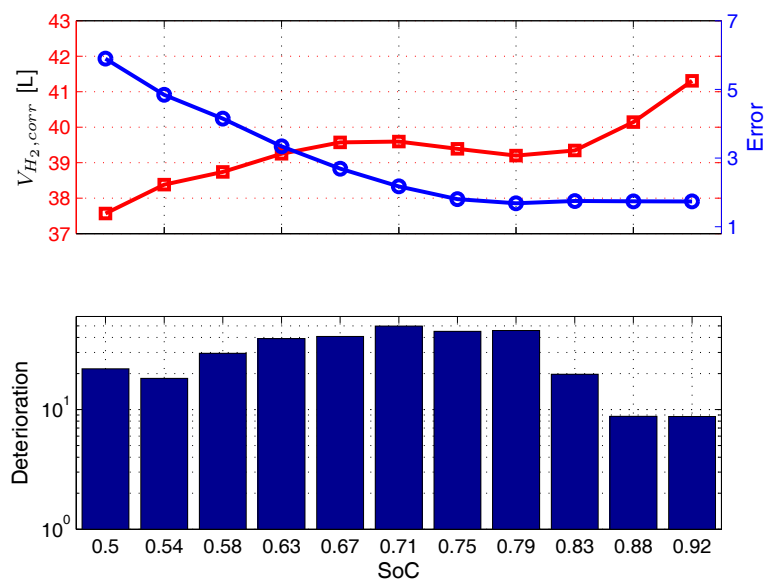
Figure 6.7: PM II - maximum FC power on the EUDC cycle. At SoC below 0.7 speed reference error is large, or fuel consumption optimum is at SoC=0.79.
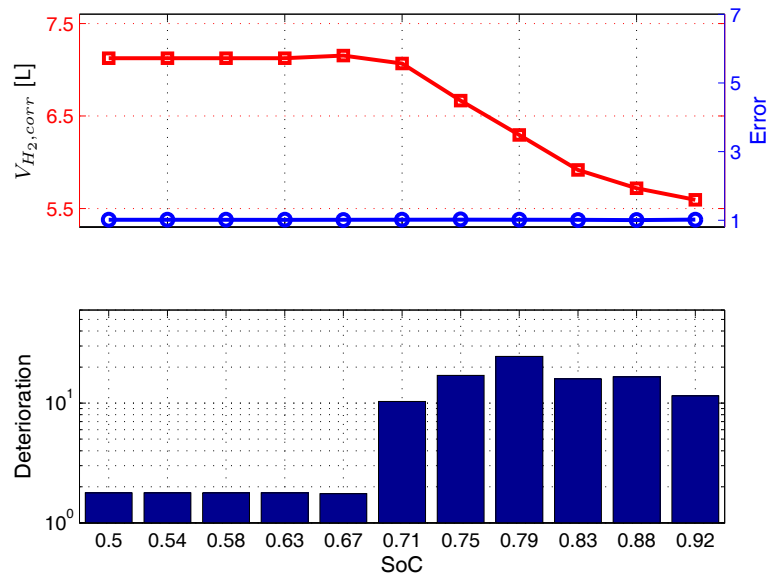
Figure 6.8: PM III - constant SoC on the ECE cycle. At SoC below 0.7 fuel cell deterioration is low as fuel consumption decreases with increased SoC.
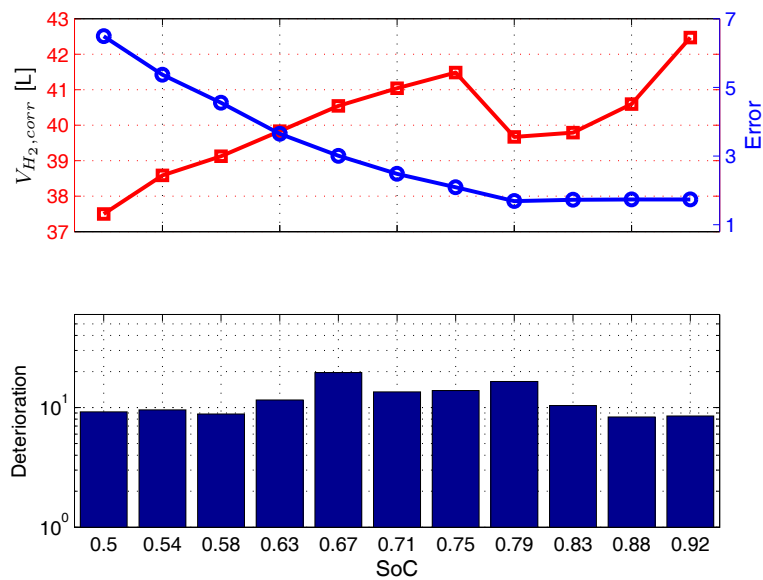
Figure 6.9: PM III - constant SoC on the EUDC cycle. At SoC below 0.79 speed reference error is large where also a local minimum of fuel consumption is observed.

Summarizing this, it can be seen that the deterioration on the fuel cells can effectively be decreased by the use of rate limitation as powermanagement. Due to the fast switching between full power and stand-by operation in PM II hereby the greatest deterioration can be observed. The small deterioration in the results in the ECE cycle are due to rare operation of the fuel cell system. Furthermore it can be observed that small SoC values have negative influence on the performance of the system. For the fuel consumption no general conclusion can be derived for all experiments but optimal SoC points could be observed due to system efficiency differences in different working points.

7 Summary and outlook

This work focuses on the development of a fuel cell-based hybrid electric powertrain for smaller (2 kW) hybrid electric vehicles (HEV's). A Hardware-in-the-Loop test rig was designed and built with the opportunity to simulate any load profile for HEV's in a realistic environment. Simulation models were developed and validated to real physical components and control algorithms were designed for the models. The design process of an HEV with regard to a given load profile was introduced with comparison between SuperCaps and batteries. The HEV was also evaluated with an introduction to powermanagement concepts that were implemented and compared.

7.1 Scientific contribution

The main scientific contribution of this work is to enable comprehensive development tools for future research in the field of electric hybrid vehicles. The detailed models that are developed and validated here give the opportunity to examine the sizing and scaling of accumulators, fuel cells, and electro-motor for HEV's. Additionally, different topologies can easily be simulated and evaluated from the simulation results. The models were developed with time-constants in consideration, in order to decrease the simulation time. As an example, the driving cycles that were simulated here had a simulation time less than half an hour for a normal PC.

Further on, the models can be used to implement new control algorithms and powermanagement strategies in a pre-development stage. The control algorithms developed were implemented in the models, due to instability of the system components. However, the control algorithms showed a performance and robustness that could well have the same positive results when implemented in real system components, i.e. fuel cell system, DC/DC-converters, and electro-motor. The gain-scheduling control method is a new control algorithm that is developed and implemented in a fuel cell system for the first time and it showed better results than state-feedback control and conventional static feed-forward control. The state-feedback control lacked in performance in the working points that are distanced from the linearization points. As a result, the stationary error increased. This is eliminated with the gain-scheduling control algorithm. The conventional static feed-forward control lacked in performance in avoiding oxygen starvation by controlling the excess oxygen ratio of the fuel cells in comparison to gain-scheduling control.

Hardware-in-the-Loop (HiL) simulations allow cost effective, safe, fast, but at the same time realistic simulations of a technical system. By modeling and simulating the environment, there is no need for field studies. The test rig that was designed and built here allows fast implementation of different components to be tested in a

realistic environment. The fuel cell system can easily be replaced with any system that generates electrical power, e.g. diesel, gasoline generator, or batteries. This gives the opportunity to examine different range extender power supply modules. Likewise, the SuperCap bank can also be replaced with different accumulators that allow recuperated energy. This was shown here with lead-batteries that proved to be insufficient for the given load profile due to their low power density tolerance.

7.2 Limitations

Although the models are detailed, there are some aspects not regarded here. These are aging of the components and temperature effects (with the exception of the fuel cell temperature model). The models are scalable up till a reasonable level, approx. 5-10 kW but the limitation of the scalability beyond the lower power classes is not proved here.

The HiL simulations have limitations in comparison to field studies in the sense that the environment is modeled. Although, the models are detailed, they contain always simplifications of the reality. These simplifications can however in this context be neglected. Realistic temperature studies (such as sub-zero temperature) or humid conditions are not regarded in these HiL simulations.

7.3 Future aspects

Due to the novelty of HEV's and the components included, the future aspects of this work are many. Fuel cells, SuperCaps, and high power DC/DC-converters are not available at the moment for large market. The research topics on improving these components have been intensified in recent years. From control perspective, there are still open issues on improving their performance. For fuel cells to have a higher power density, their lifetime deterioration in the higher power ranges must decrease. This gives a need especially to new membrane materials that are robust against large power peaks. Until then, rate limiters (as used here) are needed in order to maintain a long lifetime. The control of electro-motors is a well known science but with the introduction in vehicle applications there are new challenges on how to implement sophisticated braking recuperation algorithms that take vehicle safety such as anti-locking, anti-skidding, and vehicle stability control algorithms. Also in the DC/DC-converters there is a strong demand on minimizing the rippling behavior due to the switching in the converters. Rippling behavior can deteriorate the lifetime of the power source components applied on the converters. The control algorithms developed here are yet to be implemented in real systems.

At the moment, there are no mass-produced fuel cell electric vehicles (FCHEV's) for the market. Although, the prices could fall to considerable levels when FCHEV's are

mass-produced there exist no comprehensive infrastructure for hydrogen. The only country at the moment where it is fully possible to drive a hydrogen-driven vehicle is Norway, where a chain of hydrogen gas stations is built between the capitol of Oslo and the city of Stavanger [Ran09]. This partly makes the future aspects of fuel cell electric vehicles in the market to be a political question.

Bibliography

[AC08]   AHN, J.-W. ; CHOE, S.-Y.: Coolant controls of a PEM fuel cell system. In: *Journal of Power Sources* 179 (2008), April, Nr. 1, pp. 252–264

[Ada09a] ADAMSON, K.-A.: 2008 Large Stationary Survey / Fuel Cell Today. Version: 2009. `www.fuelcelltoday.com/media/pdf/surveys/2008-LS-Free.pdf`. – Techreport. – Online resource

[Ada09b] ADAMSON, K.-A.: Small Stationary Survey 2009 / Fuel Cell Today. Version: 2009. `www.fuelcelltoday.com/media/pdf/surveys/2009-Small-Stationary-Free-Report-2.pdf`. – Techreport. – Online resource

[Ame09]   American Department of Energy: *Basic Research Needs for Hydrogen Economy - Report of the Basic Energy Sciences Workshop on Hydrogen Production, Storage, and Use.* February Last visited date: November 27, 2009. `www.sc.doe.gov/bes/hydrogen.pdf`

[AN08]   ALBERTUS, P. ; NEWMAN, J.: I. A simplified model for determining capacity usage and battery size for hybrid and plug-in hybrid electric vehicles. In: *Journal of Power Sources* 183 (2008), August, Nr. 1, pp. 376–380

[ASS07]   AL-SWEITI, Y. ; SÖFFKER, D.: Modeling and Control of an Elastic Ship-Mounted Crane Using Variable Gain Model-Based Controller. In: *Journal of Vibration and Control* 13 (2007), Nr. 5, pp. 657–685

[Bal09]   *Ballard Power Systems Homepage*, Last visited date: November 27, 2009. `www.ballard.com`

[BDG$^+$06] BORUP, R. L. ; DAVEY, J. R. ; GARZON, F. H. ; WOOD, D. L. ; INBODY, M. A.: PEM fuel cell electrocatalyst durability measurements. In: *Journal of Power Sources* 163 (2006), December, Nr. 1, pp. 76–81

[BK06]   BAEHR, H. D. ; KABELAC, S.: *Thermodynamik.* Springer-Verlag Berlin, 2006

[BPP$^+$07] BERG, P. ; PROMISLOW, K. ; PIERRE, J. S. ; STUMPER, J. ; WETTON, B.: Water Management in PEM Fuel Cells. In: *Journal of Electrochemical Society* 151 (2007), January, Nr. 3, pp. A341–A353

[BPV98]   BAILEY, K. E. ; POWELL, B. K. ; VILLEC, G. N.: ABS/Traction Assist/Regenerative Braking Application of Hardware-in-the-Loop. In: *Proceedings of the American Control Conference.* Philadelphia, Pennsylvania, June 1998, pp. 503–507

[Bra09]   Brachmann, T.: Today's and future Hybrid- and Fuel Cell Vehicles of Honda. In: *6th Symposium on Hybrid Vehicles and Energy Management (HVEM)*. Braunschweig, Germany, February 2009, pp. 56–79

[CBF08]   Chandrasekaran, R. ; Bi, W. ; Fuller, T. F.: Robust design of battery/fuel cell hybrid systems – Methodology for surrogate models of Pt stability and mitigation through system controls. In: *Journal of Power Sources* 182 (2008), August, Nr. 2, pp. 546–557

[CGJ04]   Cropper, M. A. J. ; Geiger, S. ; Jollie, D. M.: Fuel cells: a survey of current developments. In: *Journal of Power Sources* 131 (2004), May, Nr. 1-2, pp. 57–61

[CHMF99]   Cunningham, J. M. ; Hoffman, M. A. ; Moore, R. M. ; Friedman, D. J.: Requirements for a flexible and realistic air supply model for incorporation into a fuel cell vehicle (FCV) system simulation / SAE. 1999 (1999-01-2912). – Techreport

[CWY⁺06]   Collier, A. ; Wang, H. ; Yuan, X. Z. ; Zhang, J. ; Wilkinson, D. P.: Degradation of polymer electrolyte membranes. In: *International Journal of Hydrogen Energy* 31 (2006), October, Nr. 13, pp. 1838–1854

[CZT⁺07]   Cheng, X. ; Zhang, J. ; Tang, Y. ; Song, C. ; Shen, J. ; Song, D. ; Zhang, J.: Hydrogen crossover in high-temperature PEM fuel cells. In: *Journal of Power Sources* 167 (2007), May, Nr. 1, pp. 25–31

[DWAH08]   Danzer, M. A. ; Wilheim, J. ; Aschemann, H. ; Hofer, E. P.: Model-based control of cathode pressure and oxygen excess ratio of a PEM fuel cell system. In: *Journal of Power Sources* 176 (2008), February, Nr. 2, pp. 515–522

[EIA09]   *Energy Information Administration*, Last visited date: December 02, 2009. http://tonto.eia.doe.gov/dnav/pet/pet_pri_wco_k_w.htm

[Eri99]   Erickson, R. W.: DC-DC Power Converters. In: *Wiley Encyclopedia of Electrical and Electronics Engineering* 5 (1999), pp. 53–63

[ERWL05]   Emadi, A. ; Rajashekara, K. ; Williamson, S. S. ; Lukic, S. M.: Topological overview of hybrid electric and fuel cell vehicular power system architectures and configurations. In: *IEEE Transactions on Vehicular Technology* 54 (2005), May, Nr. 3, pp. 763–770

[EXI09]   *EXIDE Technologies Homepage*, Last visited date: November 27, 2009. www.exide.at

[FM98]   FORSYTH, A. J. ; MOLLOV, S. V.: Modelling and control of DC-DC converters. In: *Power Engineering Journal* 12 (1998), October, Nr. 5, pp. 229–236

[GCLP04]   GRUJICIC, M. ; CHITTAJALLU, K. M. ; LAW, E. H. ; PUKRUSHPAN, J. T.: Model based control strategies in the dynamic interaction of air supply and fuel cell. In: *Proceedings of the Institution of Mechanical Engineers, Part A: Journal of Power and Energy* 218 (2004), Nr. 7, pp. 487–499

[Gro39]   GROVE, W. R.: A small voltaic battery of great energy. In: *Philosophical Magazine* 15 (1839), pp. 287–293

[Gro42]   GROVE, W. R.: On a Gaseous Voltaic Battery. In: *Philosophical Magazine and Journal of Science* XXI (1842), pp. 417–420

[Gue05]   GUENTHER, M. B.: *Modelling and Design Optimization of Low Speed Fuel Cell Hybrid Electric Vehicles*, University of Victoria, BC, Canada, Master thesis, 2005

[Hen08]   HENSON, W.: Optimal battery/ultracapacitor storage combination. In: *Journal of Power Sources* 179 (2008), April, Nr. 1, pp. 417 – 423

[HSHB00] HANSEN, A. D. ; SØRENSEN, P. ; HANSEN, L. H. ; BINDNER, H.: Models for a stand-alone PV system / Risø National Laboratory. 2000. – Techreport

[HSZ$^+$06] HUANG, X. ; SOLASI, R. ; ZOU, Y. ; FESHLER, M. ; REIFSNIDER, K. ; CONDIT, D. ; BURLATSKY, S. ; MADDEN, T.: Mechanical endurance of polymer electrolyte membrane and PEM fuel cell durability. In: *Journal of Polymer Science. Part B. Polymer physics* 44 (2006), July, Nr. 16, pp. 2346–2357

[HU07]   HELMOLT, R. von ; ULRICH, E.: Fuel cell vehicles: Status 2007. In: *Journal of Power Sources* 165 (2007), March, Nr. 2, pp. 833–843

[Hua08]   HUANG, X.: *Analytical Analysis of Fuel Cell Lifetime*, University of Duisburg-Essen, Chair of Dynamics and Control, Master thesis, February 2008

[Hyb09]   *Hybrid Vehicle Homepage*, Last visited date: December 02, 2009. `www.hybrid-vehicle.org/hybrid-vehicle-porsche.html`

[KFG$^+$09] KITOU, E. ; FERNANDEZ, R. ; GUGELE, B. ; GOETTLICHER, S. ; RITTER, M.: Annual European Community greenhouse gas inventory 1990-2007 and inventory report 2009 / European Environment Agency.

Version: May 2009. www.eea.europa.eu/publications/. – Techreport. – Online resource

[Kie07]   KIEL, E.: *Antriebslösungen - Mechatronik für Produktion und Logistik.* Heidelberg : Springer-Verlag, 2007

[KMD02]   KAPUR, A. ; MALHOTRA, R. ; DUTTA, U.: Roots Blowers: Understanding Twin Lobe Operation. In: *Chemical Engineering World* 37 (2002), September, Nr. 7, pp. 78–80

[KML⁺05]   KOKKOLARAS, M. ; MOURELATOS, Z. ; LOUCA, L. ; FILIPI, Z. ; DE-LAGRAMMATIKAS, G. ; STEFANOPOLOU, A. ; PAPALAMBROS, P. ; AS-SANIS, D.: Design under Uncertainty and Assessment of Performance Reliability of a Dual-Use Medium Truck with Hydraulic-Hybrid Powertrain and Fuel Cell Auxiliary Power Unit. In: *SAE 2005 Transactions: Journal of Passenger Cars - Mechanical Systems*, 2005

[KP07]   KIM, M.-J. ; PENG, H.: Power management and design optimization of fuel cell/battery hybrid vehicles. In: *Journal of Power Sources* 165 (2007), March, Nr. 2, pp. 819–832. – IBA - HBC 2006 - Selected papers from the INTERNATIONAL BATTERY ASSOCIATION & HAWAII BATTERY CONFERENCE 2006 Waikoloa, Hawaii, USA 9-12 January 2006

[KSLK08]   KIM, M. ; SOHN, Y.-J. ; LEE, W.-Y. ; KIM, C.-S.: Fuzzy control based engine sizing optimization for a fuel cell/battery hybrid mini-bus. In: *Journal of Power Sources* 178 (2008), April, Nr. 2, pp. 706–710

[LD00]   LARMINIE, J. ; DICKS, A.: *Fuel Cell Systems Explained.* Baffins Lane, Chichester, West Sussex, U.K. : John Wiley & Sons, Ltd., 2000

[LG91]   LJUNG, L. ; GLAD, T.: *Modellbygge och simulering.* Lund, Sweden : Studentlitteratur, 1991

[LL00]   LEITH, D. J. ; LEITHHEAD, W. E.: Survey of gain-scheduling analysis and design. In: *International Journal of Control* 73 (2000), Nr. 11, pp. 1001–1025

[MFF⁺08]   MAASS, S. ; FINSTERWALDER, F. ; FRANK, G. ; HARTMANN, R. ; MERTEN, C.: Carbon support oxidation in PEM fuel cell cathodes. In: *Journal of Power Sources* 176 (2008), February, Nr. 2, pp. 444–451

[MJJ⁺06]   MIESSE, C. M. ; JUNG, W. S. ; JEONG, K.-J. ; LEE, J. K. ; LEE, J. ; HAN, J. ; YOON, S. P. ; NAM, S. W. ; LIM, T.-H. ; HONG, S.-A.: Direct formic acid fuel cell portable power system for the operation of a laptop computer. In: *Journal of Power Sources* 162 (2006), November, Nr. 1, pp. 532–540

[MK99]   Moraal, P. ; Kolmanovsky, I.: Turbocharger Modeling for Auto-
           motive Control. In: *International Congress & Exposition*, 1999

[MOS09]   Marx, M. ; Özbek, M. ; Söffker, D.: Comparison and Evaluation
           of Power Management Approaches Applied to a Fuel Cell-based Hybrid
           HiL Powertrain. In: *7th Workshop on Advanced Control and Diagnosis
           (ACD 2009)*. Zielona Góra, Poland, November 2009

[MS07]   Moran, M. J. ; Shapiro, H. N.: *Fundamentals of engineering ther-
           modynamics*. 5. Chichester, U.K. : Wiley, 2007

[NGD07]   Na, W. K. ; Gou, B. ; Diong, B.: Nonlinear Control of PEM Fuel
           Cells by Exact Linearization. In: *IEEE Transactions On Industry Ap-
           plications* 43 (2007), Nr. 6, pp. 1426–1433

[NPA06]   Naylor, S. M. ; Pickert, V. ; Atkinson, D. J.: Fuel Cell Drive Train
           Systems - Driving Cycle Evaluation of Potential Topologies. In: *IEEE
           Vehicle Power and Propulsion Conference (VPPC '06)*, 2006, pp. 1–6

[OS08]   Özbek, M. ; Söffker, D.: Modeling and Simulation of a Fuel Cell-
           based Hybrid Powertrain. In: *Proc. IEEE/ASME International Con-
           ference on Mechtronic and Embedded Systems and Applications (MESA
           2008)*. Beijing, China, October 2008, pp. 298–303

[Pro09]   *Proton Motors GmbH Homepage*, Last visited date: December 02, 2009.
           `www.proton-motor.de/pm-hybridsystems.html`

[PSP04]   Pukrushpan, J. T. ; Stefanopolou, A. G. ; Peng, H.: *Control
           of fuel cell power systems: principles, modeling, analysis, and feedback
           design*. Springer-Verlag, London Limited, 2004

[Ran09]   Randers, J.: The Low Emission Norway Project. In: *The 24th Inter-
           national Battery, Hybrid and Fuel Cell Electric Vehicle Symposium &
           Exhibition*. Stavanger, Norway, May 2009

[SDA09]   Segura, F. ; Durán, E. ; Andújar, J. M.: Design, building and
           testing of a stand alone fuel cell hybrid system. In: *Journal of Power
           Sources* 193 (2009), pp. 276–284

[Smi09]   *Smithsonian Institution Homepage*, Last visited date: December 02,
           2009. `http://scienceservice.si.edu/pages/059013.htm`

[SSR08]   Steiger, W. ; Scholz, I. ; Riemann, A.: Electrification of Powertrain
           Systems - Battery, Fuel Cell or Both? In: *ATZautotechnology* 8 (2008),
           May, Nr. 5, pp. 18–22

[SYG07] Shao, Y. ; Yin, G. ; Gao, Y.: Understanding and approaches for the durability issues of Pt-based catalysts for PEM fuel cell. In: *Journal of Power Sources* 171 (2007), September, Nr. 2, pp. 558–566

[SZG91] Springer, T. E. ; Zawodzinski, T. A. ; Gottesfeld, S.: Polymer Electrolyte Fuel Cell Model. In: *Journal of the Electrochemical Society* 138 (1991), August, Nr. 8, pp. 2334–2342

[TPJ+07] Tang, H. ; Peikang, S. ; Jiang, S. P. ; Wang, F. ; Pan, M.: A degradation study of Nafion proton exchange membrane of PEM fuel cells. In: *Journal of Power Sources* 170 (2007), June, Nr. 1, pp. 85–92

[TRD06] Thounthong, P. ; Raël, S. ; Davat, B.: Control strategy of fuel cell/supercapacitors hybrid power sources for electric vehicle. In: *Journal of Power Sources* 158 (2006), July, Nr. 1, pp. 806–814

[TZ00] Thomas, S. ; Zalbowitz, M.: Fuel Cells - Green Power / Los Alamos National Laboratory. 2000. – Techreport

[Uni92] United Nations: *UNITED NATIONS FRAMEWORK CONVENTION ON CLIMATE CHANGE.* Last visited date: November 27, 1992. `http://unfccc.int/resource/docs/convkp/conveng.pdf`

[Uni98] United Nations: *KYOTO PROTOCOL TO THE UNITED NATIONS FRAMEWORK CONVENTION ON CLIMATE CHANGE.* 1998. `http://unfccc.int/resource/docs/convkp/kpeng.pdf`

[Ven86] Venkataramanan, R.: *Sliding Mode Control of Power Converters*, California Insitute of Technology, Dissertation, 1986

[WCF+06] Wahdame, B. ; Candusso, D. ; Francois, X. ; Harel, F. ; Pera, M.-C. ; Hissel, D. ; Kauffmann, J.-M.: Dual Response Surface Approach for the Analysis of a Fuel Cell Durability Test. In: *IEEE 32nd Annual Conference on Industrial Electronics - IECON 2006*. Paris, France, November 2006, pp. 4337–4342

[Win07] Wingelaar, P. J. H.: *Low-temperature fuel cells operating with contaminated feedstock*. Eindhoven, Holland, TUE Technische Universiteit Eindhoven, Dissertation, 2007

[XTS+04] Xue, X. ; Tang, J. ; Smirnova, A. ; England, R. ; Sammes, N.: System level lumped-parameter dynamic modeling of PEM fuel cell. In: *Journal of Power Sources* 133 (2004), June, Nr. 2, pp. 188–204

[YSMH09] YOUSFI-STEINER, N. ; MOÇOTÉGUY, Ph. ; HISSEL, D.: A review on polymer electrolyte membrane fuel cell catalyst degradation and starvation issues - Causes, consequences, and diagnostic for mitigation. In: *Journal of Power Sources* 194 (2009), October, Nr. 1, pp. 130–145

[YY07] YU, X. ; YE, S.: Recent advances in activity and durability enhancement of Pt/C catalytic cathode in PEMFC - Part II. In: *Journal of Power Sources* 172 (2007), October, Nr. 1, pp. 145–154

[ZB98] ZUBIETA, L. ; BONERT, R.: Characterization of Double-Layer Capacitors (DLCs) for power electronics applications. In: *1998 IEEE Industry Applications Conference. Thirty-Third IAS Annual Meeting.* Bd. 2, 1998, pp. 1149–1154

[ZBT09] *Zentrum für BrennstoffzellenTechnik ZBT GmbH Homepage*, Last visited date: November 27, 2009. `www.zbt-duisburg.de`

[ZGZW08] ZHANA, Y. ; GUOB, Y. ; ZHUB, J. ; WANG, H.: Intelligent uninterruptible power supply system with back-up fuel cell/battery hybrid power source. In: *Journal of Power Sources* 179 (2008), May, Nr. 2, pp. 745–753

[ZLYO08] ZHANG, J. ; LIU, G. ; YU, W. ; OUYANGA, M.: Adaptive control of the airflow of a PEM fuel cell system. In: *Journal of Power Sources* 179 (2008), May, Nr. 2, pp. 649–659

[ZS07] ZENITH, F. ; SKOGESTAD, S.: Control of fuel cell power output. In: *Journal of Process Control* 17 (2007), April, Nr. 4, pp. 333–347